UNIVERSITY OF SOUTHAMPTON

FACULTY OF ENGINEERING AND THE ENVIRONMENT

School of Engineering Sciences

Numerical Investigations of Thermal Spray Coating Processes:

Combustion, Supersonic Flow, Droplet Injection and Substrate Impingement Phenomena

by

Hani Tabbara

Supervision: Dr. Sai Gu and Prof. Kai H. Luo

Thesis for the degree of Doctor of Philosophy

June 2012

Abstract

The aim of this thesis is to apply CFD methods to investigate the system characteristics of high speed thermal spray coating processes in order facilitate technological development. Supersonic flow phenomena, combustion, discrete droplet and particle migration with heating, phase change and disintegration, and particle impingement phenomena at the substrate are studied. Each published set of results provide an individual understanding of the underlying physics which control different aspects of thermal spray systems.

A wide range of parametric studies have been carried out for HVOF, warm spray, and cold spay systems in order to build a better understanding of process design requirements. These parameters include: nozzle cross-section shape, particle size, processing gas type, nozzle throat diameter, and combustion chamber size. Detailed descriptions of the gas phase characteristics through liquid fuelled HVOF, warm spray, and cold spray systems are built and the interrelations between the gas and powder particle phases are discussed. A further study looks in detail at the disintegration of discrete phase water droplets, providing a new insight to the mechanisms which control droplet disintegration, and serves as a fundamental reference for future developments of liquid feedstock devices.

In parallel with these gas-particle-droplet simulations, the impingement of molten and semi-molten powder droplets at the substrate is investigated and the models applied simulate the impingement, spreading and solidification. The results obtained shed light on the break-up phenomena on impact and describe in detail how the solidification process varies with an increasing impact velocity. The results obtained also visually describe the freezing induced break-up phenomenon at the splat periphery.

Contents

Acknowledgements

First and foremost, I would like to thank Prof. Sai Gu and Prof. Kai Luo for giving me the opportunity to explore this fascinating topic. Their enthusiasm and drive has given me the strength to persevere with this PhD project, and I will be forever grateful. I would also like to thank the supervisory support of Prof. Graham McCartney from the University of Nottingham and Dr Terry Lester from Metallisation Ltd for kindly donating their time and efforts.

I could write a separate thesis acknowledging the help and efforts of Jamilla Shahin. During the good times and the less good times, she was always there. I thank my mother and father and two brothers too for always remaining close. To my friends and colleagues within building 25 and beyond, thank you for sharing your thoughts, ideas, knowledge and friendship. Andreas, Arvind, Costas, Derick Shen, Georgios and Agathi, Jorn, Jun Xia, Kostas, Leon, Lindsay, Nanhang, Nathan Waters, Raymond Wong, Samuel, Siddharth, Shayan, and Spyros, thank you.

I dedicate this small piece of work to my Grandma Eileen, who has supported me wholeheartedly throughout my life.

Declaration of authorship

I, **Hani Tabbara**

Declare that the thesis entitled "**Numerical Investigation of Thermal Spray Coating Processes: Combustion, Supersonic Flow, Droplet Injection and Substrate Impingement Phenomena"** and the work presented in the thesis are both my own, and have been generated by me as the result of my own original research. I confirm that:

- this work was done wholly or mainly while in candidature for a research degree at this University;
- where any part of this thesis has previously been submitted for a degree or any other qualification at this University or any other institution, this has been clearly stated;
- where I have consulted the published work of others, this is always clearly attributed;
- where I have quoted from the work of others, the source is always given. With the exception of such quotations, this thesis is entirely my own work;
- I have acknowledged all main sources of help;
- where the thesis is based on work done by myself jointly with others, I have made clear exactly what was done by others and what I have contributed myself;
- the published articles on the following page make up the majority content of this thesis;

Signed: ……

Date:……

List of publications

Journal articles

Tabbara, H. Gu, S (2012) A Study of Liquid Droplet Disintegration for the Development of Nanostructured Coatings. *AIChE Journal*, doi: 10.1002/aic.13755.

Tabbara, H. Gu, S. (2012) Modelling of impingement phenomena for molten metallic droplets with low to high velocities. *Int. J. Heat Mass Tran.*, 55(7-8), 2081–2086.

Tabbara, H. Gu. S. (2011) Numerical study of semi-molten droplet impingement. *Appl. Phys. A*, 104 (4), 1011–1019.

Tabbara, H. Gu, S. McCartney, D. G. (2011) Computational modelling of titanium particles in warm spray. *Comput. Fluids.*, 44 (1), 358–368

N. Zeoli, H. Tabbara, S. Gu (2011) CFD modeling of primary breakup during metal powder atomization. *Chem. Eng. Sci.*, 66 (24), 6498–6504.

Tabbara, H. Gu, S. McCartney, D. G. Price, T. S. and Shipway, P. H. (2010) Study on Process Optimization of Cold Gas Spraying, *J. Therm. Spray Technol.*, 20 (3), 608–620.

Tabbara, H. Gu, S. (2009) Computational simulation of liquid-fuelled HVOF thermal spraying. *Surf. Coat. Technol.,* 204 (5), 676–684.

Conference papers

Tabbara, H. Kamnis, S. Gu, S. (2011) Modelling ceramic droplet impingement. IN: *Proceedings of the international thermal spray conference*, September 27-29, Hamburg, Germany.

Tabbara, H. Gu, S. (2011) Simulation of HVOF thermal spray for nano-coatings. IN: *Proceedings of the twelfth UK national heat transfer conference*, August 30 - September 1, Leeds, UK.

A. Kumar, H. Tabbara, S. Kamnis, S. Gu (2011) Numerical modelling of hollow metal droplet impingements. IN: *Proceedings of the twelfth UK national heat transfer conference*, August 30 - September 1, Leeds, UK.

Tabbara, H. Gu, S. (2010) Computational modelling of thermal spray systems. IN: *Proceedings of the sixteenth school of engineering sciences (SES) postgraduate conference*, October 1, Shirrel Heath, Hampshire, UK.

Tabbara, H. Gu, S. McCartney, G. (2010) Computational Investigation of Warm Spray. IN: *Proceedings of the international thermal spray conference*, May 3-5, Singapore.

List of figures

List of tables

Abbreviations

CD	*Convergent Divergent*
CFD	*Computational Fluid Dynamics*
CGDS	*Cold Gas Dynamic Spray*
FOV	*Field of View*
HA	*Hydroxyapatite*
HVOF	*High Velocity Oxygen Fuel*
HVOLF	*High Velocity Oxygen Liquid Fuel*
LD	*Laser Diffractometry*
MOC	*Method of Characteristics*
PDIA	*Particle Droplet Image Analysis*
RMS	*Root Mean Square*
RSM	*Reynolds Stress Model*
SEM	*Scanning Electron Microscope*
SOFC	*Solid Oxide Fuel Cell*
SPS	*Suspension Plasma Spray*
SPTS	*Solution Precursor Thermal Spraying*
UDF	*User Defined Function*
WS	*Warm Spray*
VOF	*Volume of Fluid*

1 Introduction

1.1 Thermal spray coatings

A thermal spray coating is a chaotic process formed by accelerating a stream of molten, semi molten or solid particles towards a targeted substrate surface using an energized process gas. The particles initially impact onto the substrate where in general, they are required to plastically deform and adhere to the surface through mechanical interlocking with the asperities and diffusion-type bonds. The particles then impinge onto one another, building up the coating particle by particle in a successively layered lamellae structure. The degree of deformation of the particles and their adhesion strength can be attributed to several factors, including: particle velocity, particle size; phase content; particle material properties; wetting of the substrate; temperature of the substrate and substrate roughness. Features such as voids, oxidized material and unmelted particles may be present in the coating, as depicted by the buildup process in Figure 1.1.

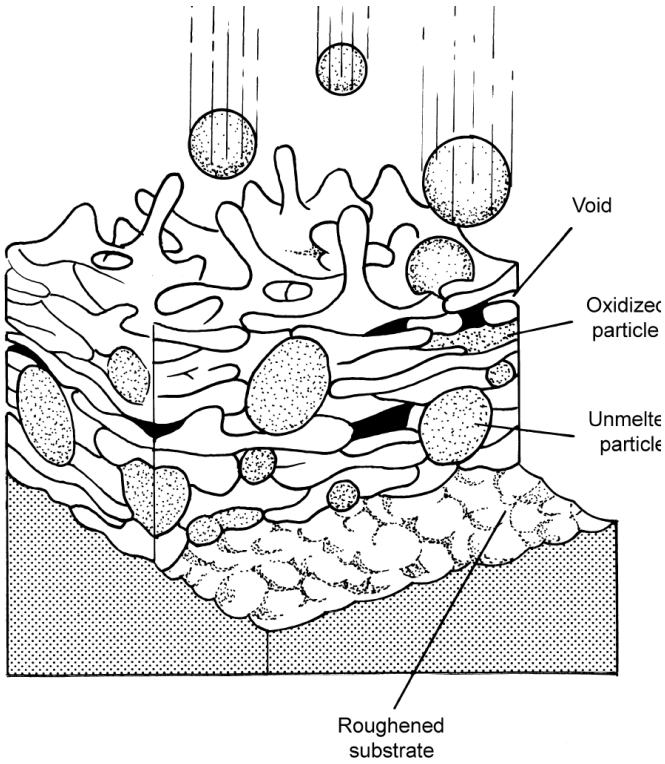

Figure 1.1: Diagram showing the build-up of a thermal spay coating. The image is courtesy of Davies (2004).

The combination of different coating features determines the coating properties. These features include the lamellar or layered splat structure, entrapped unmelted or solidified particles, pores, oxide inclusions, grains, phases, cracks, and bond interfaces. Figure 1.2 is a scanning electron microscope (SEM) image showing the micro-morphology of a composite coating cross-section after impact, consisting of chromium-carbide with a nickel based binder phase alloy. Figure 1.2 is a good example of how particles may undergo varying degrees of deformation, and the impact structures are indicative of the degree of particle heating and melting achieved during their in-flight migrations. However, for a cold sprayed powder the extent of particle deformation within the coating is governed by particle kinetic energy. In turn, the levels of thermal softening and impact velocity contribute to the cohesion, porosity, and subsequent properties of the manufactured coatings.

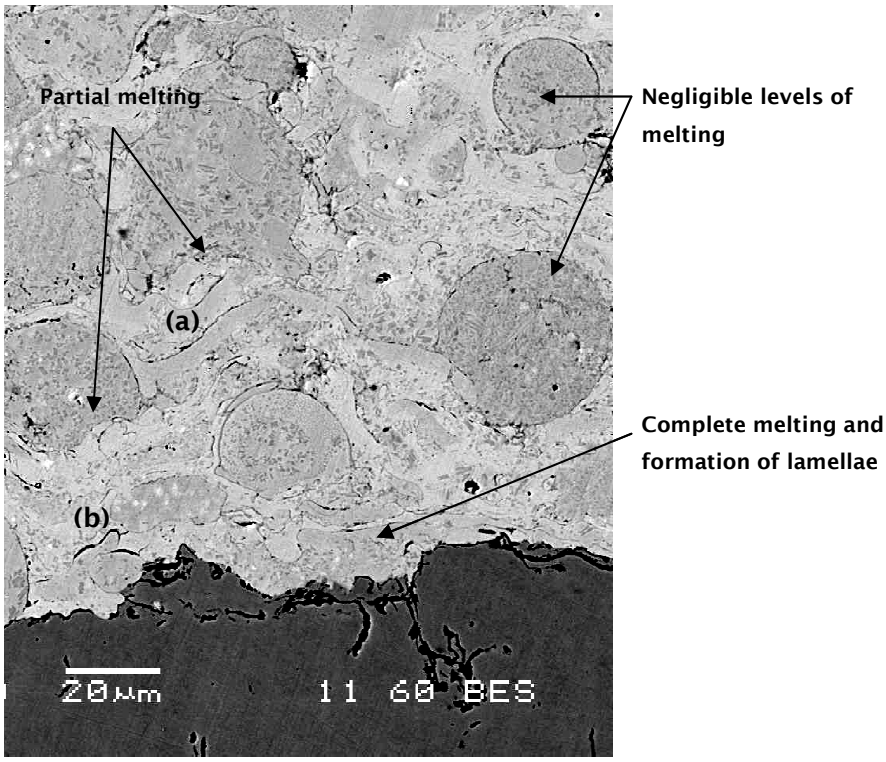

Figure 1.2: Scanning electron microscope image of a composite coating microstructure, highlighting different degrees of melting and deformation.

Oxide inclusions (also known as stringers) usually appear as dark strings-like borders surrounding deformed droplets in the coating cross section. Two examples are highlighted in Figure 1.2, underneath labels (a) and (b). Oxides are produced by chemical reaction at the particle surface and can occur during in-flight propulsion and during heating at coating surface during deposition. These oxide films are thickened

by longer dwell times and higher particle and gas temperatures. The oxide inclusions increase the coating hardness leading to brittle coatings which fracture easily. Furthermore, high oxide concentrations interfere with splat-to-splat cohesion, leading to decreased cohesive strength. However, for some applications oxide inclusions are desired because of increased wear resistance and lower thermal conductivity.

Coating porosity is another major feature which strongly influences the coating properties generated. As with the oxide inclusions, the porosity may be a desirable trait. For instance, medical implant prostheses require porous coatings to allow bone growth into the coating, which aids patient healing. Another use for porous coatings is in the dye sensitized solar cell. However, generally, porosity reduces coating cohesion and increases wear and corrosion rates. The pores are usually created by unmelted or resolidified particles and the resulting poor splat or particle cohesion often results in premature cracking, delamination, or spalling. Furthermore, pores which interconnect from the coating interface enable corrosion or oxidization at the substrate.

There are several ways of generating coating porosity. These include: material shrinkage during solidification; solid particles creating voids; poor intersplat cohesion; intersplat and intrasplat cracking; shadowing from adjacent surfaces and porosity within the feedstock. However, the most common source is trapped, unmelted, or resolidified particles. As thermal spray is a line-of-sight process the next arriving particles cannot fill voids adjacent to trapped solid particles. In some cases a partially melted particle can provide sufficient liquid to fill voids that form around a solid core. Porosity control is largely determined by: particle size distribution; the method of powder manufacture; the degree of melting of the sprayed particles; and their angle of impact. Furthermore: particle melting can be controlled by: jet temperature and enthalpy distribution; jet gas heat transfer properties; particle size and size distribution; particle morphology; particle heat transfer properties; particle dwell time; and the particle trajectory and spray distribution. Details of these coating microstructures can be found in literature (Davies 2004, Pawlowski 2008b).

The arriving particle or molten droplet velocity distributions also determine the extent of porosity formation. The impact kinetic energy is used to deform each particle or droplet. For a liquid droplet, this energy spreads the droplet surface to fill voids and cover surface irregularities, strengthening interparticle cohesion. For a solid or part-melted particle, the material is plastically deformed. As a result, higher particle velocities relate to greater particle deformations. These elevated impact energies also help to break up oxide inclusions, leading to lower oxide-related porosity. In general,

higher particle impact velocities are favoured over heating and melting to improve coating density by forcing closed the pores.

The thermal spray process is initiated by feeding the coating material into the system in the form of powder, wire, rod, or dissolved or suspended in a liquid. Various methods are then used to accelerate and heat the material particles to a critical adhesion state. The thermal and kinetic energy of the gas which is responsible for heating and accelerating the feedstock can be energized by a combination of plasma arc (see Fauchais & Vardelle 2011); high pressure inert gases (see Kumar et al. 2009, Yoon et al. 2009); and a combustion reaction (see M. Li & Christophides 2009). As a result, a wide spectrum of particle impact velocities and temperatures can be achieved; ranging from several tens to several thousands of metres per second and from below room temperature up to several thousand degrees Kelvin. Using these methods, almost every type of material that does not degrade when heated can be deposited to form a coating. The different thermal spray techniques are categorized in Table 1.1 into groups of primary energy source.

Energy source	Spray techniques
Electric discharge	• Arc spraying • Atmospheric plasma spraying • Vacuum plasma spraying
Combustion	• High velocity oxygen-fuel (HVOF) • Flame spray • Detonation gun • Warm spray
Compression of gas	• Cold gas spray

Table 1.1: Classification of the main thermal spray processes grouped by the type of energy source

The expected range of particle temperatures and velocities for several different thermal spray systems are summarized by Figure. 1.3. For the spray methods with high kinetic energy the in-flight particle time is short and consequently, these particles generally impact at the substrate without complete melting. This family of thermal spraying includes detonation spray, high-velocity oxygen fuel (HVOF), cold-gas spraying, and warm spray.

One of the earliest forms of supersonic spray coating technique was developed in the 1950s by Union Carbide, and named the detonation gun, also known as the D-Gun.

For this pulsed detonation spray method, high particle velocities are achieved, which generally exceed 800 ms^{-1} (Kadyrov, 1996). Large levels of particle impact deformation occur at the substrate for particles being accelerated by this method, forming low porosity coatings with high levels of adhesion and cohesion and coating hardness (Sundararajan et al., 2005). For these reasons, wear resistant coatings such as those applied to commercial jet aircraft engines are created often using WC-Co.

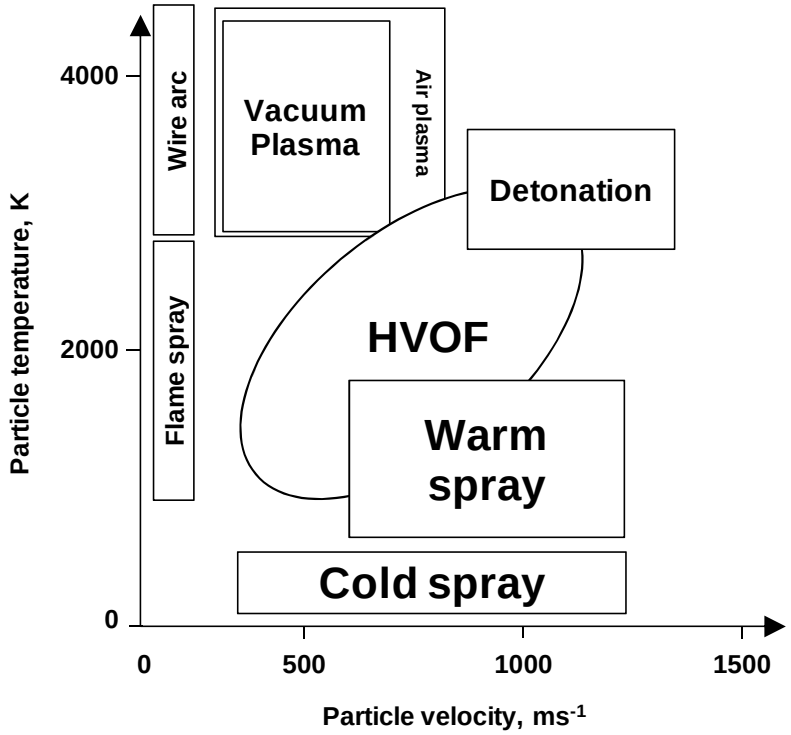

Figure 1.3: A summary of the expected particle velocities and temperatures achieved by the main industrial thermal spray processes. Reference data courtesy of Davies (2004).

High velocity oxygen–fuel (HVOF) thermal spraying was developed in 1930 and has been commercially available for twenty-five years. This continuous spray process has a high material throughput rate compared to other thermal spray processes, and good controllability. The flow field through a HVOF gun is characterized by a complex combination of combustion, compressible supersonic flow, turbulent mixing and gas-particle interactions. A typical HVOF system is initialized at the combustion chamber, where fuel and oxygen are fed in and combusted into a gaseous mixture. These gaseous products are then forced through a nozzle which accelerates them to supersonic velocity. The coating in powder form may either be fed by a carrier gas into the combustion chamber or downstream after the convergent-divergent nozzle. The ability of this process to propel the powder particles at high velocity without overheating them is its most salient feature. The powder particles which most

commonly range in size from 5μm to 80μm are softened or melted by the hot gas while being carried to a targeted substrate to build up coatings up to mm thickness. Like the detonation spray process, it can be used to deposit dense, hard cermets of WC-Co (de Villiers Lovelock, 1998) and Cr_2C_3-NiCr (He et al., 2001), but is also often used in engineering to deposit a variety of metallic alloys (Dent et al., 2000). The coatings produced are generally durable with high bond strength, hardness and wear resistance due to a homogeneous distribution of the sprayed particles within the coating structure (Cheng et al 2001).

The cold gas dynamic spraying (CGDS) process is a relatively new spray coating technique, developed in Novosibirsk, Russia in the mid 1980s by Alkhimov et al. (1990). From the outset it was demonstrated that pure metals, metal alloys, and composite powders can be deposited without extensive heating. As a result the inherent degradation of the powder particles due to overheating, which are commonly found in traditional, high temperature thermal spraying can be largely reduced. These include: high-temperature oxidation, crystallization, and residual tensile stresses due to solidification shrinkage (Papyrin et al. 2007, Dykhuizen & Smith 1998). CGDS is renowned for its simplicity. High pressure gas is accelerated through a de Laval nozzle, and depending on the type of gas, pressure and temperature the gas velocity can easily exceed 1000 ms^{-1}. The powder particles which range in size from 1-50 μm (Papyrin et al. 2007) are accelerated to the substrate by the gas at temperatures below their melting point. Due to the low processing temperatures cold-gas spraying is particularly suitable for depositing ductile materials that can deform plastically without excessive pre-heating, and includes: Cu (Donner et al., 2011), MCrAlY (Stoltenhoff et al., 2001), Al and Zn (Zhao et al., 2006), and Ti (C. –J. Li & W. –Y. Li, 2003). In order to achieve adhesion on impact the particles deform in their solid state, characterized by high strain rates through the material (Balani et al. 2005). The particle velocity on impact is one of the dominant factors controlling the deposition efficiency (W. Y. Li et al. 2008). It has been shown that when a critical velocity (v_c) is exceeded adiabatic shear instabilities form (Assadi et al. 2003, Grujicic et al. 2004). This process involves heat release on impact due to deformation at the interface between the particle and the impingement zone, which induces further thermal softening and in turn induces viscous-like flow (King et al. 2008). This unstable plastic deformation is the dominant mechanism in the bonding between the particle and substrate in cold spray (Bae et al., 2008). The value of V_c can be equated to the relative densities of the particle and substrate, and further relies on their thermal and mechanical properties (Assadi et al. 2003, Schmidt et al. 2006). However, if v_c is not exceeded and the particle fails to deform to an adequate degree erosion at the surface may take place, or the particle

may rebound from the surface, creating material waste and prolonged turnaround times.

A modification of the HVOF process, named warm spray (WS) processing, has been recently developed and is the latest within this family of supersonic devices. By combining a room temperature inert gas with the standard HVOF jet, the temperature of the propellant gas can be controlled in order to deposit powder materials in a thermally softened state at high impact velocity (Kuroda et al., 2011).

When depositing an oxygen sensitive material such as titanium using powder based thermal spray methods, control of the particle temperature and its surrounding environment is crucial. High-velocity oxygen-fuel (HVOF), plasma and wire flame spray are the classic thermal spray techniques which generally operate at temperatures above 3000 K. Their excessive temperatures often melt or partially melt smaller metallic particles before they reach the substrate surface. This overheating has been shown to degrade the coating quality as a result of oxidation at a particle's melted surface, and these levels of oxidation have been shown to increase exponentially when heated beyond 900 K for titanium (Wu et al. 2006). The cold gas dynamic spray (CGDS) technique could potentially resolve the issues of overheating the titanium powder (Papyrin et al. 2007), but the low temperatures associated with this method may impede plastic deformation and inter-particle metallic bonding on impact, and for titanium can result in low deposition efficiencies, high porosities within the coating and premature fatigue crack formation (Price et al. 2006, Marrocco et al. 2006). Both experimental and computational modelling investigations have highlighted the benefits of warming the process gas or powder feedstock in CGDS. The results demonstrate that by softening the powder prior to impact the critical adhesion velocity can be lowered, the adhesion strength can be improved and the deposition efficiency is heightened (Assadi et al. 2003, Klinkov et al. 2005). Despite this, the CGDS process is technically unable to increase the particle temperatures beyond 800 K (Kawakita et al. 2008) because this method relies on heating of the process gases using a heating element, and is without a combustion reaction or plasma ionisation. On the other hand, the temperature of a HVOF thermal spray jet can be controlled using the WS method, as first patented by Browning (Browning, 1992). Over the past few years this idea has re-emerged and developed to help remedy the problems associated with the high and low temperature conditions of HVOF and CGDS respectively. The WS technique has the ability to control the powder particle temperatures, for instance, beyond 800K but below their melting point prior to impingement at the substrate. The control of the carrier gas temperature is achieved in a WS system by injecting a cooling gas at different locations (Kawakita et al. 2006). A review of the WS process can be

found in (Kuroda et al. 2008), which demonstrates that a wide variety of industrially important materials can benefit, including titanium.

Most branches of engineering are currently benefiting from thermal spray coatings to improve a component's performance, to create more advanced functional coatings, and to form complete components. Some of the most common applications of thermal spaying are given in Table 1.1, where the five main applications within different global regions are listed.

China (a)	**Europe (b)**	**Japan (c)**
Corrosion protection (25)	Aeronautics (28)	Machine building (24)
Steel (20)	Automobiles (15)	Printing and paper (15)
Textiles (10)	Processing (13)	Steel structures & bridges (15)
Automobile & engines (10)	Machine building (11)	Steel (14)
Processing (10)	Corrosion protection (10)	Semi-conductors, liquid crystal displays (10)

Table 1.2: Principal industrial sectors in selected countries/regions using thermal spray coatings in order of decreasing percentage of the market. (a) Data courtesy Xiaoou & Yufen (2004), (b) Data courtesy of Ducos & Durand (2001), (c) Data courtesy of Tani & Nakahira (2004).

However, there has always been a growing desire to create smarter coatings which require more and more stringent control over specific coating features. The coatings applied to metallic prosthetic implants for instance, are now combining functionally graded coatings with controlled levels of porosity and dispersed antibacterial agents (Bai et al. 2010). Furthermore, the use of nanometric powders have been shown to improve biocompatibility further in comparison to their micro scale counterparts (Gutwein & Webster 2004, Lima & Marple 2007). The functionally graded aspect of such coatings is used to avoid delamanition of the coating from the substrate, which is believed to be caused by the mismatch of the thermal expansion coefficients between the coating and the substrate materials (Lu et al., 2004). It is not uncommon for a bond coat to be introduced in thermal spray coatings. However, the use of functionally graded coatings in which the composition gradually changes, for example, from TiO_2 to Hydroxyapatite, is difficult to achieve, but has been shown to improve the performance of the coating if correctly applied. Figure 1.4 is an example of a continuous functionally graded coating (Cannillo et al., 2008). This SEM cross-

section reveals the common splat-like morphology of plasma-sprayed ceramics, with the dark lamellae made of hydroxyapatite and the light lamellae of TiO_2.

The induced porosity of a prosthetic implant coating is another key feature, allowing growth of bone tissue into the hydroxyapatite, leading to better biointegration and mechanical stability (Łatka et al. 2010, d'Haese et al. 2010, Simmons et al. 1999). However, the levels of porosity require careful consideration and control in order to maximize biointegration without compromising the coating strength.

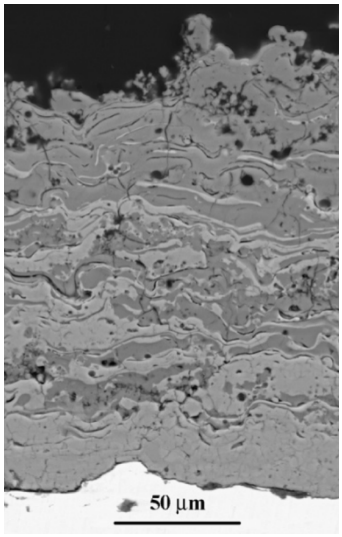

Figure 1.4: Cross-section of the TiO_2–hydoxyapatite graded coating for application in prosthetic implants. Image courtesy of Cannillo et al. (2008).

The manufacture of the dye sensitized solar cell is another good example where more elaborate thermal spray coatings can be beneficial to the advancement of a specific technology. The dye sensitized solar cell, also known as the Gratzel cell (O'Regan & Gratzel, 1991), has a porous nanocrystalline TiO_2 coating which serves as an electrode within the cell system. This is covered and infiltrated by a molecular dye which bonds to the coating's porous surface. The arriving photons which are energetic enough are absorbed by the dye, and cause an electron to be passed from the dye to the conduction band of the titanium dioxide. Features such as the coating thickness, porous volume fraction, crystalline structure, grain size and grain contact condition heavily affect the photocatalytic performance and the current carrying characteristics of the system (Fan et al. 2006, Vaßen et al. 2009). The thermal spray deposition of the nanostructured TiO_2 particles can be carried out by either spraying a previously agglomerated nanoparticle feedstock, or by spraying liquid feedstock with the

dispersed nanometric particles existing as a suspension or dissolved forming a solution (Fauchais et al., 2011).

Solid oxide fuel cells (SOFCs) are high-efficient power converting devices, which can largely benefit from thermal spraying of nanometric particles. Currently, the main difficulties preventing the widespread implementation of SOFCs are the high component and overall manufacturing costs, high performance requirements, long term stability, thermal cycling capability, and long startup times. Operating these units at temperatures far below the traditional 1000°C can provide many advantages over the conventional types, permitting: low-cost peripheral material, increased structural robustness, thermal stability, reduced degradation, and increased flexibility in design and assembly (Oberste-Berghaus et al., 2008). One approach to compensate for the increased resistance to ion transport at lower temperatures within the electrolyte is to reduce the electrolyte thickness. It is crucial that a thin, dense, and fully crystalline electrolyte layer is present to separate the fuel from the oxidant atmosphere (Stöver et al, 2006). The thermal spray deposition of nanometric particles is therefore gaining attention in this field. The liquid feedstock approach allows the deposition of much finer particles to form thinner coatings with a more refined microstructure and grain size (Maric et al., 2011). An example SOFC is given in Figure 1.5. The anode depicted was produced by suspension plasma spraying and the electrolyte was produced by high-velocity oxy-fuel (HVOF) spraying with a liquid suspension feedstock (Oberste-Berghaus et al. 2008).

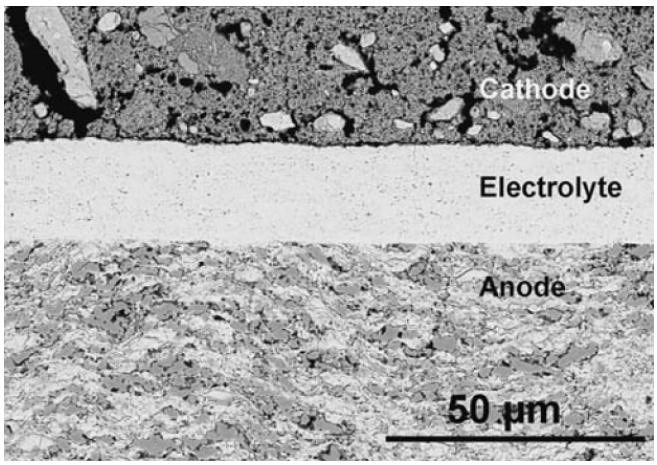

Figure 1.5: An example solid oxide fuel cell produced by liquid feedstock methods. The picture is courtesy of Oberste-Berghaus et al. (2008).

As part of the interest in developing more complex thermal spray coatings, there is a growing desire to deposit nanostructured films. However, the deposition of ultra fine submicron and nano-sized particles requires current techniques to be

adapted. For both health and safety reasons as well as to avoid particle agglomeration during storage and feeding into the spray device, a nano-powder feedstock has to be mixed to form a suspension (suspension thermal spraying, STS) or a solution precursor (solution precursor thermal spraying, SPTS). The liquid injection method also increases the momentum of the feedstock particles, aiding penetration into the thermal jet core. The consistently high levels of interest in the fields of STS and SPTS in recent years is reflected by the number of review papers published (Fauchais et al. 2011, Killinger et al. 2011, Fauchais & Montavon 2010, Pawlowski 2008a, Pawlowski 2009). In all, a variety of thermal spray methods have been utilized in pursuit of depositing nanoparticles from a liquid feedstock, including: plasma, flame, and HVOF. An overview of these achievements is provided as follows.

Hydroxyapatite (HA), TiO_2, and Al_2O_3 are some of the most popular materials being deposited as a liquid feedstock using the plasma spray method. Their respective functions include: prosthetics coatings, photocatalytic devices, and wear and corrosion protection. SPTS of HA using a plasma torch can lead to fine splat morphologies, and demonstrates superior control of coating porosity, which is a key feature of prosthetic coatings (Huang et al. 2010). The deposition of TiO_2 nanoparticles using liquid feedstock plasma spraying has been successfully achieved with grain sizes of roughly 40 nm, and with a high proportion (90%) of desirable anatase phase; vital in the production of photocatalytically active coatings (Vaßen et al. 2009). Liquid feedstock alumina has also been deposited by plasma spraying with controlled coating density and with high levels of thermodynamically stable corundum (α-Al_2O_3); which is necessary for good wear resistance and electrical insulation (Toma et al. 2010).

The flame spray method with liquid feedstock injection has been utilized to both manufacture (Bonini et al. 2002, Mäkelä et al. 2004, Heine & Pratsinis 2005) and deposit TiO_2 nanometric particles. SPTS of TiO_2 using flame spray has successfully created nanostructured coatings, consisting of 80% (C. J. Li et al. 2003) and 95% (G. J. Yang et al. 2005), anatase phase. However, cohesion between particles and their adhesion to the substrate can be limited. The high-velocity suspension flame spray (HVSFS) method, based on existing HVOF technology, has shown a high level of potential for the deposition of submicron and nanosized particles due to its high momentum throughput and controllable flame characteristics which can be utilized to improve the particle impact conditions. As a result, dense TiO_2 coatings with good adhesion to the substrate have been formed (Killinger et al. 2006). Furthermore, Al_2O_3 nanosized particles can be completely melted by this process, resulting in little interlamellar defects and extremely low interconnected porosity (Bolelli et al. 2009). The liquid feedstock HVOF method has also been applied to experimentally

manufacture ceria-based electrolytes for solid-oxide fuel cells, where the flame limits the evaporation and decomposition of the feedstock compared to plasma spray alternatives, producing a low-porosity, smooth and defect free coating (Oberste-Berghaus et al. 2008).

1.2 Project motivations

The coating applications and liquid feedstock methods outlined in Section 1.1 highlight the continuously moving trend of thermal spray coatings towards advanced roles with complex coating architectures. In order to develop the coatings and processing techniques of the future, the science and technology of thermal spraying can benefit from in depth processing information. However, understanding the internal and external dispersed particle and gas flow regimes and the particle morphologies in thermal spray processes is not only restricted by the physical obstructions made by the equipment casing and apparatus, but is also made difficult and often impossible by the extremely high velocities and temperatures at which thermal spray systems often operate. Computational fluid dynamics and numerical modelling enables these complex systems to be visualized, helping to enhance our understanding of how their individual thermal-physical characteristics are affected by a given set of operating conditions such as: the oxygen-fuel mixture in HVOF; the gas pressure and temperature in cold spray or the powder material density and diameter of a powder feedstock. In depth parametric studies can then be carried out, providing a global picture of the system's performance. The numerical approach also provides a foresight which can result in better design and a more immediate understanding of the process parameters in thermal spraying. A large proportion of the physical prototyping and lab based experiments can then be bypassed leading to a short design period.

From details of the thermal-physical and dynamic state of an individual particle at the substrate surface a focused impingement simulation which predicts the build up of the coating microstructure particle by particle can be created. New information describing the deposition process at the substrate may then be built and In turn, can lead to better prediction and control of the coating build-up process.

With a view to improving the fundamental understanding of the thermophysical phenomena occurring through supersonic thermal spray devices with powder based feedstocks, computational modelling is developed and applied in this project to simulate the supersonic gas phase dynamics, particle characteristics and individual particle impingements at the substrate. Each research chapter of this thesis represents a standalone contribution consisting of a concise introduction, modelling approach

and results and discussion sections. These chapters are summarised is Section 1.3 as follows.

1.3 Thesis summary

In order to gain an initial understanding of the flow field through a HVOF type thermal spray system a design analysis was first conducted whereby several geometric parameters were varied. The findings from this study are presented in chapter 2. The investigation conducted led to a published study of the gas phase phenomena through the most widely used liquid fuelled HVOF thermal spray system, the JP5000. Combustion with discrete phase fuel droplets, turbulence, and compressible flow are modelled. The flow field is examined by adjusting the nozzle throat diameter and combustion chamber size. The influence of fuel droplet size on the flame shape and combusting gas flow is further studied.

Chapter three examines the effects of changing the nozzle cross-section and expansion region, particle size and process gas type on the gas flow characteristics through a cold spray nozzle. The spray particle distribution and particle velocity variation at the exit of the nozzle are examined in order to improve the nozzle design and achieve maximum particle velocities. An understanding of the interactions between the nozzle geometry, the process gases, and the powder particles is built in order to improve future cold spray nozzle design.

The relatively new warm spray process is studied in chapter four by introducing a central mixing chamber into the previously investigated HVOF system presented in chapter 2. The effects of injecting a cooling gas on the gas and particle dynamics are examined. The results present a new insight in to the interrelations between the gas and particle phases in warm spray, and highlight the advantage of warm spray for the deposition of oxygen sensitive materials such as titanium.

Chapter five looks into the disintegration of discrete phase water droplets by comparing the time scales of different breakup modes with the rates of evaporation. The results obtained in this chapter give a new insight to the mechanisms which control droplet disintegration within HVOF thermal spraying and serve as a fundamental reference for future development of liquid feedstock devices using water based suspensions.

Chapter six applies the volume of fluid method to simulate the boundary between the metallic and atmospheric-gas phases during the impingement of a molten,

millimeter sized tin droplet impacting at increasing velocities onto a cold, stainless steel substrate. The results shed light on the break-up phenomena on impact and describe in detail how the solidification process varies with an increasing impact velocity. Furthermore, the detailed solidification process is simulated, indicating three unique stages: planar solidification; uneven solidification and wave mixing. The modelling approach from this chapter is developed in chapter seven, and presents for the first time, a simulation of a semi-molten droplet impacting onto a solid substrate, consisting of an undeforming, moving, solid core. The impact, spreading and break-up of a 50 μm zirconia droplet with a solid centre of 30 μm is simulated. The results obtained also visually describe the freezing induced break-up phenomenon at the splat periphery.

2 Gas phase phenomena in liquid fuelled HVOF thermal spraying

Liquid fuelled high-velocity oxygen-fuel (HVOF) thermal spray systems are attractive due to their advantage of producing denser coatings and having higher throughput in comparison to their gas-fuelled counterparts. The flow through a HVOF gun is characterized by a complex array of thermodynamic phenomena involving combustion, turbulence, and compressible flow. Advanced computational models have been developed to gain an insight to the thermochemical processes of thermal spraying, however little work has been reported for the liquid fuelled systems.

In order to gain an initial understanding of the flow field through a HVOF type thermal spray system a design analysis has been conducted whereby several geometric parameters are varied. The study of the gas phase phenomena through the most widely used liquid fuelled HVOF thermal spray system, the JP5000 is therefore carried out. Combustion with discrete phase fuel droplets, turbulence, and compressible flow are modelled. The flow field is examined by adjusting the nozzle throat diameter and combustion chamber size. The influence of fuel droplet size on the flame shape and combusting gas flow is further studied.

2.1 Chapter introduction

HVOF systems are designed to run on either gas or liquid fuels. However, the liquid-fuel HVOF systems (HVOLF) create a greater momentum output which enables the production of denser coatings with a reduced level of porosity and superior corrosion resistance (Zhang et al. 2003). The design of HVOLF systems is more complex because the liquid fuel needs to be atomised and efficient combustion is sometimes difficult to achieve due to the variations in kerosene quality. Advanced computational models have been developed to gain an insight to the thermochemical processes of thermal spraying. A thorough review on modelling developments for HVOF systems can be found in (Cheng et al. 2003). Most research has been focused on gas-fuel systems including work on the HV-2000 (Praxair, US) (Gu et al. 2001) and Diamond Jet (Sulzer-Metco, Switzerland) (M. Li et al. 2004, M. Li & Christphides 2005). The most systematic study of the liquid-fuel system is reported for the METJET (Metallisation, UK) including the combusting gas flow (Kamnis & Gu 2006) and the in-flight particle dynamics (Zeoli et al. 2008). However, these studies are without any discussion on the supersonic characteristics of the flow. For the most widely used

liquid-fuel gun, JP5000 (Praxair, US), only a single numerical investigation was reported in 1996 (Yang & Eidelman 1996), without a vigorous discussion on combustion phenomenon or revelation of the complex flow patterns which occur during HVOF thermal spraying.

The properties of thermal spray coatings are dependent on the physical and chemical state of the powder particles on impact, such as the degree of melting, temperature, velocity, and oxidant content as discussed in Chapter 1. The computational study on METJET has shown that the thermodynamic flow field within the HVOF gun is sensitive to several parameters including the nozzle shape, oxygen-fuel ratio, fuel droplet size and combustion chamber pressure. The design of the thermal spray gun is therefore critical in order to achieve consistency and a high performance from the coating. The METJET has three injection ports for the fuel/oxygen mixture while only one inlet is designed for JP5000. This gives rise to substantial differences for the combustion phenomena and subsequent flow patterns in the combustion chamber between these two guns.

In this chapter the computational fluid dynamics (CFD) approach is applied using the commercial finite-volume CFD package Fluent 6.3 (Fluent. Inc) to model the JP5000 thermal spray system. The investigation is performed in order to gain an understanding of the flow field through a liquid fuelled HVOF type thermal spray system, and examines the effects of gun geometry on the combusting gas flow. The results presented within this chapter focus on kerosene combustion, the formation of supersonic flow phenomenon, and its expansion within the standoff region. By developing a thorough understanding of the thermochemical processes and the interactions between gas and powder within such thermal spray systems a more holistic understanding of the system linking the input system parameters and the final coating structures can be developed; leading to better control of these processes. A first step in such control-mechanisms can be found in M. Li & Christophides (2009).

2.2 Model Description

2.2.1 Model overview

A schematic diagram of the working JP5000 is illustrated in Figure 2.1 highlighting the fuel-oxygen inlet, the combustion chamber, the convergent-divergent (CD) nozzle, and barrel. The position of the powder feeders are shown, but are not included in the simulation. A mixture of fuel and oxygen is injected into the combustion chamber through the central inlet. Unlike the gas-fuel system where

powder is injected into the centre of the combustion chamber, the powder particles are introduced downstream of the CD nozzle using a carrier gas.

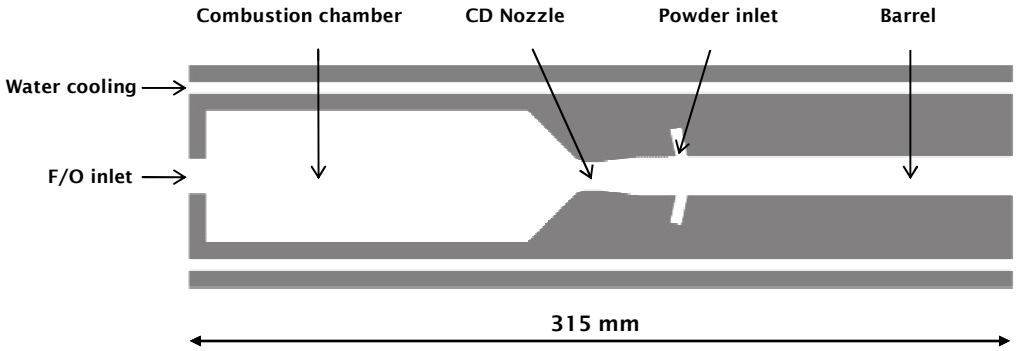

Figure 2.1: Schematic diagram of the JP5000 HVOF thermal spray system

The axisymmetric gun design can be well represented by a 2D simulation domain which is adopted in this study, as depicted in Figure 2.2. The mesh within the combustion chamber consists of 90 axial nodes and 50 radial nodes, and 120 and 115 axial nodes are present for the CD nozzle and barrel respectively. The external region covers a practical stand of distance of 300 mm. The grid around the nozzle and the free jet region has been successively refined in a grid sensitivity study in order to accurately capture steep variations in flow properties due to the effects of compressibility. Further refinement is applied to the oxygen-fuel inlet along the axis to improve the flame contours. Finally, a total of 26,000 cells proved suitable. The geometric parameters and the working conditions for the simulation are summarized in Table 2.1.

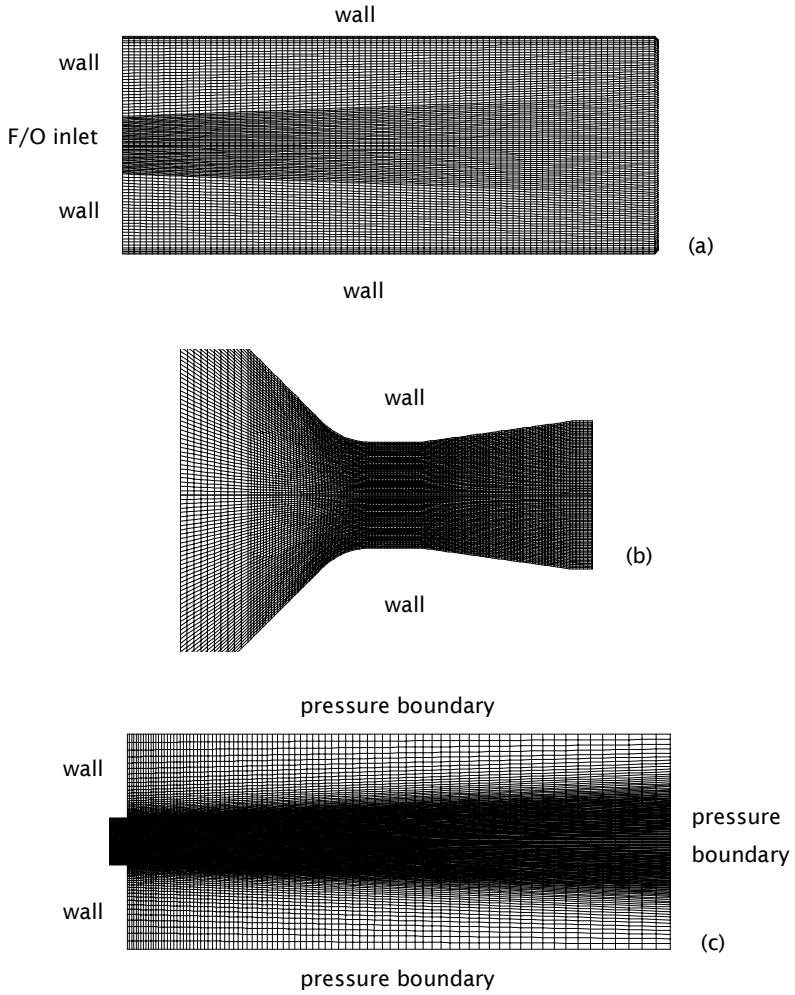

Figure 2.2: Sections of the complete computational grid, highlighting the refinements for the combustion chamber (a), convergent-divergent nozzle (b), and standoff region (c) for the simulation of JP5000 HVOF thermal spray system. Geometric parameters can be found in table 2.1.

Geometric parameter	
Barrel length	111.1 mm
Barrel entrance diameter	11.0 mm
Barrel exit diameter	11.1 mm
Combustion chamber length	92.5 mm
Combustion chamber diameter	37.8 mm
Nozzle throat diameter	7.9 mm
Working conditions	
Fuel	Flow rate: 0.007 kg/s, Temperature: 300 K
Oxygen	Flow rate: 0.022 kg/s, Temperature: 300 K
Atmosphere	Pressure: 101325 Pa, Temperature: 300 K
Internal wall boundary	Temperature: 350 K, Non-slip

Table 2.1: Summary of geometric parameters and working conditions for the JP5000 HVOF thermal spray system

2.2.2 Mathematical models

The numerical modelling techniques for the gas phase phenomena are described mathematically in chapter five, and includes the: continuity, energy and momentum equations, combustion reaction, and turbulence modelling schemes. The fuel droplet modelling is described as follows. The fuel droplets mixed with oxygen are injected evenly spread across the fuel/oxygen inlet into the combustion chamber at the inlet boundary. The acceleration of each droplet particle is calculated using Newton's second law, equating the inertia of each droplet with the forces applied by the continuum, described by Equation 2.1. Subsequently, the trajectory of each droplet is tracked by computing its displacement through time, where the drag force per unit particle mass, $F_D(u-u_p)$, is computed from Equation 2.2. A list of definitions for the mathematical symbols can be found in the nomenclature at the end of this chapter.

$$\frac{du_p}{dt} = F_D(u - u_p) + F_x \tag{2.1}$$

$$F_D = \frac{18\mu}{\rho_p d_p^2} \frac{C_D Re}{24} \tag{2.2}$$

The drag coefficient C_D (Morsi and Alexander, 1972) is given by Equation 2.3 and the relative Reynolds number is defined by Equation 2.4. The values a_1,a_2 and a_3 are listed Table 2.2.

$$C_D = a_1 + \frac{a_2}{Re} + \frac{a_3}{Re^2} \tag{2.3}$$

$$Re = \frac{\rho d_p |u_p - u|}{\mu} \tag{2.4}$$

Re	**a_1**	**a_2**	**a_3**
Re < 0.1	0	24.0	0
0.1 < Re < 1.0	3.69	22.73	0.0903
1.0 < Re < 10.0	1.222	29.1667	-3.8889
10.0 < Re < 100.0	0.6167	46.5	-116.67
100.0 < Re < 1000.0	0.3644	98.33	-2778
1000.0 < Re < 5000.0	0.357	148.62	-4.75×10^4
5000.0 < Re < 10000.0	0.46	-490.546	57.87×10^4
10000.0 < Re < 50000.0	0.5191	-1662.5	5.4167×10^6

Table 2.2: Droplet drag model constants from Morsi & Alexander (1972)

As the droplets are dispersed through the continuous flow field, they exchange mass, momentum and energy. While the trajectory of each droplet is calculated using the mean velocity of the continuous phase, the dispersion of these droplets is deduced by the turbulent velocity component. The number of particles in this model represents the number of tries used by the probability based solver to compute the random effects of turbulence on the discrete droplets. The velocity fluctuations are a function of time and remain constant over a period defined by the characteristic lifetime of an eddy within the continuous phase. The time spent in turbulent motion along the particle path is approximated by the k-ε model using Equation 2.5. This method is discussed in further detail in chapter 3, where a study is conducted for the dispersion of powder particles in cold gas dynamic spraying.

$$T_L = 0.15 \frac{k}{\varepsilon} \tag{2.5}$$

When the temperature of a single droplet within the fuel spray is lower than its vaporization temperature the droplet temperature is controlled by convective heat transfer between itself and the gaseous phase in which it is submersed. The Ranz and Marshall correlation (Ranz & Marshall 1952a, 1952b) given in Equation 2.6 is used to

calculate the convective heat transfer coefficient between the droplet and the gaseous continuum.

$$Nu = \frac{hd_p}{k_\infty} = 2.0 + 0.6Re_d^{\frac{1}{2}}Pr^{\frac{1}{3}} \tag{2.6}$$

When the droplet temperature surpasses the vaporization temperature the vaporization law is initialized and the reduction of the droplet's mass begins to reduce in accordance to Equation 2.7.

$$m_p(t + \Delta t) = m_p\,(t) - N_i A_p M_{\omega,i} \Delta t \tag{2.7}$$

Where,

$$N_i = k_c(C_{i,s} - C_{i,\infty})$$

$$C_{i,s} = \frac{p_{sat}(T_p)}{RT_p}$$

$$C_{i,\infty} = X_i \frac{p_{op}}{RT_\infty}$$

The mass transfer coefficient is evaluated through the Sherwood number correlation (Ranz & Marshall 1952a, 1952b), is given by Equation 2.8.

$$k_c = \frac{D_{i,m}}{d_p}\left(2.0 + 0.6Re_d^{\frac{1}{2}}Sc^{\frac{1}{3}}\right) \tag{2.8}$$

The following assumptions have been applied to the modelling of the fluid droplets:

- The volume fraction occupied by the liquid fuel droplets is sufficiently small i.e. less than 10 percent. Therefore the number of collisions between liquid droplets is presumed negligible. Their volumes in space are simply modelled as overlapping without physical interaction, and therefore the droplets do not collide or coalesce.

- The droplets do not break up into smaller elements, even during evaporation. The droplets do not react while in their liquid phase before evaporating.

- The density of the droplets is much higher than the gaseous phase. Hence the effect of the pressure gradient force and the virtual mass force are neglected.

- The impact of gravity is neglected due to high horizontal velocities and high velocity gradients within a relatively small domain.

- Liquid sprays reportedly radiate negligibly (Williams 1988) and therefore a radiation model is omitted.

- The fuel droplets remain spherical.

- All droplets are identical at the inlet, with the same diameter and temperature.

- The liquid droplets are assumed to have negligible internal thermal resistance and therefore have a uniform temperature throughout.

- The partial pressure of fuel vapour at the surface of each droplet is equal to the saturated vapour pressure at the temperature of the liquid droplet.

2.3 Results and Discussion

A comparison between the model prediction and temperature measurements at the exit of the JP5000 thermal spray gun (Swank et al. 1995) are given in Figure 2.3, showing a good level of agreement between the computational and experimental results. Further comparisons can be found in Chapter 5.

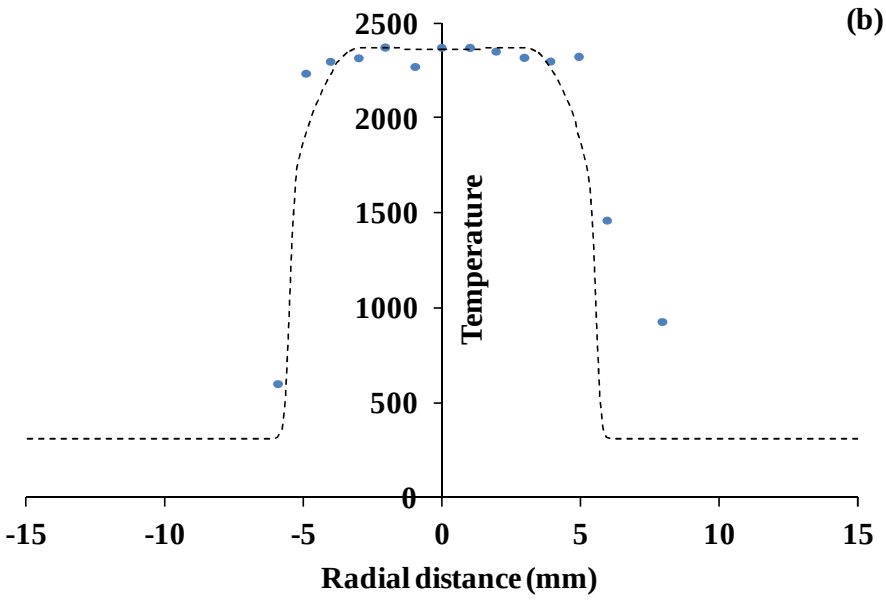

Figure 2.3: Comparison between point measured and CFD simulated gas phase temperatures at the barrel exit of JP5000

2.3.1 Gas flow characteristics

The steady state flame is shown in Figure 2.4. The flame itself is detached from the inlet port with an expected conical heating zone. The combustion reaction relies on the evaporation of the fuel droplets, and this evaporation process occurs most rapidly at the outside edge of the inlet jet stream, owing to the higher temperature of the gaseous mixture in this region.

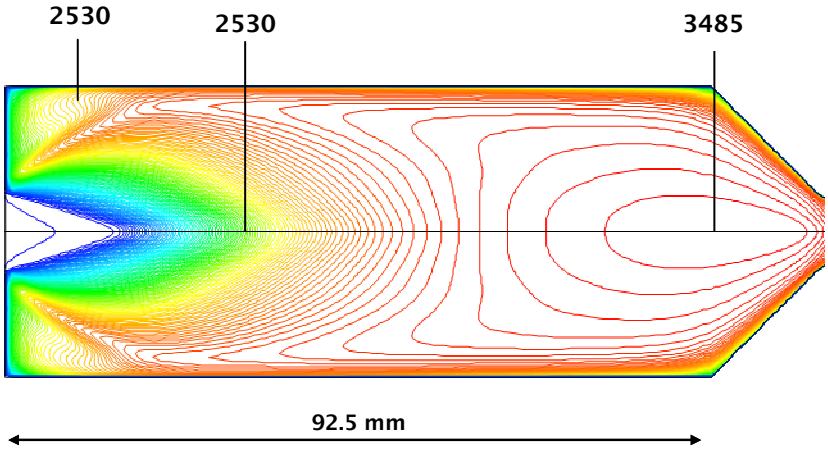

Figure 2.4: Temperature contours through the JP5000 combustion chamber

In liquid-spray combustion the development of a flame can be summarized by a primary preheating zone (warming of liquid droplets), secondary heating zone (warming of liquid droplets and vaporisation), and a reaction zone. The chemical reaction is initiated when the gaseous fuel and oxygen reach their activation energy, and may occur simultaneously with the second preheat zone in the case of larger, less volatile droplets. However, the employed eddy-dissipation turbulent-chemistry model (Magnussen & Hjertager 1976) initiates a reaction as soon as evaporation occurs and therefore completely overlaps the second preheat zone, as illustrated in Figure 2.5.

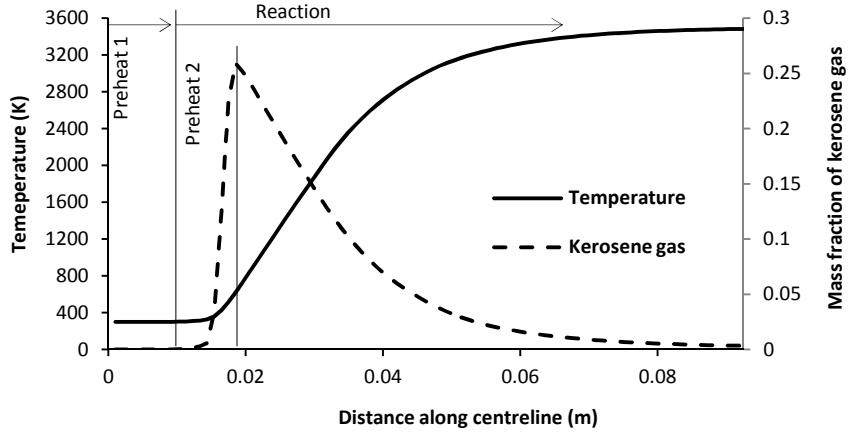

Figure 2.5: Graphical representation of the simulated flame development within the combustion chamber of the JP5000 HVOF thermal spray system.

The compressed gases under high pressure are forced through the CD nozzle and a rapid rise in velocity occurs. At the throat the flow is chocked at mach one. Two small shocks follow as the gas expands and accelerates through the divergent section, marked by slight increases in temperature along the centreline, as shown in Figure 2.6.

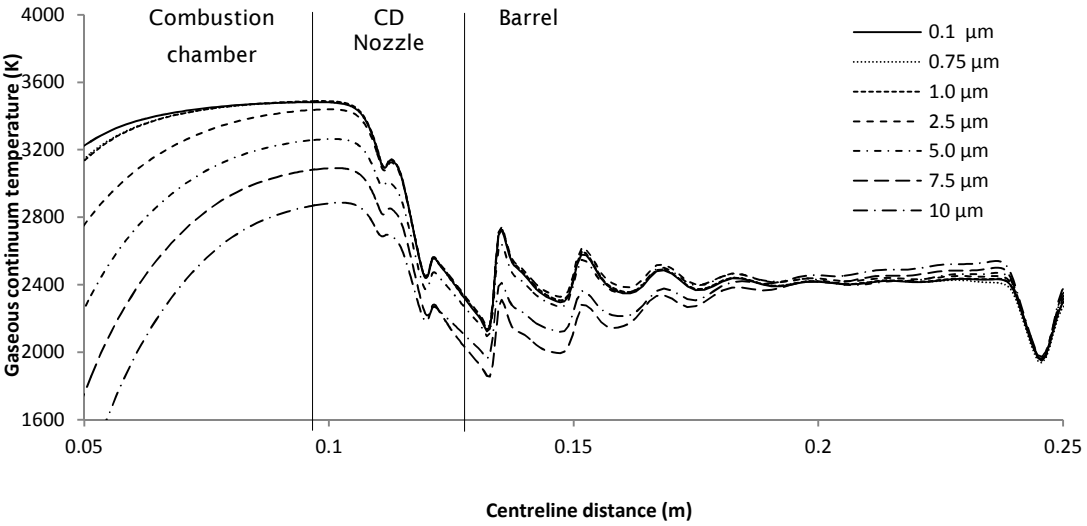

Figure 2.6: Modelled centreline temperature profile through the JP5000 for different fuel droplet sizes.

Shock patterns occur at the exit of the CD nozzle due to the expansion of the supersonic gas and strong reflections at the solid internal surface of the barrel, which again are characterized by fluctuations in temperature along the centreline plot in Figure 2.6. An under expanded flow regime at the exit of the barrel is present, enforced by a slightly subcritical atmospheric back pressure. The fluctuations in

velocity and pressure at the exit of the barrel are created by the flow periodically over expanding and then re-converging above and below atmospheric pressure, as depicted in Figure 2.7. These adjustments continually overshoot due to the boundary communicating with the jet by sound waves, which naturally travel slower than the bulk supersonic flow. Criss-cross shock waves form shock diamonds created by converging sound waves. Rarefaction fans spray around the corners of the barrel exit and the oscillating jet boundary, as shown in Figure 2.7. As the gas jet passes through the region of rarefaction fans it is expanded and cooled, and through the shock diamonds, the gas is compressed and heated. The convergence points of the incident shocks at the centreline are marked by peaks on the centreline velocity profiles in Figure 2.8.

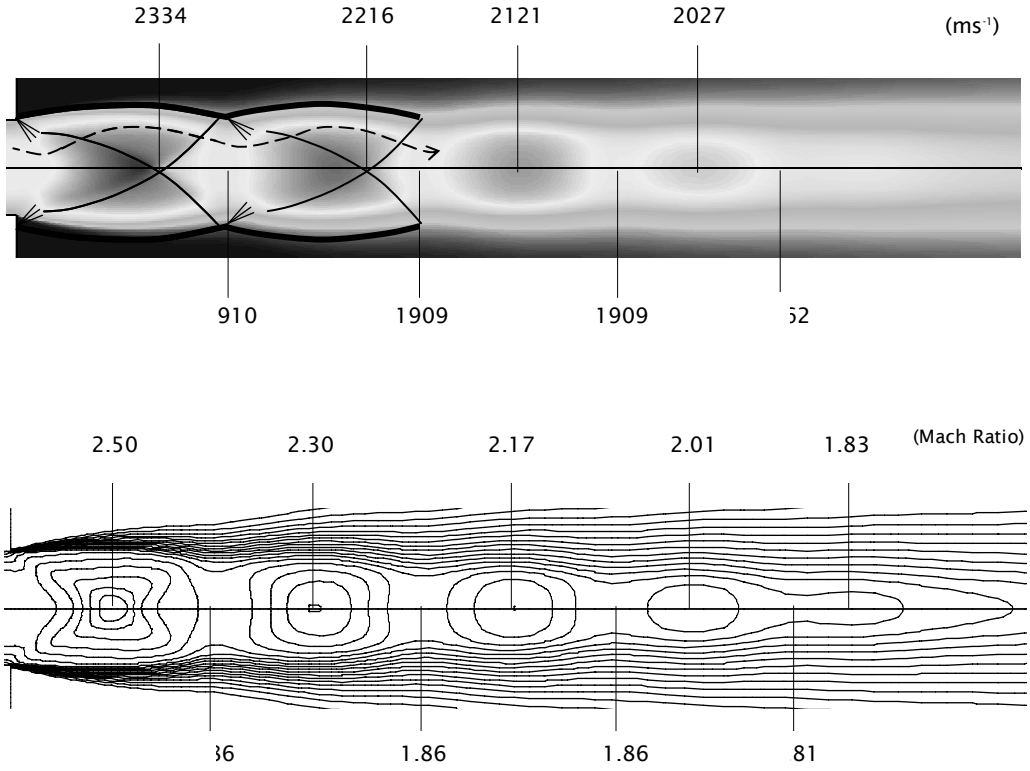

Figure 2.7: Variations in velocity (top) and Mach number (bottom) through the expanded jet at the exit of the JP5000 barrel.

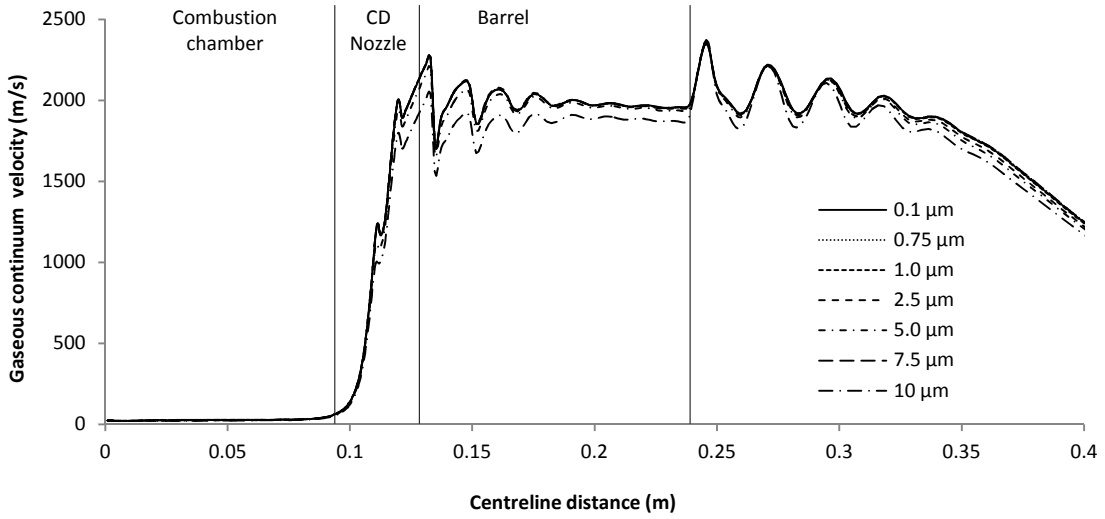

Figure 2.8: Variation in simulated gaseous velocity along the centreline of the JP5000 for different fuel droplet sizes

2.3.2 Fuel droplet size

The gas flow characteristics are evaluated by varying the fuel spray droplet diameter between an unrealistically low 0.1 µm and 10 µm. The results show that for fuel droplets less than 5µm the fuel completely reacts within the combustion chamber. However, above this size, a small amount of gaseous fuel at the centre of the flame enters the CD nozzle and continues to react, as depicted in Figure 2.9. For this reason there is a noticeable difference in the gas temperature profile through the combustion chamber, CD nozzle and through the first half of the barrel for droplets of 5µm diameter and above (Figure 2.6). Half way along the barrel the fuel has completed reacted and the flow regimes for each case converge to similar values. The velocity regimes through the system are less sensitive to the unburnt gaseous fuel and for cases where the fuel droplet diameter is 7.5 µm and less the velocity profile is negligibly affected. For the 10µm case the largest amount of fuel exits the combustion chamber causing a reduction of roughly 100 ms^{-1} throughout the system (Figure 2.8).

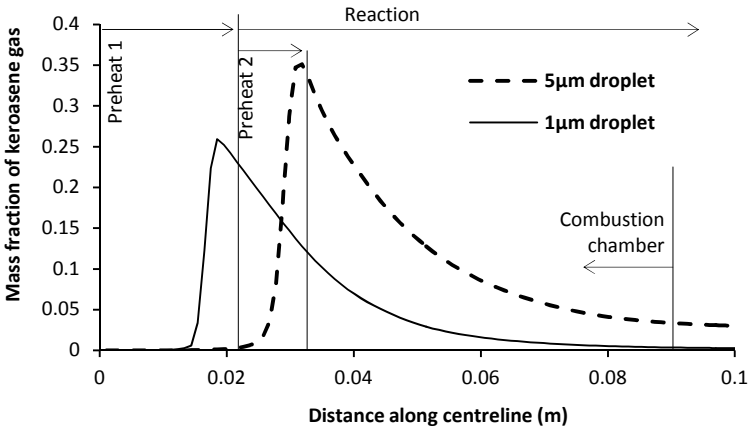

Figure 2.9: Flame development for 5µm droplet scenario with 1µm comparison

The radial temperature profiles through the combustion chamber at quarterly intervals along the centreline (Figure 2.10) quantify the variations in flame shape for varying droplet size, and show that for droplets below 1 µm there is negligible difference in flame shape. On the other hand, for droplets greater than 1 µm the total evaporation rate is reduced due to a smaller total surface area. As a result the flame is stretched along the centre of the combustion chamber.

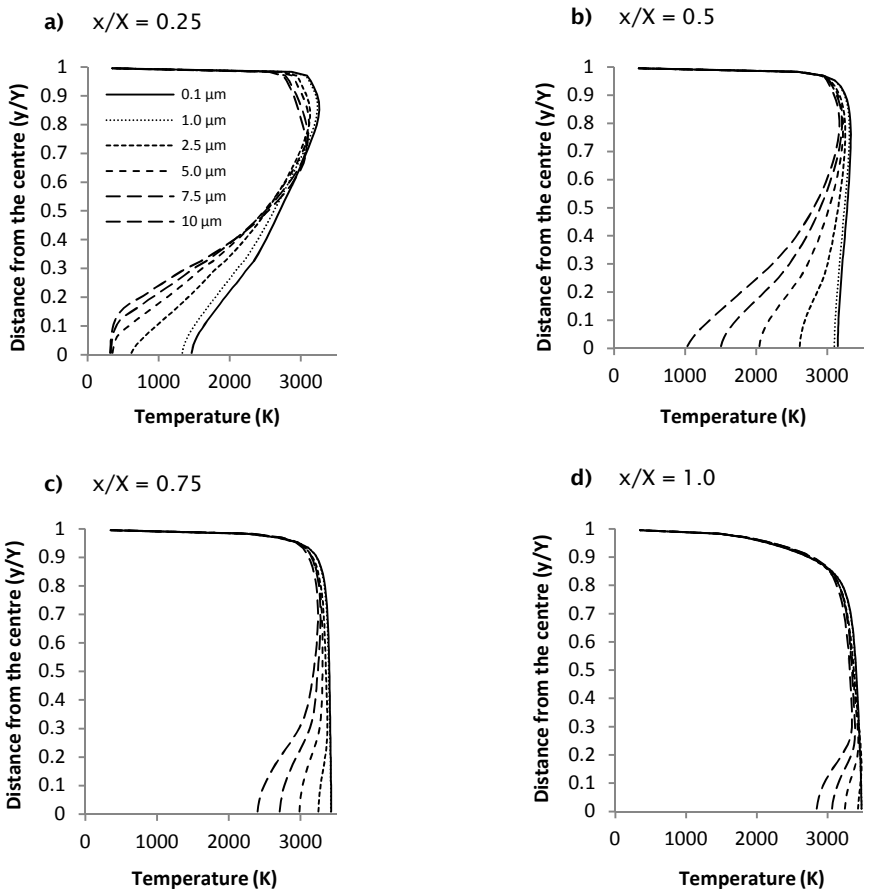

Figure 2.10: Radial temperature profiles at quarterly intervals through the combustion chamber for variations in fuel droplet sizes

At the first quarter the 10 µm, 7.5 µm and 5.0 µm droplet scenarios are in their preheating stage along the centreline and hence the continuum is yet to experience an increase in temperature. However, the preheating zones for the 2.5 µm, 1.0 µm and 0.1 µm droplets are surpassed by this stage and the temperature of the gaseous continuum has risen due to chemical reaction. The temperature profiles for the different droplet scenarios converge roughly half way along the radial distance from the centreline and this pattern is repeated along the length of the combustion chamber, suggesting that varying the droplet size would make a negligible impact on the amount of energy dissipated through the combustion chamber surface.

Figure 2.11 illustrates the recirculation zones at the inlet end of the combustion chamber, and show that for larger droplets the size of the recirculation region is increased. However, due to lower rates of evaporation and a lower rate of production of gaseous products the intensity is reduced. In this zone the velocities are relatively low and at the corner of the combustion chamber soot accumulation is likely to occur. The sharp corner also creates an area of high stress concentration. In some HVOF designs it may be chamfered, which helps to alleviate these problems. However, the

flame within the combustion chamber may tend to be drawn to the wall if the chamfer resides to close, leading to inefficient combustion.

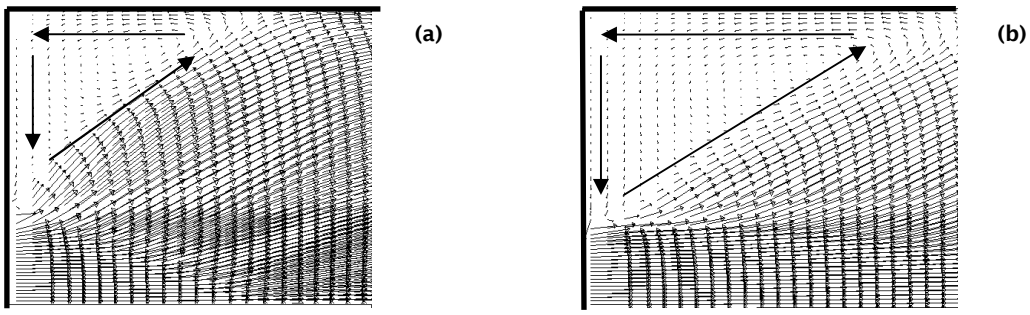

Figure 2.11: Corner recirculation in the JP5000 combustion chambers for the injection of 0.1 μm fuel droplets (a) and 10 μm fuel droplets (b)

2.3.3 Throat diameter

The diameter at the throat of the convergent-divergent nozzle is increased and decreased by 20% in order to investigate the impact on the flow regime. Figures 2.12 and 2.13 show that such changes make a negligible impact on the upstream flow profiles within the combustion chamber, however the gas flow characteristics are largely altered through the CD nozzle, within the barrel and at the barrel exit. At the exit the difference in pressure and back pressure determines the type and intensity of the flow regime. Greater velocity oscillations at the exit of the barrel imply a greater degree of mixing and axial momentum reduction for the gaseous flow. By increasing the flow velocity the pressure of the flow at the exit of the barrel can be reduced towards atmospheric pressure and as a result the magnitude of the fluctuations in velocity and temperature which are brought about by the under-expanded flow regime can be lowered.

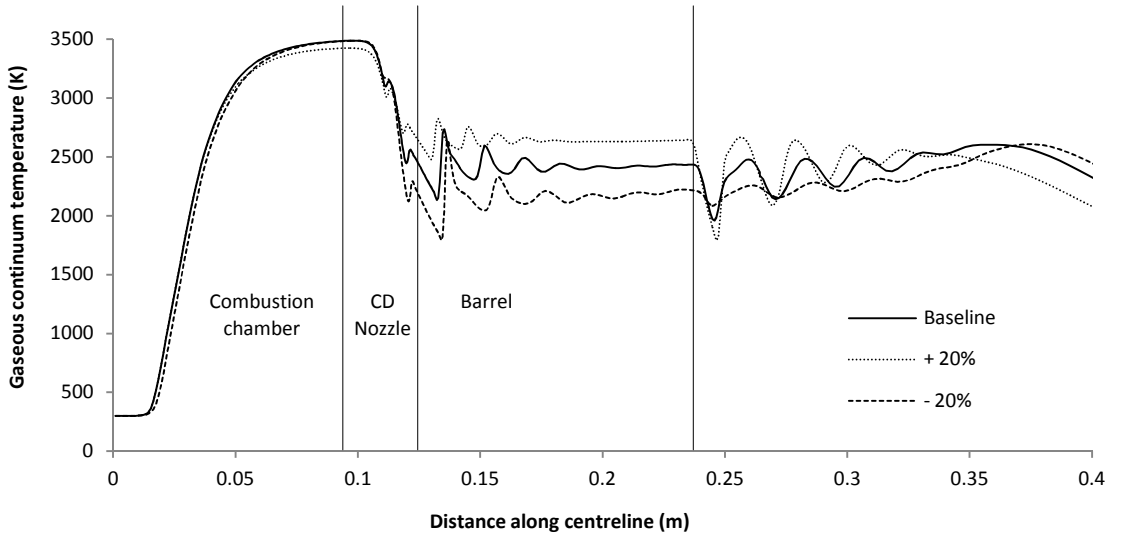

Figure 2.12: Simulated variation in gaseous continuum temperature along the centreline of the JP5000 for different nozzle throat diamters.

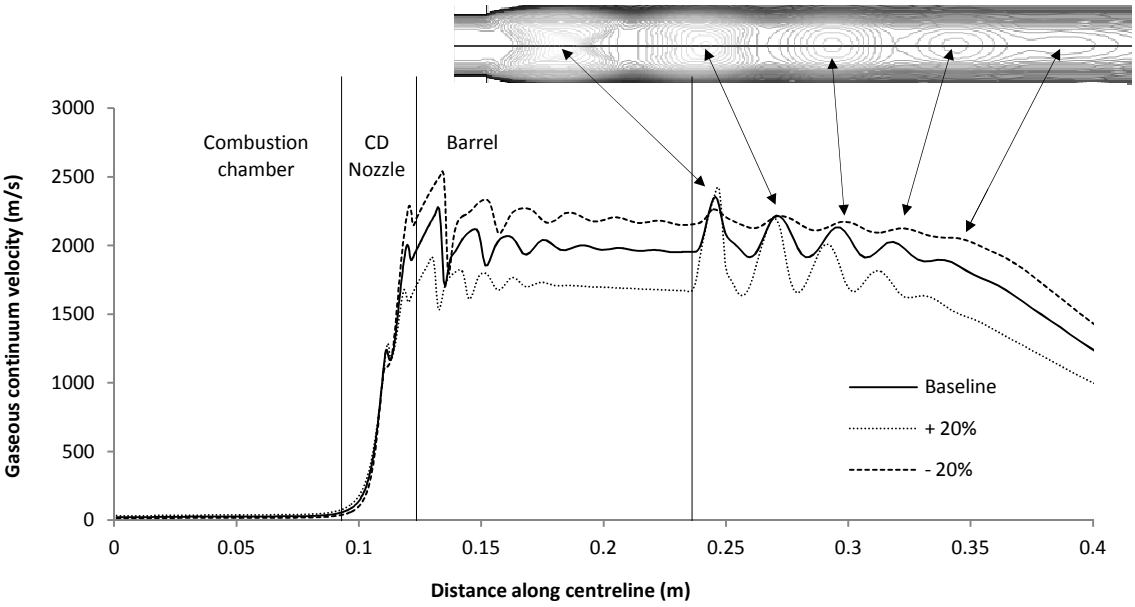

Figure 2.13: Simulated variation in gaseous continuum velocity along the centreline of the JP5000 for different nozzle configurations

By increasing or decreasing the throat diameter the gaseous products in the combustion chamber are compressed to a lesser or greater degree respectively. For an increase in compression higher velocities can be attained through the system. An increase in kinetic energy incurs a decrease in thermal energy and hence a lower temperature profile for a faster travelling gas flow is produced. Figure 2.12 highlights the importance of the exterior jet design as this region contributes significantly to the powder particle heating. The 20% decrease in throat diameter creates a flow of almost

perfect design condition which is only slightly under-expanded. As a result the temperature and velocity oscillations diminish due to less intense rarefaction waves.

This design alteration maximizes the gas velocity in the free jet region and at the same time could help prevent overheating of the powder particles. However, the reduction in throat diameter not only enforces an increase in velocity downstream but also causes a compression of upstream gas, which effectively heightens the combustion chamber pressure. Results indicate that a 20% reduction in throat diameter will induce roughly a 60% increase in pressure inside the combustion chamber. By altering the CD nozzle throat diameter the combustion chamber pressure is significantly altered and therefore this requires careful consideration.

2.3.4 Combustion chamber size

The combustion chamber length is gradually reduced in 20% increments and the effects on the gas flow are investigated. By reducing the combustion chamber length by 40% the velocity and temperature profiles through the system are unaltered. However, for a reduction of 60% a large percentage of fuel enters the CD nozzle as quantified by Fig 2.14.

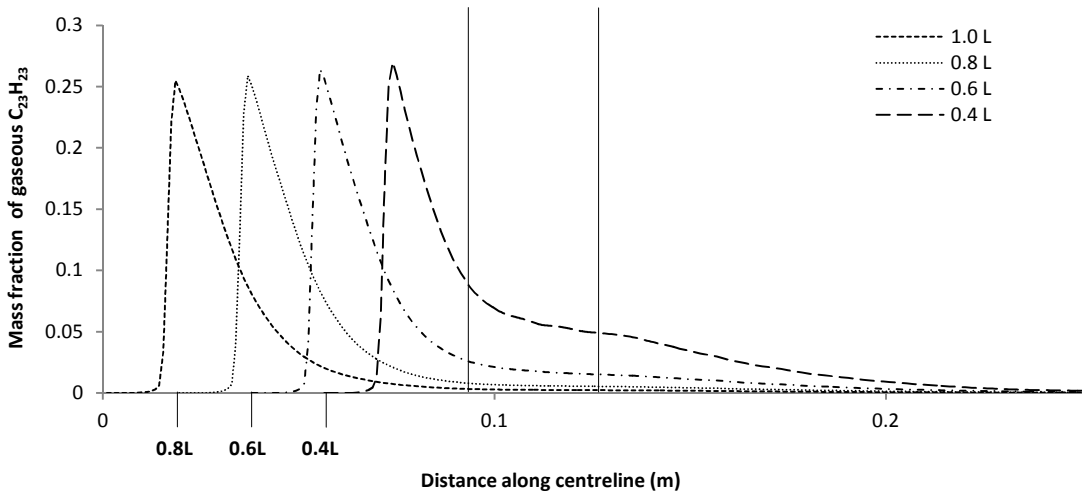

Figure 2.14: Mass fraction of gaseous fuel along the centreline for each combustion chamber length reduction

The gaseous fuel which escapes the combustion chamber continues to react through the nozzle and barrel. Comparing the reaction rate with the corresponding velocity profile for the 60% reduction shows the reaction rate peaking when the flow

experiences a shock (Figure 2.15). This phenomenon is created by heightened levels of turbulence in areas of steep velocity gradients.

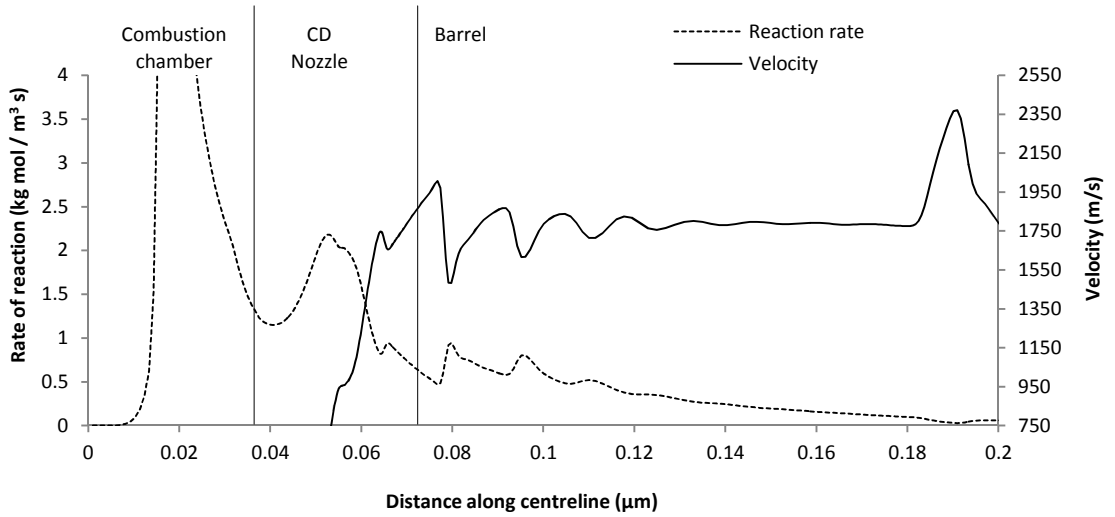

Figure 2.15: Comparison of reaction rate and velocity fluctuations along the centreline for L = 40%

Radial temperature profiles at quarterly intervals through the combustion chamber for the four different combustion chamber lengths (Figure 2.16) show little variation when the combustion chamber is reduced by 20%. With a 40% reduction only a small amount of fuel exits the combustion chamber and leads to a slightly lower than expected temperature at the exit of the combustion chamber along the centreline (Figure 16c).

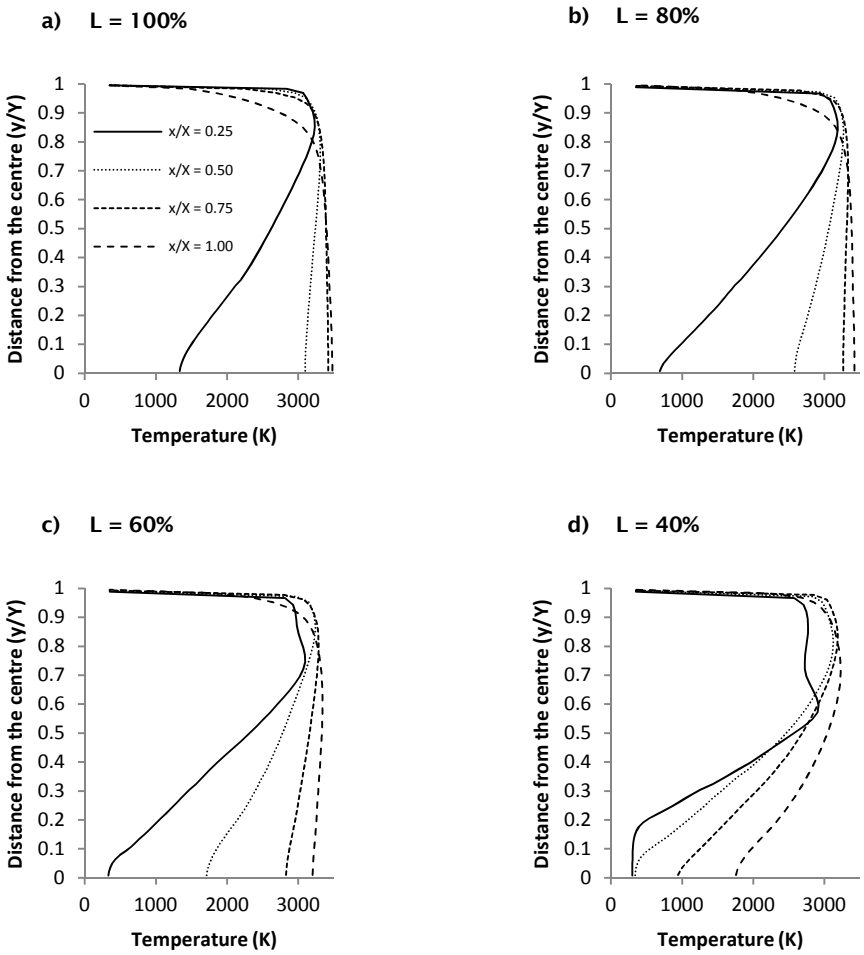

Figure 2.16: Radial temperature profiles at quarterly intervals through the combustion for each tested combustion chamber length

The reduced temperature profiles in Figures 2.16c and 2.16d at the first quarter highlight the presence of recirculation zones. These regions reduce the temperature near the wall and therefore help to reduce the amount of energy dissipated through the internal surface. The size and intensity of the recirculation region remains unaffected by the changes in combustion chamber length and therefore gradually covers a larger proportion of the internal surface as the length of the combustion chamber is reduced.

Results from this investigation indicate a reduction in the combustion chamber length by 20% for the baseline model is possible without risking an excessive amount of fuel exiting the combustion chamber, and this reduction can be expected to make a negligible difference to the temperature and velocity profiles through the system. The heat transferred through the internal surface of the combustion chamber can be expected to be reduced by at least the same factor due to the surface area reduction as well as the larger proportion of recirculation at the surface.

2.4 Conclusion

A premixed steady-state flame and compressible combustion flow has been simulated within the kerosene-fuelled JP5000 HVOF thermal spray system, using the commercial CFD code, Fluent 6.3. The results drawn from this model are summarized as follows.

The core of the flame is significantly stretched by larger droplets. For fuel droplets greater than 5μm there is a risk of combustion occurring through convergent divergent nozzle and barrel, which largely reduces the temperature around the powder inlet. However, for smaller droplets there is a negligible difference in velocity and temperature profiles through the system. Therefore, given the applied flow rates the fuel should be atomized below 5μm in order to achieve an optimum working performance. The degree of atomization is unlikely to make a significant difference on the heat conducted through the internal surface of the combustion chamber for droplets varying between 0.1 and 10 μm.

The velocity of the gas flow beyond the combustion chamber is increased by reducing the throat diameter of the convergent-divergent nozzle. The intensity of the under-expanded shock regime at the exit of the barrel is also reduced. A 20% decrease in throat diameter creates a flow of almost perfect design condition. However, this reduction heightens the combustion chamber pressure by 60%.

A reduction in the combustion chamber length by 20% for the baseline model is possible without excessive fuel exiting the combustion chamber. This reduction makes a negligible difference to the temperature and velocity profiles through the system. The heat transferred through the internal surface of the combustion chamber can be expected to be reduced by at least the same factor due to the surface area reduction as well as the larger proportion of recirculation at the surface.

2.5 Chapter nomenclature

General symbols

A_p	surface area of a droplet (m^2)
$a_{1,2,3}$	drag coefficient constants
C_D	drag coefficient
d	diameter (m)
$D_{i,m}$	diffusion coefficient of vapour in the bulk flow ($m^2 s^{-1}$)
F_D	drag force coefficient
F_x	additional acceleration term ($N kg^{-1}$)
h	convective heat transfer coefficient ($W m^{-2} K^{-1}$)
k	turbulent kinetic energy ($m^2 s^{-2}$)
K_∞	thermal conductivity of the continuous phase ($W m^{-1} K^{-1}$)
K_c	mass transfer coefficient ($m s^{-1}$)
m_p	mass of particle (kg)
$M_{w,i}$	molecular weight of species i ($kg mol^{-1}$)
N_i	molar flux of vapour ($mol m^{-2} s^{-1}$)
Nu	Nusselt number
P_{op}	operating pressure (Pa)
Pr	Prandtl number
P_{sat}	saturated pressure (Pa)
R	universal gas constant ($J K^{-1} mol^{-1}$)
Re	Reynolds number
Re_d	Reynolds number based on the particle diameter
s	particle path
Sc	Schmidt number
t	time (s)
T	temperature (K)
T_L	Lagrangian time integral
u	velocity ($m s^{-1}$)
X_i	local bulk mole fraction

Greek symbols

ε	turbulence dissipation rate ($m^2 s^{-3}$)
μ	viscosity ($kg m^{-1} s^{-1}$)
ρ	density ($kg m^{-3}$)

3 Process optimization of cold gas spraying

Cold gas dynamic spraying is a relatively new spray coating technique capable of depositing a variety of materials without extensive heating. As a result the inherent degradation of the powder particles found during traditional thermal spraying can be avoided. The simplicity of this technique is its most salient feature. High pressure gas is accelerated through a convergent-divergent nozzle up to supersonic velocity. The powder particles are carried to the substrate by the gas and on impact the particles deform at temperatures below their melting point. In this chapter the computational fluid dynamic approach is adopted to systematically examine the effects of changing the nozzle cross-section shape, particle size and process gas type on the gas flow characteristics through a cold spray nozzle, as well as the spray distribution and particle velocity variation at the exit.

3.1 Chapter introduction

Several computational fluid dynamic (CFD) models have been utilized in the development of cold spray, and due to the common cold spray nozzle having a circular cross-section the majority of these studies adopt a two-dimensional axisymmetric domain. Amongst these, investigations include geometric optimization of the de Laval nozzle by varying the length and expansion-ratio (W. Y. Li & Li 2005, Li et al. 2006, Li et al. 2007) as well as testing the effects of stand off distance and the bow shock phenomena on particle impact velocity (W. Y. Li et al. 2008, Pattison et al. 2008). Powder particle velocity has also been shown to be effected by the particle size (W. Y. Li et al. 2008, W. Y. Li & Li 2005, W. Y. Li et al. 2007, Pattison et al. 2008, Jen et al. 2005) and the type of material being sprayed (W. Y. Li et al. 2008, Pattison et al. 2008, Jen et al. 2005, Katanoda et al. 2007).

Several research papers have been targeted at optimizing the geometry of conical nozzles, including (W. Y. Li & Li 2005, W. Y. Li et al. 2006, W. Y. Li et al. 2007). However, there have been few steps taken to investigate the possibility of designing a more complex contour shape. Some early work undertaken by Dykhuizen & Smith (1998) to optimize the nozzle cross sectional area through the coupling of the isentropic flow equations and the particle drag force was conducted in one dimension.

In this chapter the method of characteristics (MOC) is utilised in order to numerically test a minimum length, axisymmetric de Laval (CD) nozzle with a contoured diverging section. Its performance is numerically simulated and compared alongside an equivalent conical design with nitrogen as the process gas at a stagnation

pressure and temperature of 3 MPa and 300 K. Spherical, 11 μm, copper particles are tracked through the gas phase along the centreline and their dynamic response is viewed for both the conical and contoured scenarios.

A small amount of 3D CFD modelling has been applied previously to cold spray (Karimi et al. 2006), which successfully simulates the compressible flow through a de Laval nozzle. However, this study is without nozzle design development and lacks vigorous scientific discussion concerning the compressible flow and particle interactions. Rather, the investigation is focused on the novel development of a CFD tool for numerically simulating and then post processing and visualizing particle concentrations outside of the nozzle. The computational time and resource required to produce a realistic 3D model is limiting the depth of research in this field. In particular 2D models are unable to simulate a realistic particle distribution, and design developments have to exclude cross-section shape variations which are not axisymmetric.

In this chapter, full three dimensional simulations are constructed for investigation and are used to simulate the particle laden flow through various cold spray nozzles. The 3D models are utilized to investigate the particle distributions at the nozzle exit for nitrogen and helium gas flow and for different size particles. Furthermore, circular, square, and elliptical nozzle cross sections are simulated to test their effect on the particle dynamic response.

In summary, the CFD approach is applied in this study in 2D when simulating a single particle trajectory and 3D when simulating particle dispersion. The chapter examines how certain nozzle design modifications impact on the gas flow behaviour and powder particle velocity variation and distribution. Meanwhile, an extended study explores the effect of feedstock particle size and process gas type. The study is strengthened by comparison to state of the art experimental measurements of particle size and their associated in-flight velocities. The particle exit velocity is directly related to the deposition efficiency in the application of cold spray, and therefore acts as a useful indicator for industrial application.

3.2 Model description

3.2.1 Model overview

Geometric parameter	Length (mm)
Throat Diameter	1.35
Nozzle Entrance Diameter	13
Nozzle Exit Diameter	4
Length of Converging Section	10
Length of Diverging Section	100

Table 3.1: Baseline model geometric parameters for the working cold spray nozzle

An axisymmetric view of the cold spray nozzle and exterior region is illustrated in Figure 3.1, which summarizes the boundary conditions for the 3D computational domain. The geometric parameters for the baseline model are provided in Table 3.1, which are based on a working circular cross section cold spray nozzle, as published in (Price et al. 2007). The experimental methodology incorporated in this study is outlined in Section 3.3. For the 3D simulations, the powder particles are introduced into the computation domain via a 1mm x 1mm region as highlighted in Figure 3.1.

a)

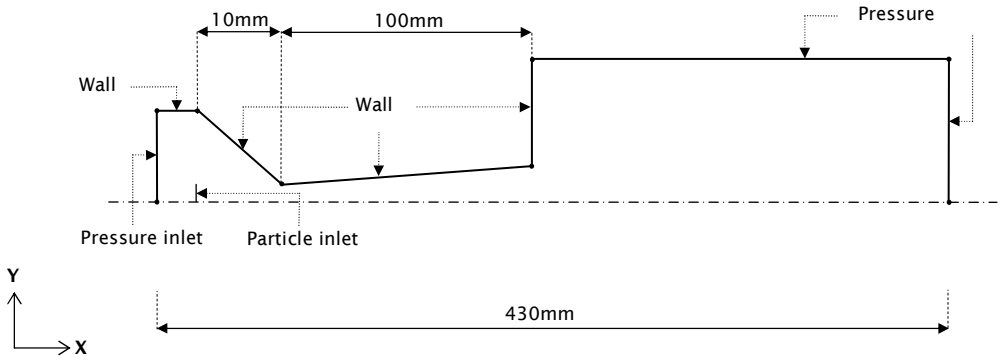

b)

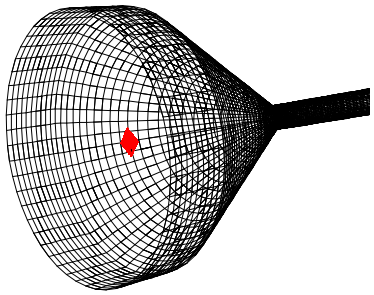

Figure 3.1: An axisymmetric view of the computational boundary conditions for the cold spray nozzle (a) and the highlighted location of particle inlet surface (b)

Figure 3.2 exhibits the computational grid around the gas inlet, the de Laval nozzle throat and at the nozzle exit. The grid around the nozzle throat and the free jet region is refined in order to accurately capture steep variations in flow properties due to the compressible nature of the flow. A grid sensitivity analysis was carried out whereby the grid was successively refined by increasing the number of computational cells until the magnitude of the axial velocity through the nozzle changed by less the 1% when compared to the previous refinement. This process deemed a total of 800,000 computational cells to be adequate.

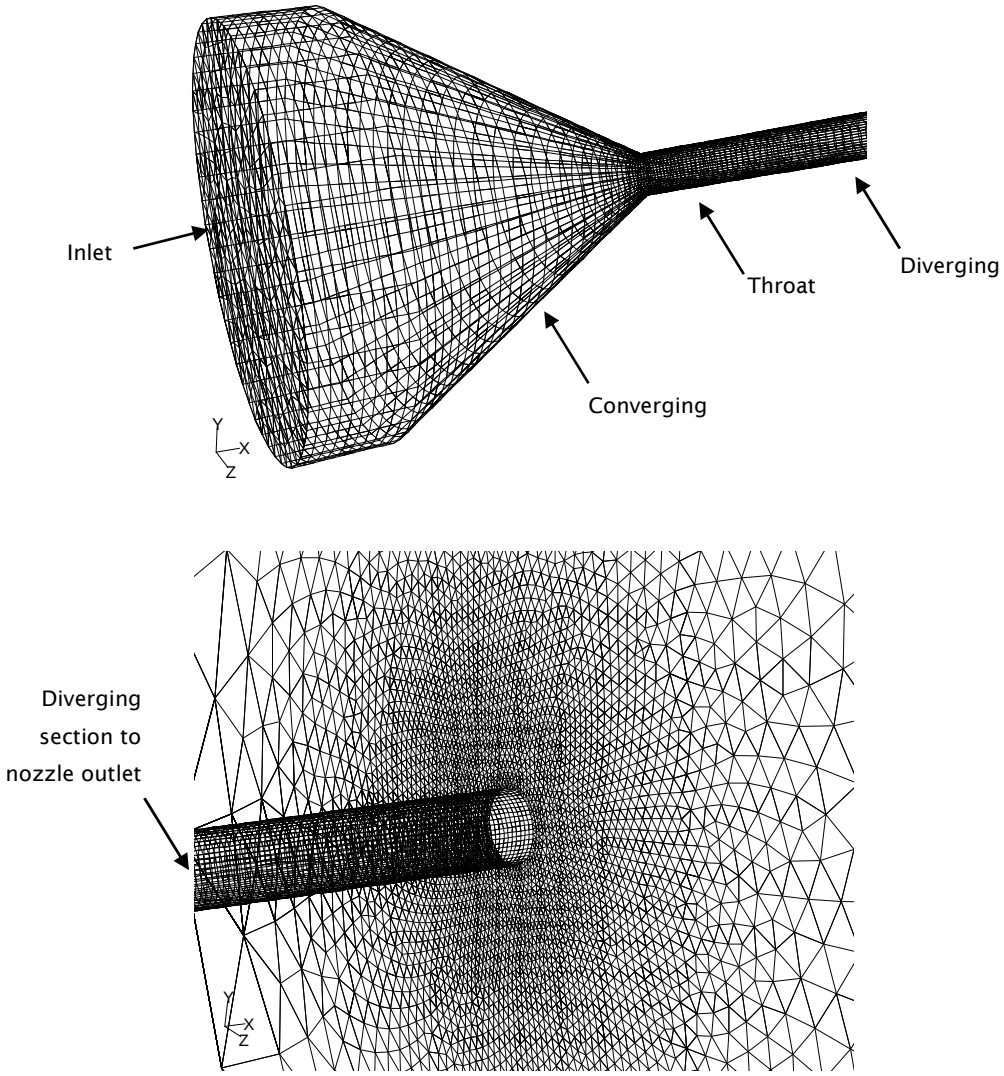

Figure 3.2: Illustration of the three dimensional computational grid for simulating cold spray nozzle, including: the converging section, the nozzle throat, the diverging section and a close up of the nozzle exit.

The commercial finite-volume CFD package Fluent 6.3 (Fluent. Inc) is used to model a steady-state compressible gas flow with discrete phase particles. The inlet and exterior regions are modelled using pressure boundaries. A non-slip condition is applied at the nozzle wall surface, which is also treated as adiabatic. To avoid strong coupling between the pressure and velocity the pressure-based segregated solution algorithm is applied (Vandoormaal et al. 1987), whereby the solution variables (velocity components, pressure, temperature, turbulence scalars) are solved one after another. The velocity and pressure are coupled using the semi-implicit method for pressure linked equations (SIMPLE) algorithm (Peric 1990, Raithby & Schneider 1979), which obtains an estimate of the pressure field using a guess and correct procedure. The transport equations are discretized using a second-order accurate upwind scheme. A description of the realizable k-ε turbulence model, applied for this investigation is

given in Chapter 5 and an overview of the aforementioned numerical schemes can be found in the appendix of this thesis. The discrete phase particle history is computed in a Lagrangian reference frame by coupling the properties of the fluid at the cell in which the particle resides with those of the instantaneous particle properties.

3.2.2 Discrete phase model

The trajectory of spherical copper (Cu) particles is simulated and the material properties are summarized in Table 3.2. The initial injection particle velocity of 20 ms^{-1} is deemed reasonable when compared to calculated values in HVOF (Katanoda et al. 2004) which are estimated to vary between 60 and 33 ms^{-1} for particles between 10 and 50 μm.

The discrete phase particles are injected into the domain at the convergent-divergent nozzle using an artificial surface, as illustrated in Figure 3.1. The trajectory of each particle is calculated using Newton's second law, equating the inertia of each particle with the forces applied by the continuum. As outlined by Crowe (Crowe et al. 1998), for particle laden flows where the relative Mach number M_r exceeds 0.6 shock patterns form on the micro-sized particles. Therefore, the calculation of the particle drag force in cold spray should include both Re_r and M_r terms, and not just Re_r as often applied. For this reason the drag force coefficient is calculated using the model proposed by Henderson (Henderson 1976). This correlation can be found later in this thesis in Equations 5.19-5.22. The drag correlation by Henderson has been cross referenced to simulation results of supersonic flow around a sphere (Sun et al. 2004, Saito et al. 2007), showing a good level of concordance. These comparisons, as well as its widespread use in the application of cold spray modelling gives confidence to its use in this study.

During the experimental procedure for measuring the particle velocity–size relationship (see section 3.3) the particles were fed into the system at a mass flow rate of 30 g min^{-1}. At this rate the volume fraction of the powder within the gas phase is less than 10-12% and therefore it is reasonable to simulate each powder particle in a Lagrangian fashion, as a single, inert point in space with collisions between particles neglected. The momentum coupling parameter, Π_{mom}, as outlined by Equations 3.3–3.5, is used to assess the impact of the momentum of the dispersed powder on the gas phase, where: ρ_d is the particle density (kg.m^{-3}); d is the particle diameter (m); μ_c is the continuous phase viscosity (Pa.s); U is the continuous phase velocity (m.s^{-1}); L is the characteristic length (m) (i.e. the diameter of the nozzle at a specific location) and Z is the mass ratio of powder to gas.

$$\Pi_{mom} = \frac{Z}{St_{mom} + 1} \tag{3.3}$$

$$St_{mom} = \frac{\tau_v U}{L} \tag{3.4}$$

$$\tau_v = \frac{\rho_p d^2}{18\mu_c} \tag{3.5}$$

The parameter Π_{mom} has been calculated for both nitrogen and helium, and is less than 5% in all cases. Therefore the small reduction in momentum for the gas phase due to the presence of the powder is not included in this investigation. However, if the powder flow rate was increased and Π_{mom} exceeded 0.1 (≈60 g.min^{-1}) then one should couple the momentum of the two phases in a two-way manner. The vertical displacement induced by gravity on the discrete phase particles is deemed negligible due to the short time required by the particles to traverse the domain. Furthermore, by omitting the gravitational force the dispersion of the particles is solely influenced by the fluid dynamic behaviour of the process gas flowing through the designed nozzle. A thermophoretic force is included which arises due to temperature gradients within the flow. All of the discrete particles remain spherical and therefore the drag force model does not change accordingly. All discrete particles are identical at the inlet, with the same diameter, temperature and inlet velocity, which is perpendicular to the inlet surface, and parallel to the x-axis.

Property	**Description**
Material	Inert gas atomised copper (Cu)
Particle Density (kg m^{-3})	8978
Specific Heat Capacity (J kg^{-1} K^{-1})	381
Initial Particle Velocity (m s^{-1})	20
Initial Particle Temperature (K)	300

Table 3.2: Summary of simulated Cu powder material properties

The dispersion of the particles is accounted for by computing the trajectory of each particle based on the sum of the mean and turbulent velocity component of the gas phase in all three coordinate directions. For example, the velocity components in the x-direction are shown in Equation 3.6. Due to the assumption of isotropic turbulence the root mean square (RMS) of each fluctuating component (u', v', and w') of the gas phase is equal, and is deduced from the turbulent kinetic energy, k (m^{2}s^{-3}), of

the gas phase through Equation 3.7. If applying the Reynolds Stress Model for the accounting for the turbulent fluctuations, as is the case in Chapter 4, the fluctuating components are deduced from the conserved Reynolds Stress terms, as outlined in the appendix of this thesis. The values u', v', and w' are sampled assuming they obey a Gaussian (normal) probability distribution and are deduced by Equation 3.8. The term ζ is a random number selected from a Gaussian (normal) distribution.

$$u = \bar{u} + u' \tag{3.6}$$

$$\sqrt{\overline{u'^2}} = \sqrt{\overline{v'^2}} = \sqrt{\overline{v'^2}} = \sqrt{2k/3} \tag{3.7}$$

$$u' = \zeta\sqrt{\overline{u'^2}} \tag{3.8}$$

Several groups of particles enter the domain at different points at the particle inlet surface, and the number of particles per group represents the number of tries used by the probability based solver to compute the random effects of turbulence on the discrete particles. Therefore, by increasing the number of particles per group the dispersion accuracy can be increased.

The integral time scale, T_L, is estimated by Equation 3.9. The characteristic lifetime of an eddy, τ_e, is specified in Equation 3.10 and the eddy crossing time, t_{cross} , is given by Equation 3.11, where L_e is the eddy length scale, τ is the particle relaxation time and $|u-u_p|$ is the magnitude of the relative velocity between the particle and gas phase. Equation 3.12 gives the particle relaxation time where, μ is the gas viscosity, d_p is the particle diameter and ρ_p is the particle density.

$$T_L = 0.15\frac{k}{\varepsilon} \tag{3.9}$$

$$\tau_e = 2T_L \tag{3.10}$$

$$t_{cross} = -\tau ln\left(1 - \frac{L_e}{\tau|u - u_p|}\right) \tag{3.11}$$

$$\tau = \frac{\rho_p d_p^2}{18\mu} \tag{3.12}$$

A simulated particle is assumed to be in contact with the turbulent eddy for the shorter of the eddy lifetime (Equation 3.10) and eddy crossing time (Equation. 3.11). At the end of this time, a new turbulent velocity fluctuation (u') is generated based on a new random value of ζ and the total velocity (u) is updated. The total velocity is constant over the solution advancement time step Δt and the value of Δt is estimated so that the

trajectory of each discrete particle is carried out 5 times as it traverses a computational cell.

3.3 Experimental methodology

3.3.1 Cold spray equipment

Cold gas dynamic spraying (CGDS) was carried out at The University of Nottingham using an in-house designed system which is described in detail in a previous paper (Zhang et al. 2005). The experimental work carried out by Prof. McCartney and Dr. T Price (Price, 2008) is summarized in this section, as part of a collaboration project published in Tabbara et al. (2010).

A de Laval nozzle of dimensions identical to that given in Table 1 was employed. Nitrogen was used as the carrier gas for the powder which was fed axially into the pre-chamber of the nozzle as illustrated schematically in Figure 3.3. Normally, room temperature helium is used as the main processing gas to produce cold sprayed deposits. However, in the present study, involving a comparison with CFD calculations, experiments were performed with both room temperature nitrogen and room temperature helium as process gases at 29 bar stagnation pressure. When carrying out the particle sizing and velocity measurements as described in section 3.2 the de Laval nozzle was operated in a horizontal plane without the presence of a substrate.

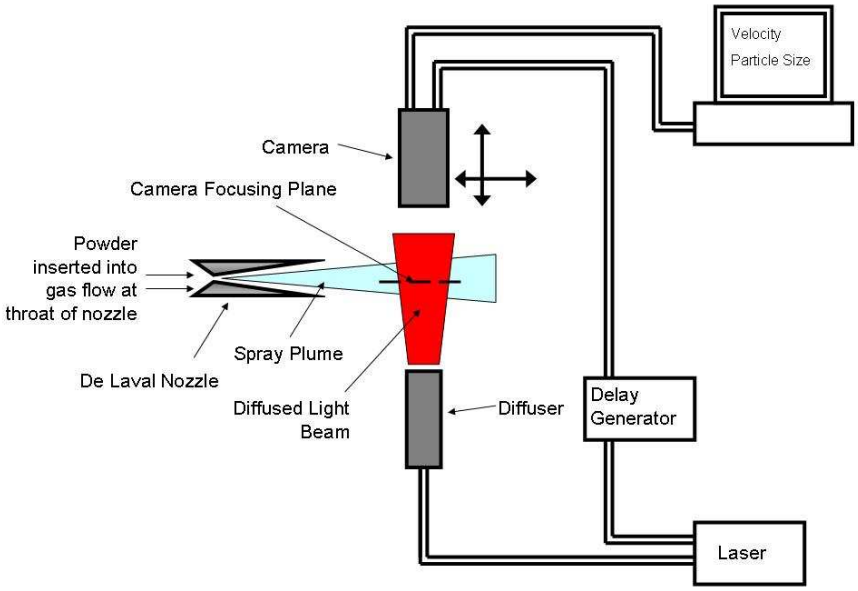

Figure 3.3: Schematic illustration of particle droplet image analysis system

A high pressure powder feeder (1264HP, Praxair, USA) was employed with a '120-hole' feed wheel and a wheel speed of 4 rpm which gave a powder feed rate for the copper

powder employed of approx 30 g·min^{-1}. The copper powder was inert gas atomized with a nominal size range 5-25 μm (Sandvik Osprey Ltd, Neath, UK) and had a near-spherical morphology.

3.3.2 Methodology for particle size and velocity measurements

Particle velocities and diameters were measured by a technique called Particle / Droplet Image Analysis or PDIA using the VisiSizer system produced by Oxford Lasers (Oxford Lasers, Didcot, UK). The principles of operation of the system, shown schematically in Figure 3.3, are as follows. An axial section of the spray plume is back lit (shadow graph method) for a short period (~ 6 ns) by a diffused, pulsed Nd:YAG laser light (532 nm) and two consecutive images are captured by a digital camera with an image separation time of typically 200 to 300 ns. Image processing software (VisisSizer v2.09, Oxford Lasers, Didcot, UK) employs a cross correlation algorithm to pair particles together. Using a known camera magnification and a known time delay between image frames individual particle velocities and corresponding particle diameters can be calculated. In the present study a field of view (FOV) of 1134 μm x 1134 μm was employed. Using this system it was possible to accurately measure particles as small as 3 μm in diameter. The image processing software was set to reject particles that failed to meet shape or focus criteria and so eliminate spurious data from overlapping particles or particles not within the measurement plane i.e. the plane of focus. The depth of field of the system was around 1 mm under the imaging conditions of operation in the present study so data obtained will approximate very closely to only those particles travelling along the spray plume axis.

For each experimental run data were recorded so that measurements of diameter and corresponding velocity could be obtained from 500 individual particles at a standoff distance of 20 mm from the nozzle exit and along the central axis of the spray plume. Further details of the experimental methodology are reported elsewhere (Price 2008).

3.4 Results and discussion

3.4.1 Measurements of particle size and velocity

In order to assess the accuracy of the size measurements performed by PDIA, in-situ, in the spray plume the resultant size distribution of the 500 measured particles was compared with that of the original copper powder feedstock. The size distribution of the original feedstock was determined by a standard laser diffractometry (LD) method. Both the PDIA and the LD data were found to closely fit a log-normal size distribution which is typically to be expected from a gas atomised powder. The PDIA

method gave a mean value for the diameter of 7.3 μm with a standard deviation for the log-normal distribution of 4.5 μm which compares very well with the LD measurements of 6.7 and 4.6 μm respectively for mean diameter and standard deviation of the log-normal distribution. Figure 4 (a) and Figure 4 (b) show scatter plots of particle velocity, V, and diameter, D, for 500 valid particles with N_2 and He process gas respectively at 29 bar stagnation pressure. Due to the small number of larger particles in the powder the data points are seen to become sparsely populated as the particle diameter increases. Clearly, there is a wide spread of particle velocities for particles of the same diameter and similar scatter is typically observed in diagnostic measurements of plasma spray or high velocity oxy-fuel spray plumes (Zhao 2004).

(a)

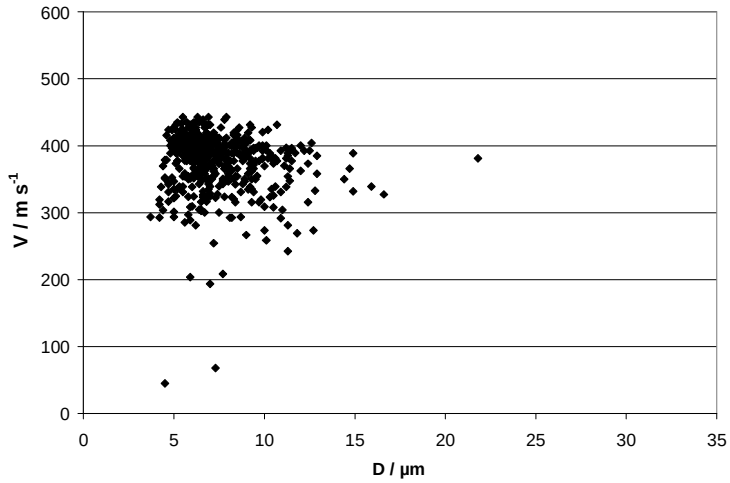

(b)

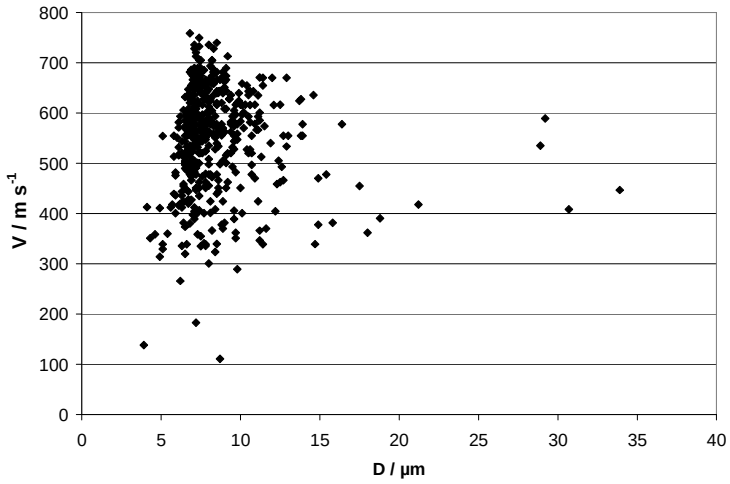

Figure 3.4: Scatter plot of particle velocity versus diameter using N_2 process gas at 29 bar, 293 K and a stand off distance of 20 mm (a) Scatter plot of particle velocity versus diameter using He process gas at 29 bar, 293 K and a stand off distance of 20 mm (b)

The raw particle data shown in Figure. 3.4 were ordered by increasing diameter and grouped into bins, each comprising of 20 particles. For each bin the mean particle size and velocity were computed and the results obtained are shown in Figure 3.5. In this plot, the error bars represent the standard error in the mean of the velocity data i.e.

$$\frac{\sigma}{\sqrt{N}}$$

where σ is the standard deviation of the velocity data in the bin and N is the number of data values in the bin (in all cases 20).

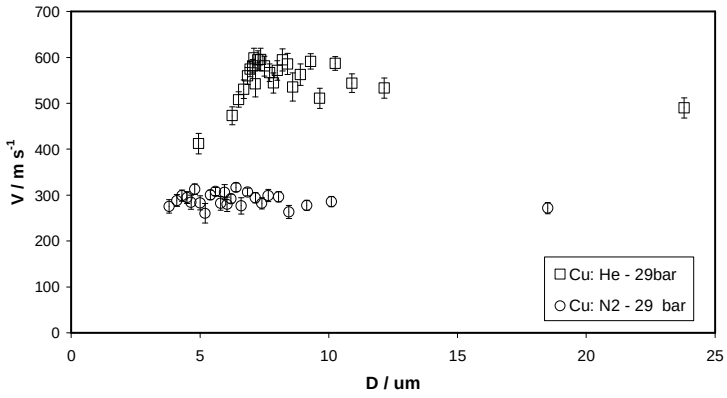

Figure 3.5: Plot of mean particle velocity versus particle diameter for particles grouped in bin sizes of 20 particles

It is clear that for all particle diameters He, as a process gas, produces particle velocities around twice that of nitrogen. Also the stagnation pressure of 29 bar has been shown previously to produce significantly higher particle velocities than 10, 20 or 25 bar (Price 2008). It is apparent that, particularly in the case of He as a process gas, particle velocity has decreased for bin sizes in the range 5 to 8 μm at a stand off distance of 20 mm which is somewhat unexpected. This could be due to either these small particles decelerating outside the de Laval nozzle or failing to be accelerated to the expected velocity inside the nozzle. To test this a limited number of measurements were performed at a 1 mm stand-off distance and a similar effect was observed. Thus it would seem possible that these smaller particles more readily diverge from an axial trajectory when injected into the de Laval nozzle than do larger particles of greater mass. They thus experience lower than optimum acceleration as discussed further in section 4.4.

3.4.2 Comparison between measurements and calculations

From the PDIA results the maximum particle velocity for a number of particle diameters are used in this investigation for comparison with the simulation results. An

SEM image of the Cu particles is exhibited in Figure 3.6, justifying the use of a spherical based drag model.

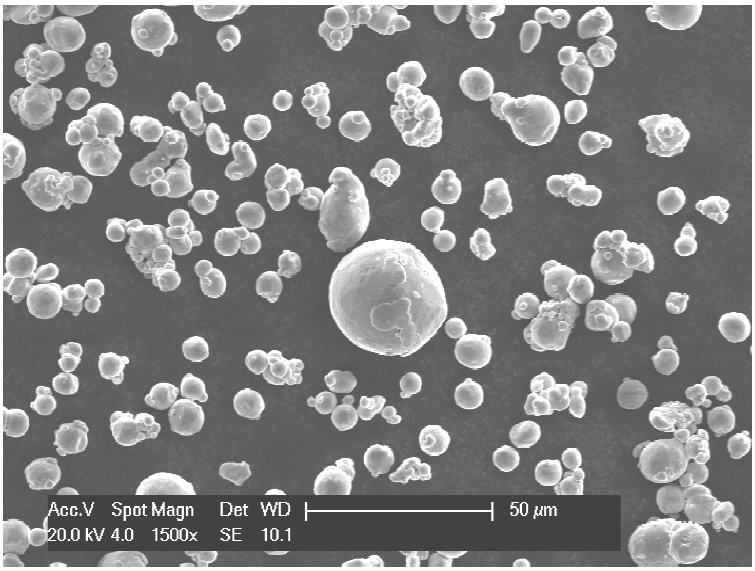

Figure 3.6: SEM image of copper powder used in the experimental section of cold gas spraying study (Price, 2008).

The baseline geometry for the simulations is outlined in Table 3.1 and the inlet boundary stagnation pressure is 29 bar. In order to replicate the maximum velocity a single particle is simulated, travelling along the centreline of the computational domain. The simulation is repeated for helium and nitrogen process gases, and for several different particle diameters. The simulated particle velocities at a stand-off distance of 20mm are compared with the experimental measurements at a stand-off distance of 20mm, as illustrated in Figure 3.7.

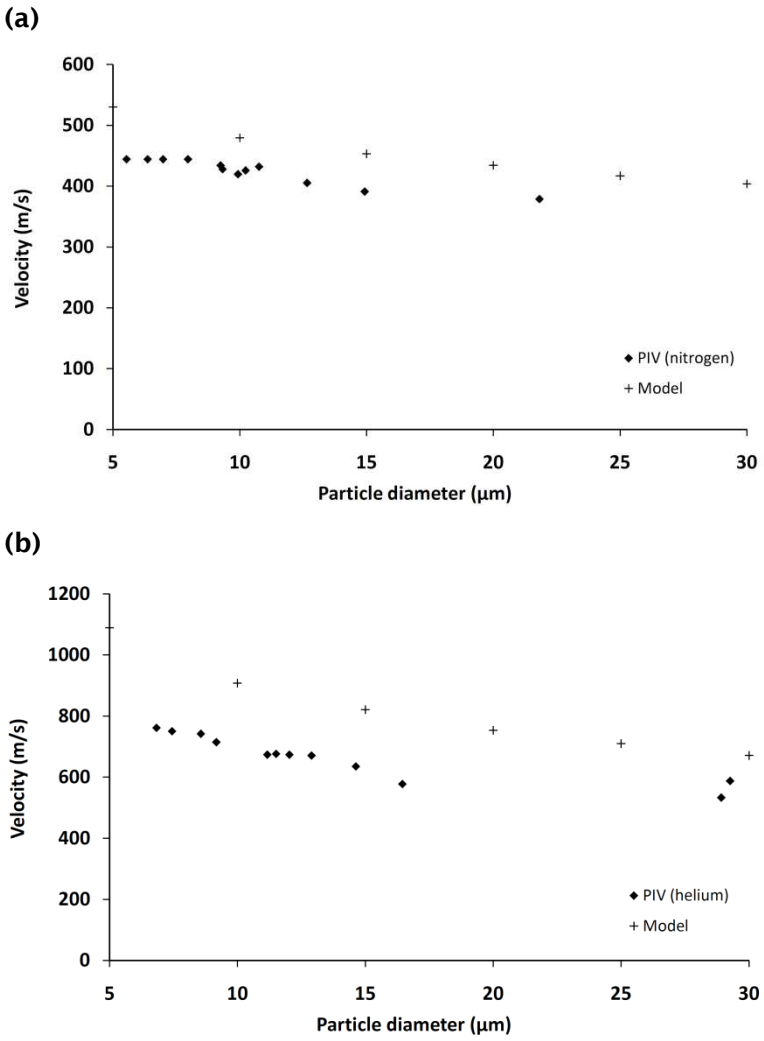

Figure 3.7: Comparison between the simulated and PIV measured particle velocities with nitrogen process gas at a SOD of 20 mm (a) Comparison between 2D simulated and PIV measured particle velocities with nitrogen and helium process gases at a SOD of 20 mm (b).

The comparisons show a similar trend, where the particles decrease in velocity with an increase in size. However, the simulations over predict the velocities by roughly 50 ms^{-1} and 200 ms^{-1} for nitrogen and helium process gases respectively. These discrepancies are believed to be caused by the assumption of a one dimensional trajectory along the centreline, where the process gas velocity is optimum. In reality each particle will travel at varying angles away from the centreline at the inlet and therefore will not be located along the centreline throughout their trajectory, where the process gas velocity and drag force is lower.

3.4.3 Nozzle cross section shape

The effect of the cross-sectional shape of the cold spray nozzle on the particle velocity and distribution at the exit is numerically tested by introducing roughly 1000 Cu particles (11 μm in diameter) from the region shown in Figure 3.1 into the

computational domain, carried by nitrogen at a stagnation pressure of 29 bar and 298 K. Each cross-sectional shape: circular, square and elliptical are investigated by designing the wall shape from the inlet to exit of the de Laval nozzle, each with the same varying cross-sectional area along the axis.

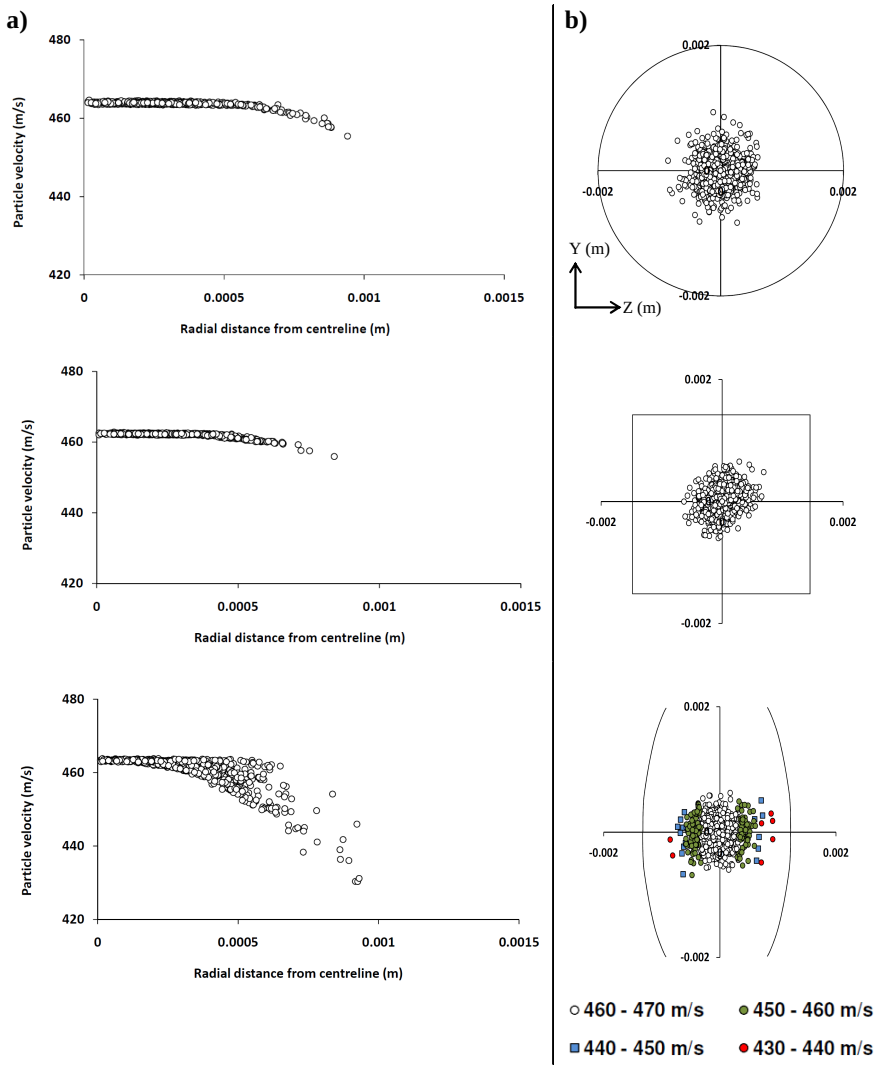

Figure 3.8: Relationship between particle velocity and radial distance (a) and exit distribution (b) at the exit of each simulated cold spray nozzle with different cross sectional shapes.

Figure 3.8(a) depicts the velocity of each particle against its radial distance from the centreline at the exit of each investigated nozzle. For the elliptical and square cross-sections, the radial location of each particle is plotted independently of its Y-Z coordinate. The Y-Z coordinates for each particle at the exit of each nozzle are exhibited in Figure 3.8(b). The results show that for all nozzle types the particles are distributed around the centreline axis. The circular cross-section and square cross section produce the least distributed set of particles in terms of both their radial

position from the centreline and their nozzle exit velocity. For these two nozzles 99% of the particles are within the 460-465 ms^{-1} range as summarized in Table 3.3.

Velocity limit (ms^{-1})	Percentage of particles with velocity < velocity limit		
	Circular	Square	Elliptical
430	0.00	0.00	0.00
435	0.00	0.00	0.35
440	0.00	0.00	0.82
445	0.00	0.00	1.41
450	0.00	0.00	2.71
455	0.00	0.00	7.53
460	1.00	1.11	21.06
465	100.00	100.00	100.00

Table 3.3: Cumulative percentage of particles with increasing exit velocity for the three tested cross sections

The results in Table 3.3 also show the wider range of particle velocity created by the elliptic cross section. The results show that roughly 20% fall below 460 ms^{-1}, and of these, a further 3% exit at velocities less than 450ms^{-1}. The correlation between the particle velocity and Y-Z location at the nozzle exit of the elliptic nozzle is depicted in Figure 3.8(b). A clear decrease in velocity and increased dispersion occurs with increasing distance along the Z-axis from the centre. A steeper velocity gradient between the wall and the centre of the flow is present in the Z-direction compared to the Y-direction due to the shorter distance, creating greater shear stresses within the flow. As a result an increase in turbulent kinetic energy and resulting velocity fluctuations arise leading to a noticeable dispersion of the particles in the Z-direction. The particles which are displaced towards the wall experience a decrease in drag force due to the decreasing flow velocity towards the wall resulting in a lower exit velocity.

3.4.4 Particle size and process gas

The effect of the particle size on the particle velocity and displacement distribution at the exit of the nozzle is tested by comparing 5μm and 30μm particles. 1000 particles are introduced into the conical nozzle computational domain, and are carried by nitrogen gas at a stagnation pressure of 29 bar and 298K.

Figure 3.9 shows the simulated variation in the displacement and velocity distributions at the exit of the de Laval nozzle, for a 5 μm and a 30 μm powder source. The 5 μm particles are clearly more dispersed by the expanding gas phase and turbulent fluctuations. On the other hand 30μm particles are less easily affected, which results in a more confined dispersion pattern with significantly slower velocities at the exit of the nozzle. While the variation in velocity for the smaller particles is larger, the velocity for all 5 μm particles remains superior throughout compared to the larger 30 μm particles.

(a)

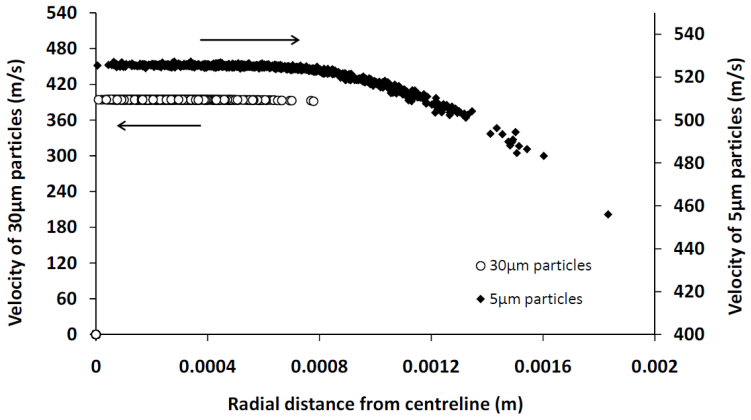

(b)

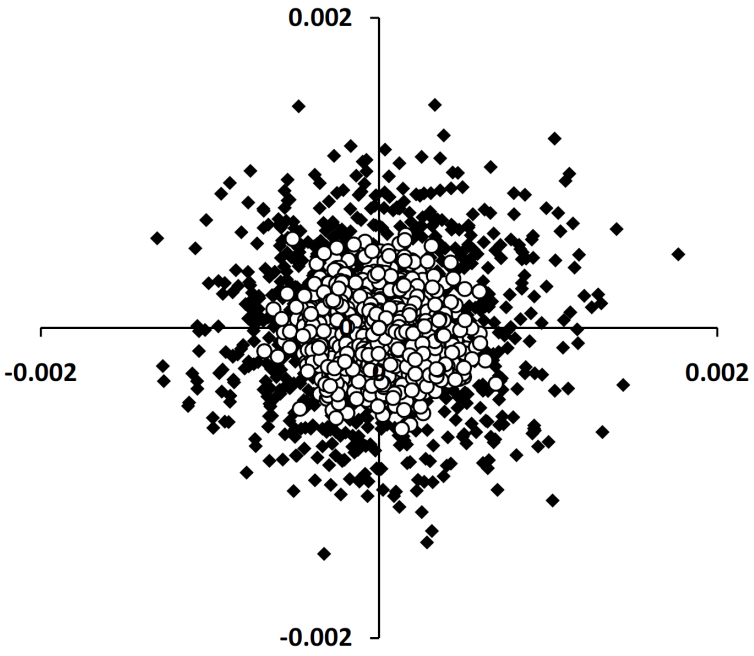

Figure 3.9: Comparison of particle velocity variations (a) and particle distributions (b) at the exit of the baseline cold spray nozzle for 5 μm and 30 μm Cu particles

Nitrogen and helium process gases are compared at a stagnation pressure of 29 bar and 298K. 1000 11μm Cu particles are introduced into the computational domain. Figure 10 quantifies the extent by which the helium velocity greatly exceeds the nitrogen gas velocity along the centreline.

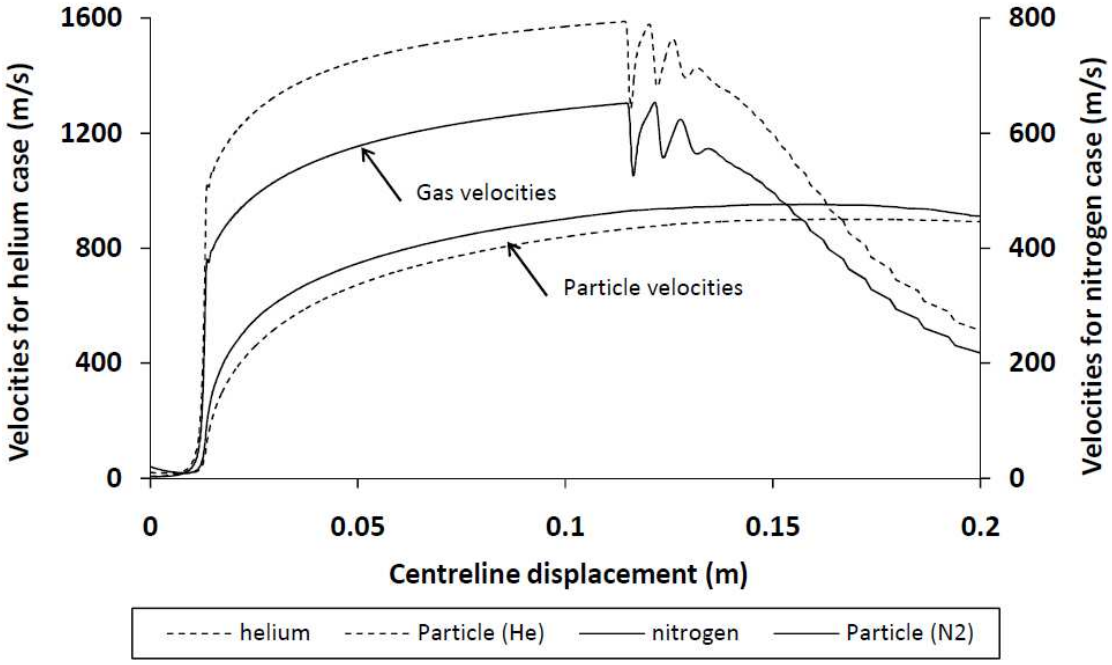

Figure 3.10: Velocities of process gas and 11μm Cu particle velocities through the baseline geometry for helium and nitrogen process gases. Simulation in 3D.

(a)

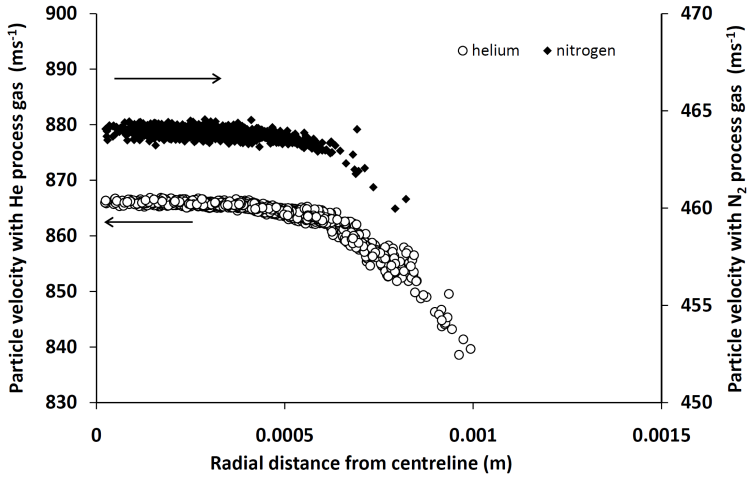

(b)

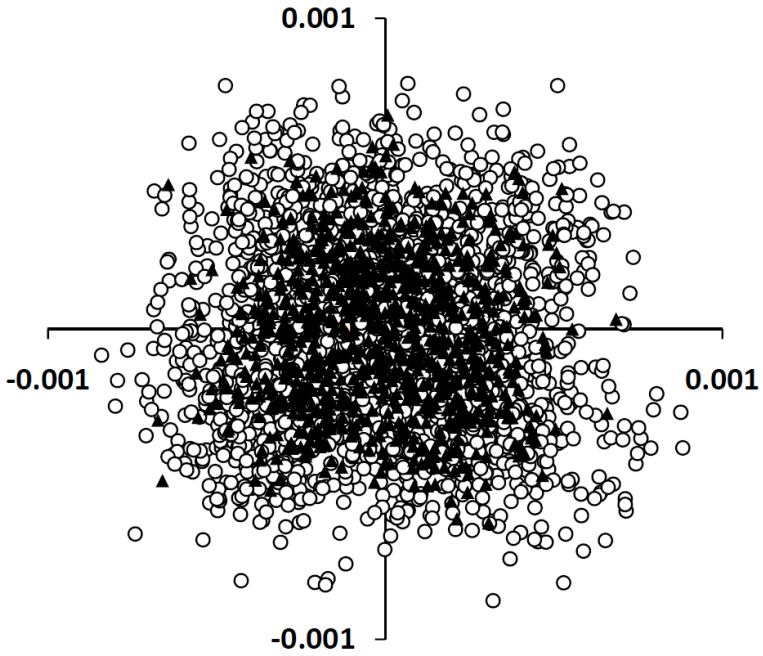

Figure 3.11: Comparison of particle velocity variations (a) and particle distributions (b) at the exit of the baseline nozzle for helium and nitrogen process gases.

Helium has a higher adiabatic index and higher specific gas constant than nitrogen, which results in a higher speed of sound. This effectively enables helium gas and the entrained particles to be accelerated to far higher velocities during the cold spray process. The results in Figure 3.10 and Figure 3.11 show that helium gas is far more effective at accelerating the powder particle than nitrogen. Helium is also shown to disperse the powder particles in Figure 3.11 more than nitrogen. This is due to the higher levels of turbulence found in the helium flows which are induced by the higher velocity gradients through the fluid. The turbulent velocity fluctuations are estimated

using Equation 3.7 and quantified by Figure 3.12 at the exit of the conical nozzle for nitrogen and helium process gases.

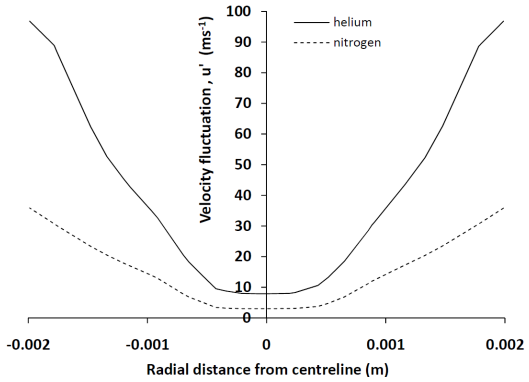

Figure 3.12: Comparison of turbulent velocity fluctuations at the exit of the conical nozzle for nitrogen and helium process gases.

3.4.5 Contoured nozzle

The straight edge of the original baseline nozzle is contoured by applying the method of characteristics (MOC) in order to reduce the length of the expansion region of the nozzle, and improve its manufacturability. It is known from internal communications that the nozzle is difficult to produce by boring with a smooth and accurate internal expansion region which usually has a long and thin structure (Figure 3.1).

A MatLab code (Nozzle Design Program by means of MOC, Dr Zhiwei Hu, University of Southampton) is used in order to create an axisymmetric minimum length nozzle. A contour correction is also included which makes the model applicable to viscous flow. The nozzle wall is corrected by a distance equal to the displacement thickness of the wall boundary layer. The semi-empirical method for the calculation of compressible turbulent boundary layers published by Tucker (Tucker et al. 1950) is applied and converted to an axisymmetric domain using the methods presented in (Sivells 1950). This contour is designed so that the stagnant nitrogen gas at a pressure of 30 bar and temperature of 300 K is expanded to a steady-state supersonic flow which is free of shocks inside the expanding section. Firstly, this technique is applied to create a nozzle with the same geometric properties as the baseline model, with an outlet diameter of 4 mm. The contour shape is exhibited in Figure 3.13. In order to create the same expanding-section length as the baseline model a barrel is attached to the end of the minimum length nozzle. This length is required to give the powder particles a sufficient amount of acceleration time inside the jet.

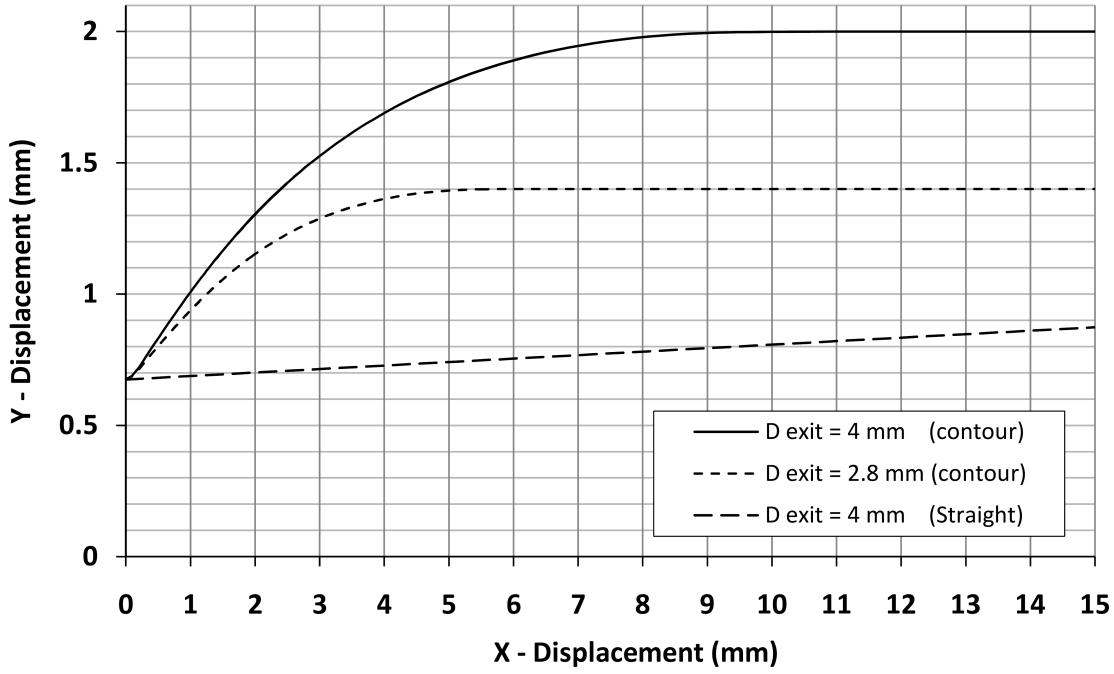

Figure 3.13: Close up of the compared expansion sections illustrating the different expanding minimum length contour designs over 15 mm of the 100 mm total throat to exit length.

Figure 3.14 summarizes the simulated gas flow and resulting single 11μm Cu particle velocity along the centreline for the baseline model and contoured designs. For the original conical nozzle, the compressed nitrogen is forced through the de Laval nozzle, at the throat the flow is choked at mach one and the nitrogen gas velocity is raised slowly and smoothly through the expansion section, with the exception of some small oscillation in the flow close the critical section of the nozzle. The gas velocity reaches a maximum velocity at the exit of the nozzle. At this point the gas pressure is lower than the atmospheric pressure resulting in an over-expanded flow regime at the exit, characterised by a sharp decrease in velocity at the nozzle exit. The lower gas pressure of the exhausting nitrogen in comparison to the atmospheric pressure leads to the exhaust gas being compressed inwards resulting in an increase in exhaust gas pressure. However, the flow is naturally over compressed to a pressure greater than the atmospheric pressure, which then causes the gas to expand. Mixing of the exhaust gas with the atmosphere occurs in the stand of region and the process of over compression and over expansion continues until the exhaust gas pressure reaches the same value as the atmospheric pressure. The oscillations are clearly visible in the modelled results, shown in Figure 3.14.

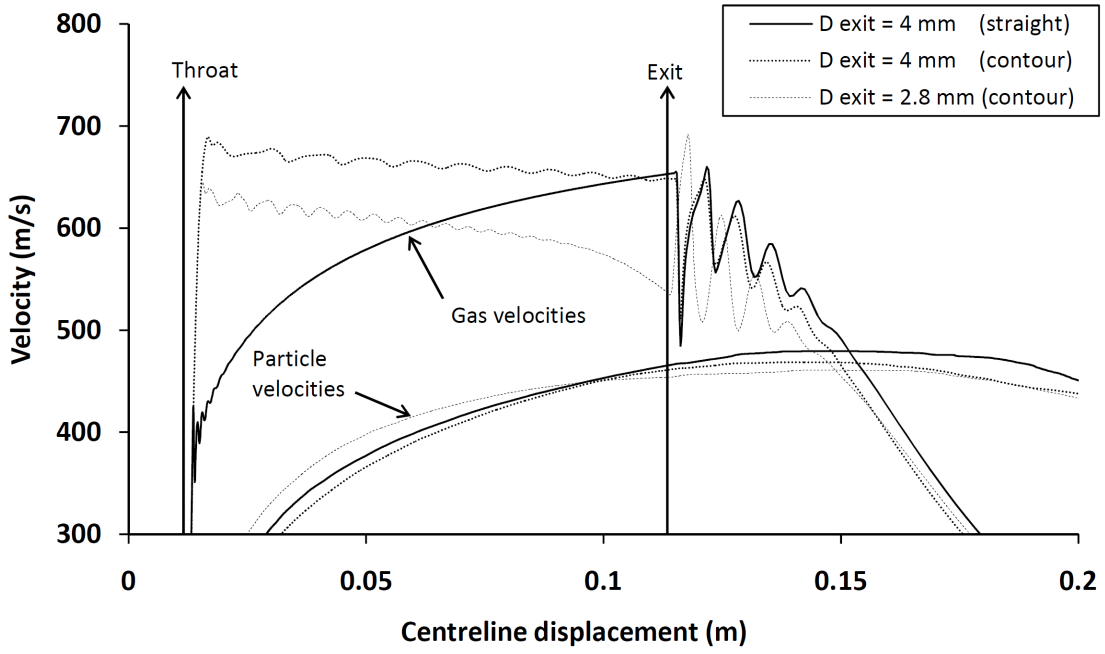

Figure 3.14: Gas and particle velocities through the baseline and contoured nozzle geometries. Simulation in 2D.

Furthermore, the over-expanded flow regime at the nozzle exit is exhibited in Figure 3.15 in terms of gas velocity and density variation. Over-expanded jet phenomena are commonly found in thermal spraying. A good example of experimental images of such regimes can be found in (Jodoin et al. 2002). Further details on this flow regime can be found in (Anderson, 2007).

Owing to the same throat and exit diameter the exit velocity and exterior jet region of the contour design and the conical baseline model are very similar, with an over-expanded flow region. However, for the contoured nozzle, the flow is accelerated rapidly when exiting the throat and the velocity profile for this design remains higher than the conical design throughout the expanding and barrel section of the de Laval nozzle. While the designed contour section creates a smooth, shock free flow through the expanding section of the nozzle, oscillations occur along the barrel due to strong reflections at the internal surface. This rapid increase in velocity of the process gas in the minimum length nozzle leads to a decrease in density and static pressure. For the contour nozzle the decrease in density during the rapid acceleration and expansion of the process gas results in lower particle acceleration through the system compared to the conical design, leading to a slightly lower particle velocity at the exit and within the stand-off region, as exhibited in Figure 3.14. This difference in particle velocity may be viewed as negligible, and the use of a minimum length nozzle and barrel extension may be seen as equivalent to a long diverging section. As a result, if the manufacture

of the long diverging nozzle proves difficult then one may produce a minimum length nozzle with an attached constant diameter barrel of appropriate length.

The exit diameter of the minimum length nozzle was reduced incrementally with the same barrel attached. The results showed that for a contoured design with an exit diameter of 2.8 mm the process gas is expanded less, leading to a lower velocity. However the density remains higher creating a faster particle velocity profile along the first half of the barrel section. In this case the gas velocity begins to decrease along the barrel due to the over expansion, indicating that the barrel length is crucial in the design of the minimum length nozzle. As a result the particle acceleration depletes, resulting in a lower exit velocity compared to the baseline conical design. By further decreasing the diameter of the nozzle exit the flow is choked inside the barrel, leading to a degraded and inefficient flow regime.

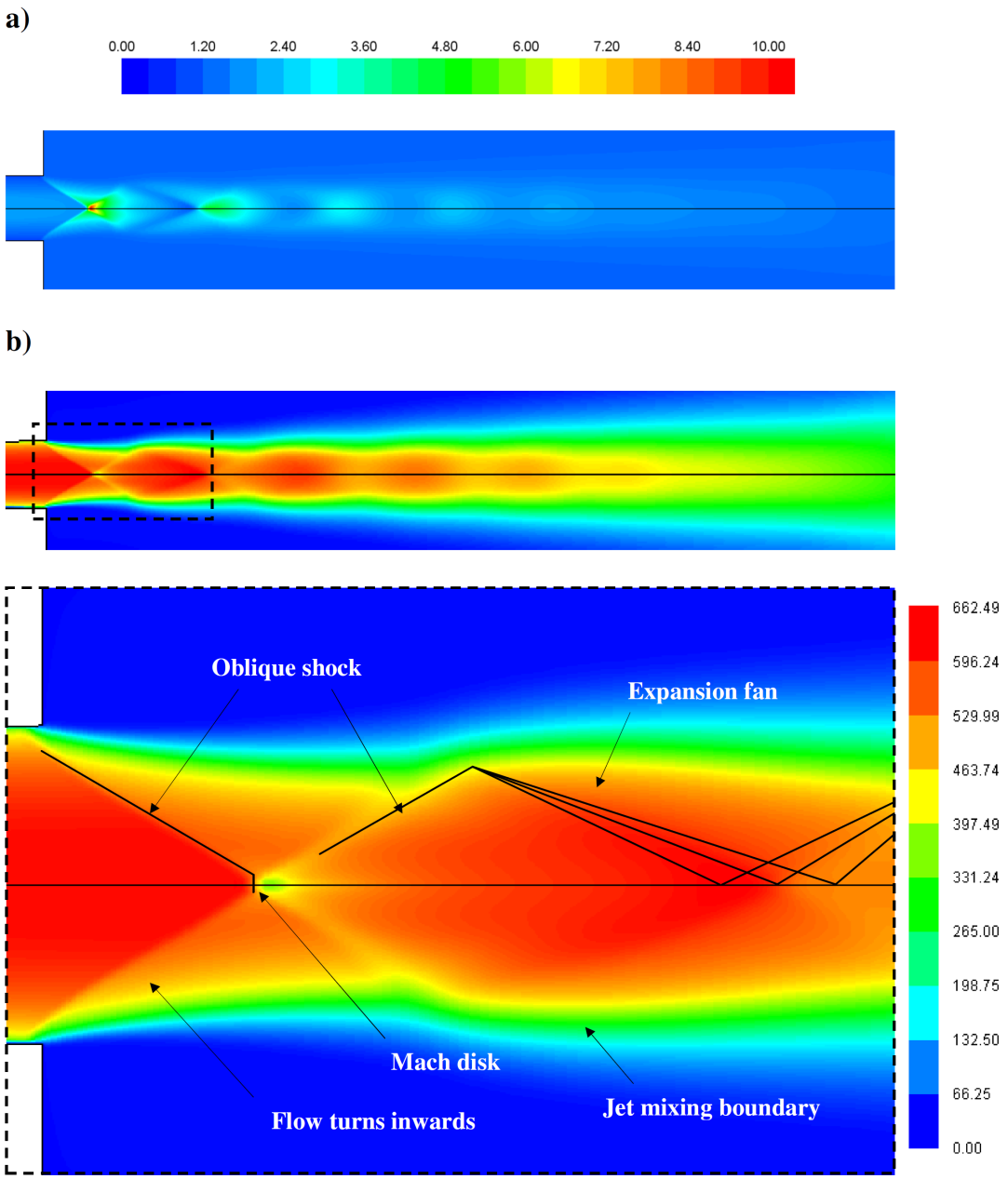

Figure 3.15: Density contours (kg m^{-3}) (a) and Velocity contours (ms^{-1}) (b) at the exit of the nozzle showing the over-expanded flow regime.

3.5 Conclusion

Compressible, supersonic nitrogen and helium gas flow is simulated in 2D and 3D through a cold spray convergent-divergent nozzle. Copper particles of various diameters are coupled in a Lagrangian reference frame, and their resulting dynamic response is investigated with the inclusion of turbulent effects. The results drawn from this investigation are summarized as follows.

The effect of the cross-sectional shape of the cold spray nozzle on the particle velocity and distribution is tested for nitrogen at stagnation pressure of 2.9 MPa and copper particles of 11 um diameter. The results show that relative to the elliptical cross section, the circular and square cross-sections have the least dispersed powder distribution as well as the greatest average particle velocities. Therefore a circular or square cross section should be selected in order to achieve the very highest particle velocities. However the velocity reduction within the elliptical flow is relatively small, at a maximum of roughly 20ms^{-1}. A more dispersed particle flow is advantageous for the buildup of an evenly distributed coating. In these cases an elliptical shape is most beneficial.

Furthermore, the effect of the particle size on the particle velocity and displacement distribution at the exit of the nozzle is tested. The 5μm particles are more dispersed and have higher velocities at the exit compared to the 30μm particles. Helium is shown to disperse the powder particles more than nitrogen due to the higher levels of turbulence created by the helium gas flow.

A contoured shape is created for the diverging section of the nozzle with a minimum length using the MOC. A barrel of constant diameter is then added to the exit. The simulated gas and particle velocities are then compared to the original conical design, with the same throat and exit diameter and throat to exit length. The gas flow in this contoured nozzle is accelerated rapidly and the velocity profile remains higher than the conical design throughout the expanding section of the de Laval nozzle. However, due to a decrease in gas density a slightly lower particle velocity is observed for the minimum length MOC nozzle design at the exit and within the stand off region. However, this difference is negligible and therefore one may alternatively produce a minimum length nozzle with an attached barrel of appropriate length. This in turn may improve the manufacturability of the cold spray nozzle by not having to bore a smooth and accurate internal expansion region which usually has a long and thin structure.

Measurements of particle size and corresponding velocity have been recorded and the results show a similar trend to the simulation results. The particle velocities are over predicted by the simulation by roughly 50 ms^{-1} for a nitrogen process gas, and by roughly 200 ms^{-1} for a helium process gas. The over predicted velocity is believed to be down to an idealistic comparison with a particle travelling along the centre line. A recent computational study including the detailed injection stream characteristics has shown that particles do in fact follow a very disorderly flow pattern through the

converging section due to collisions with the wall and dispersion due to gas turbulence (Lupoi & O'Neil, 2011).

4 Warm spraying of titanium particles

A warm spray system has been computationally investigated by introducing a centrally located mixing chamber into a HVOF thermal spray gun. The effects of injecting a cooling gas on the gas and particle dynamics are examined. The titanium powder is tracked using the Lagrangian approach including particle heating, melting and solidification. The results present an insight in to the complex interrelations between the gas and particle phases, and highlight the advantage of warm spray, especially for the deposition of oxygen sensitive materials such as titanium.

4.1 Chapter introduction

The high strength to weight ratio, corrosion resistance, biocompatibility and osseointegratability within the human body, makes titanium extremely useful when applied in aerospace engineering industries, biomedical implants, structural offshore, and other seawater-related application. This range of properties makes titanium a valuable material within engineering and the surface coating industry (Pawlowski 2008b, Brunette et al. 2001, Boyer 1996, Pohler 2000, Donachie 2000).

However, titanium exhibits a strong affinity for oxygen and so, when manufacturing a titanium coating using powder based thermal spray methods, control of the particle temperature and its surrounding environment is crucial. Several experiments have tested and revealed the sensitivity of titanium powder to the cooling gas flow rate in WS (Kawakita et al. 2006, Kim et al. 2009a, Kim et al. 2009b). With low levels of cooling the coating consistency is similar to standard HVOF, where the particles are overheated, melted and oxidized, forming an abundance of TiO and Ti_2O_3 (Kawakita et al. 2006). The melting of titanium particles can also result in splashing at the substrate surface, creating poor contact. However, with high cooling flow rates the particles do not adhere well, and a significant level of porosity is created within the coating (Kawakita et al. 2006). With the correct level of cooling gas, the particles are shown to soften but not melt. Consequently the levels of oxidation diminish, and observed particles adhere well through the creation of metallic and diffusion bonds (Kawakita et al. 2006).

An alteration to the HVOF process has recently gained much interest, and has been termed warm spray (WS). This recent development is the latest within this family of supersonic thermal spray devices. By combining a room temperature inert gas with the standard HVOF jet, the temperature of the propellant gas can be controlled in

order to deposit powder materials in a thermally softened state at high impact velocity (Kuroda et al., 2011). Further details can be found in the introduction of this thesis.

This present study goes beyond the previous study of combustion and gas-phase study described in Chapter 2 (Tabbara & Gu, 2009) by incorporating a central cooling chamber concept developed by Kawakita et al. (Kawakita et al. 2006). Preliminary results of a one-dimensional mathematical model of the gas flow of a similar WS system have been reported in (H. Katanoda et al. 2008) including titanium particle trajectories and temperatures along the one dimensional path. However, more accurate computational models are required for more detailed information about the mixing of combustion and cooling gases as well as particle dynamics and interaction with the gas flow. This CFD work is carried out to meet this objective by combining the detailed fluid dynamic and discrete phase modelling, accounting for temperature distribution and phase change within particles.

4.2 Model description

4.2.1 Model overview

The simulations are run in the commercial finite-volume CFD package Fluent 6.3 (Fluent. Inc, Lebanon, NH, USA). A schematic diagram of the modified WS system, based on a modified JP5000 gun design, is given in Figure 4.1, highlighting the fuel-oxygen inlet (a), the combustion chamber (b), the mixing chamber (c), the nitrogen inlets (d), the convergent-diverging nozzle (e) and the barrel (f). The position of the particle inlet is also provided (g).

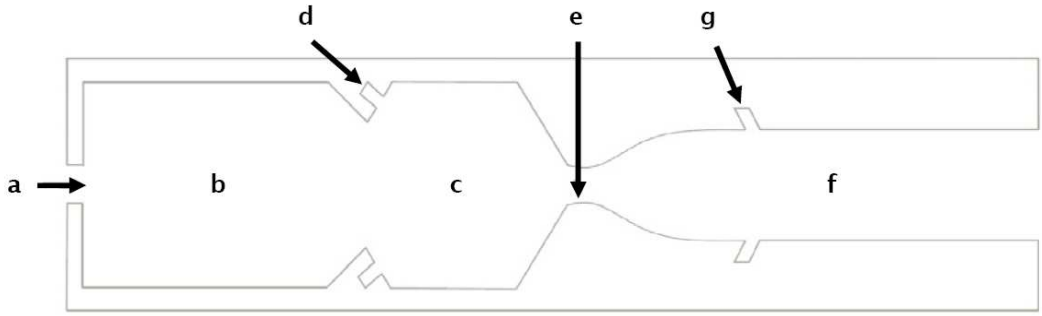

Figure 4.1: A schematic diagram of a warm spray system showing the fuel-oxygen inlet (a), the combustion chamber (b), the mixing chamber (c), the nitrogen inlets (d), the converging diverging nozzle (e) and the barrel (f).

An overview of fuel droplet and flame shape within the original JP-5000 design can be found in Chapter 2 (Tabbara & Gu 2009) and details of the gas phase dynamics and liquid fuel kerosene-oxygen combustion reaction is outlined later in Chapter 5

(Tabbara & Gu 2012). The computed temperature profile through the modified version of the thermal spray system is given in Figure 4.2 for the different cooling scenarios.

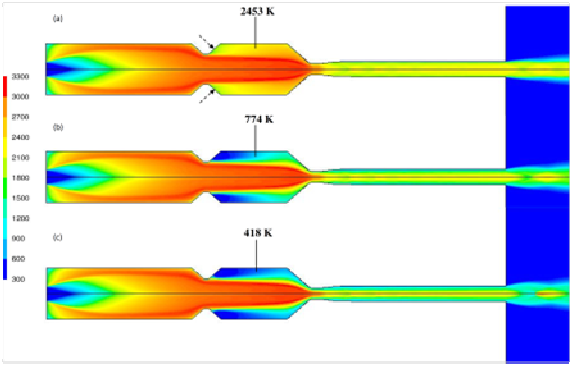

Figure 4.2: Temperature contours through the modified JP-5000 with (a) 0.00 kg/s, (b) 0.01 kg/s and (c) 0.02 kg/s of nitrogen gas. The position of the nitrogen inlet is shown by the dashed arrows in (a).

The geometric parameters and the boundary conditions for the simulation in this investigation are summarized in Table 4.1. The fuel and oxygen inlet conditions are based on values provided by industry.

Geometric parameter	
Barrel length	111.1 mm
Barrel entrance diameter	11.0 mm
Barrel exit diameter	11.1 mm
Combustion chamber length	92.5 mm
Combustion chamber diameter	37.8 mm
Mixing chamber length	43.0 mm
Mixing chamber diameter	37.8 mm
Nozzle throat diameter	7.9 mm
Working conditions	
Fuel	Flow rate: 0.0057 kg/s, Temperature: 300 K
Oxygen	Flow rate: 0.022 kg/s, Temperature: 300 K
Atmosphere	Pressure: 101325 Pa, Temperature: 300 K
Internal wall boundary	Temperature: 350 K, Non-slip

Table 4.1: Summary of geometric parameters and working conditions of the simulated warm spray system

The modelling domain is represented by a 2D axisymmetric model. The mesh within the combustion chamber consists of 160 axial nodes and 50 radial nodes. The mixing chamber and converging-diverging region consists of 235 axial nodes combined. The external region covers a practical stand off distance of 300mm. The

grid consists of 61,000 cells in total, with the convergent-divergent nozzle and the free jet region being successively refined in a grid sensitivity study in order to capture steep variations in flow properties due to the effects of compressibility. These refined grid area refinements are depicted previously in Figure 2.2.

The near wall region of a fluid flow can be split into three sections: the viscous sub layer adjacent to the wall which generally represents 1% of the total boundary layer thickness; the buffer region; and the logarithmic law region. The standard wall function developed by Launder & Spalding (1974) is adopted, where the wall mean velocity relationship is given by Equation 4.1, and the dimensionless distance from the wall is given by Equation 4.2.

$$U = \frac{1}{\kappa} ln(Ey^*) \tag{4.1}$$

$$y^* \equiv \frac{\rho C_\mu^{0.25} \lambda^{0.5} y_p}{\mu} \tag{4.2}$$

In order for the boundary cell centroid to lie within the log law region, and therefore for an accurate prediction of the cell velocity, the y* value should lie between 30 and 300. Hence, to accurately capture the flow development within the convergent-divergent nozzle and barrel the mesh y* values within these regions were tuned by adapting the mesh density accordingly.

4.2.2 Turbulence model

In the previous investigation of the JP-5000 as presented in Chapter 2 (Tabbara & Gu 2009), the realizable k-ε model was applied in order to capture the turbulent effects within the steady state flow. However, due to the added complexity of a second mixing gas impinging on the main flow a more elaborate turbulence model is adopted in this instance. The advanced Reynolds-stress turbulence model (RSM) is applied (Gibson & Launder 1978, Launder 1989, Launder et al. 1975), which solves the transport equations for each Reynolds-stress term ($\overline{u_2' u_1'}$) and so avoids the isotropic eddy-viscosity hypothesis used in the k-ε model. As a result the model can more accurately capture the mixing of the cooling nitrogen gas within the combustion mixture as well as help to improve the realism of the external flow regime where the flow strain-rates are extremely high and shock wave patterns and shear-layer interactions are complex. In turn, the particle heating and cooling which is expected to be largely affected by this external flow pattern can be better predicted. Details of RSM can be found in the appendix of this thesis.

4.2.3 Particle model

The discrete particles are tracked in a Lagrangian reference frame and their interaction with the gas phase is one-way coupled. Hence, the particles do not influence the computation of the gas phase characteristics. Each particle is injected into the gas stream at a single point at an angle of 45° in the same direction as the flow. Their initial velocity magnitude is 40 ms^{-1} which compared to velocities calculated in (Katanoda et al. 2004) for particles in the range of 10 to 50 μm injected in to the JP-5000, is deemed a reasonable and realistic value. An overview of the particle dispersion modelling approach can be found in Chapter 3 (Tabbara et al. 2010).

The heat transfer model appearing in (Ahmed et al. 2001, Zeoli et al. 2008) has been applied as a user defined function (UDF) in this paper to predict the transient temperature profile and phase change through spherical titanium particles of various diameters. The relavent thermal physical properties of titanium are listed in Table 4.2.

Property	**Value**
Melting point, T_m (K)	1943
Heat of fusion, H_f (MJ/kg)	0.419
Density, ρ (kg/m^3)	4540
Thermal conductivity, k(T) (W/mK)	0-28.0
Specific heat capacity, C_p(T) (J/kgK)	521 -752

Table 4.2: Titanium particle material properties used for the simulation within warm spray.

The transient temperature distribution through a spherical particle as a function of the particle radius can be calculated using Equation 4.3. The rate of change of solid fraction determines the latent heat of fusion in the last term of this equation, which is computed by rearranging Equation 4.12 to form Equation 4.4 and Equation 4.5.

$$\rho_p C_p \frac{\partial T}{\partial t} = k_p \left(\frac{\partial^2 T}{\partial r^2} + \frac{2}{r} \frac{\partial T}{\partial r} \right) + H_f \rho_p \frac{\partial f}{\partial t} \tag{4.3}$$

$$\frac{\partial T}{\partial t} = \frac{\alpha}{\psi(T)} \left(\frac{\partial^2 T}{\partial r^2} + \frac{2}{r} \frac{\partial T}{\partial r} \right) \tag{4.4}$$

$$\psi(T) = \begin{cases} if\ T_s \leq T \leq T_L \ \ 1 + \dfrac{H_{sf}}{C_p(T_l - T_s)} \\ else\ 1 \end{cases} \tag{4.5}$$

The boundary conditions for the temperature profile at the outside surface where r = R and at the centre, where r = 0 are specified below in Equation 4.6 and Equation 4.7 respectively.

$$\left.\frac{\partial T}{\partial r}\right|_{r=0} = 0 \tag{4.6}$$

$$4\pi r_p^2 k \left.\frac{\partial T}{\partial r}\right|_{r=r_p} = 4\pi r_p^2 h\left(T_g - T_R\right) \tag{4.7}$$

The convective heat transfer coefficient, between the surface of the particle and the surrounding gas is derived from the Ranz & Marshall correlation (1952a, 1952b) as presented in Equation 4.8.

$$Nu = \left(2 + 0.6 Re_p^{\frac{1}{2}} Pr^{\frac{1}{3}}\right) \tag{4.8}$$

The partial differential equation in Equation 4.4 is discretized using the Crank-Nicholson method as outlined in Chapter 7 (A radiation term in Chapter 7 is included in order to estimate the temperature distribution through a ceramic particle in a plasma flow). The maximum computed Biot number for all particles is 0.2. Because this value is not a complete order of magnitude smaller than 1 (i.e. 0.1) it is necessary to model the temperature gradient through the particle, rather than assume that the rate of heat conduction through the particle far exceeds the rate of heat convection into the particle at its surface. The temperature at 20 equally spaced intervals along every particle radius is calculated. Even in the case of the maximum Biot number 20 discretization points is considered more than satisfactory. At each time step the temperature distribution through the particle is solved using the Gauss Seidel iterative method.

4.3 Modelling results

4.3.1 Gas flow dynamics

The liquid fuel droplets are injected into the combustion chamber with pure oxygen where they heat, evaporate and then exothermically combust, creating a highly pressurized gaseous mixture at roughly 3200 K. The fully mixed exhaust gas consisting of O, O_2, H, H_2, OH, H_2O, CO_2, and CO exits the combustion chamber and then passes the cooling compartment. At the convergent-divergent nozzle the gas is rapidly accelerated. At the throat of the convergent-divergent nozzle the flow is choked at Mach one. Two small discontinuities follow as the gas expands and accelerates through the divergent section, marked by slight increases in velocity along the centreline, as depicted in section e of Figures 4.3 and 4.4.

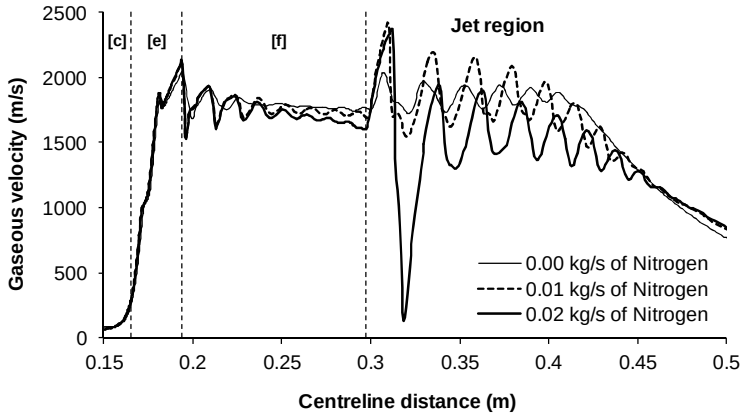

Figure 4.3: Comparison of gas flow velocity along the centreline of the modified JP-5000 with increasing nitrogen cooling flow rates.

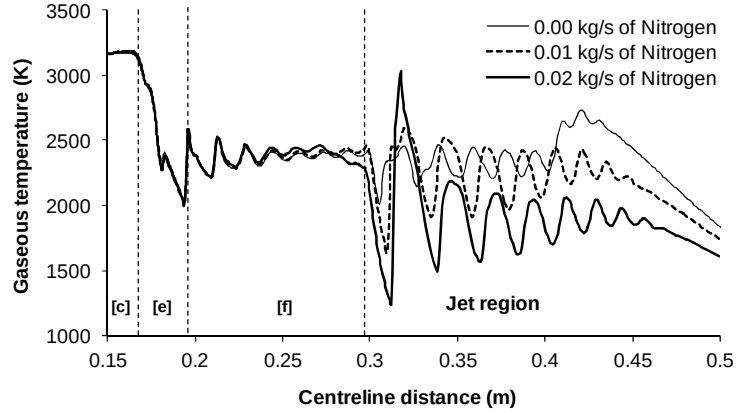

Figure 4.4: Comparison of gas flow temperature along the centreline of the modified JP-5000 with increasing nitrogen cooling flow rates.

Several shocks occur at the exit of the convergent-divergent nozzle and through the barrel due to the expansion of the supersonic gas and strong reflections at the solid internal surface of the barrel, which are characterized by fluctuations in velocity and temperature along the centreline, as exhibited in Figures 4.3 and 4.4. An under-expanded flow regime at the exit of the barrel is present, enforced by a slightly subcritical atmospheric back pressure. The fluctuations in flow properties at the exit of the barrel are created by the flow periodically over expanding and then re-converging above and below atmospheric pressure. These adjustments continually overshoot due to the boundary communicating with the jet by sound waves, which naturally travel slower than the bulk supersonic flow.

At the exit the difference in pressure and back pressure determines the type and intensity of the flow regime. Greater velocity oscillations at the exit of the barrel imply a greater degree of mixing and axial momentum reduction for the gaseous flow. By

increasing the nitrogen flow rate and hence also the upstream pressure, the flow pressure at the exit of the barrel is also increased. As a result the magnitude of the fluctuations in velocity and temperature which are brought about by the under-expanded flow regime are increased.

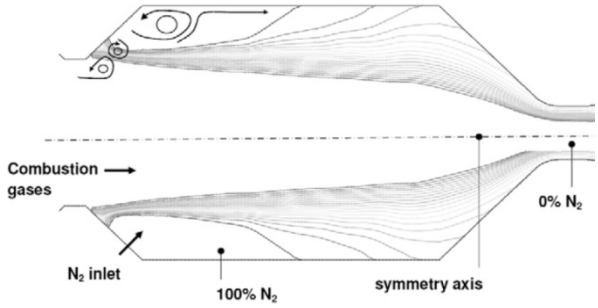

Figure 4.5: Mole fraction variation of N2 within the mixing chamber with a nitrogen flow rate of 0.02 kg/s. The recirculation zones highlighted.

Figure 4.5 depicts the mole fraction variation of nitrogen through the mixing chamber. Initially the nitrogen mixing is limited, even with the injection angled towards the passing combustion gas mixture. Figure 4.6a shows that the nitrogen cooling gas travels along the boundary wall and continues to mix along the barrel, essentially producing a nitrogen-rich boundary layer, where the gas temperature and axial velocity is lowered. Figure 4.6a indicates that for the current design and nitrogen injection mass flow rate of 0.02 kg/s the two gaseous sources are not fully mixed by the end of the barrel length (x/L = 1). The gaseous velocity and temperature reductions induced by increasing nitrogen flow rates are quantified by Figure 4.6b at a position half way along the barrel. With a nitrogen inlet mass flow rate of 0.02 kgs^{-1} the gaseous velocity is reduced by up to 500 ms^{-1} close to the barrel wall. Furthermore, the results show the temperature is reduced by up to 750 K close to the wall.

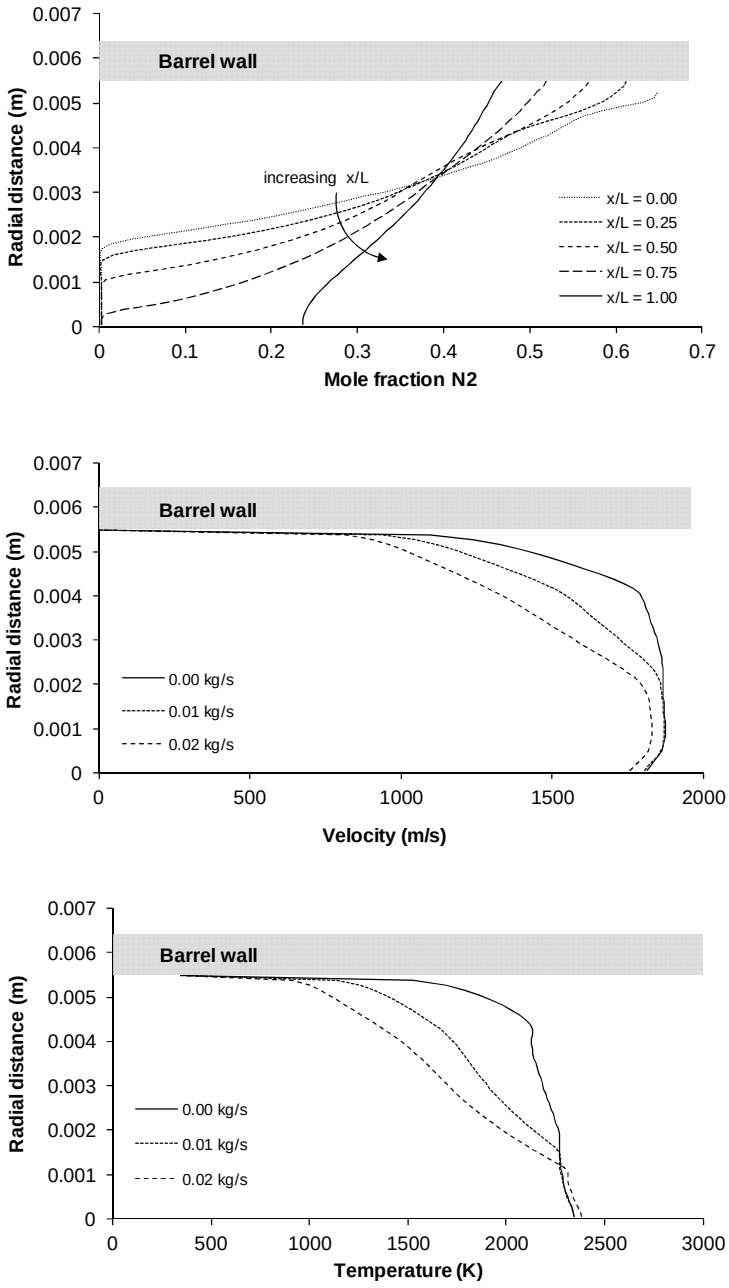

Figure 4.6: Radial nitrogen mole fraction variation (a), Radial velocity variation (b) and radial temperature variation (c) half way along the barrel for varying nitrogen flow rates.

4.3.2 Particle dynamics

Figure 4.7 exhibits the trajectories of 5 μm, 30 μm, and 60 μm diameter particles injected close to the convergent-divergent nozzle. Due to the overlapping dispersion of the 5 μm particles from the two cooling scenarios without and with nitrogen cooling, Figure 4.7a includes only the particles with the most upper, central and lower trajectories of these particles for clarity. The resulting velocity and temperature profiles are plotted in Figures 4.8 and 4.9 and are labelled accordingly. For the 30 μm,

and 60 μm particles only a single velocity and temperature variation is plotted in Figures 4.8 and 4.9 because little dispersion was found for particles greater than 30 μm in diameter.

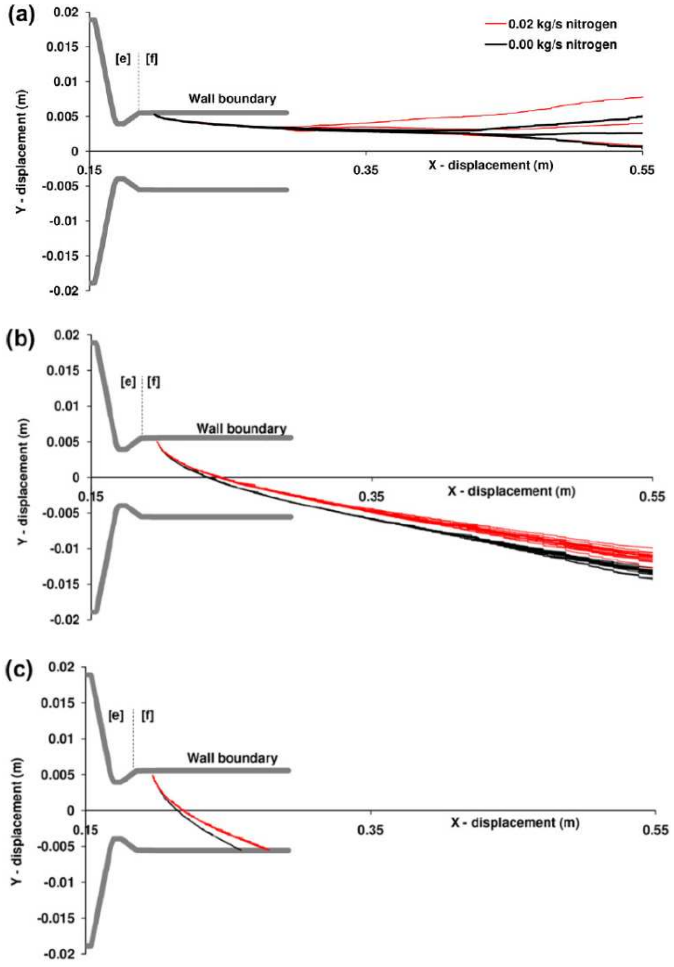

Figure 4.7: Particle trajectory for (a) 5μm (b) 30μm and (c) 60μm diameter particles without and with the nitrogen cooling gas.

The trajectory of the 60 μm diameter particles is slightly affected by the increasing nitrogen rate as depicted in Figure 4.8c. However, these particles are shown to migrate across the barrel and impinge on the barrel wall, with and without nitrogen cooling. In reality these particle are likely to stick to the internal surface of the barrel on impingement, and so the simulation terminates the particle at this point. On the other hand, the 30 μm particles do not impinge, and their velocity is slightly increased by roughly 50 ms^{-1} when 0.02 kgs^{-1} of nitrogen is injected due to the particles following a more central trajectory where the fluid flow is fastest. The 5 μm diameter particles respond quickly to the motion of the fluid and migrate less through the high speed cross flow compared to the larger particles, as exhibited in Figure 4.7a. The 5 μm particles are shown to be swept along the cooler region where in the case of cooling,

the N_2 mole fraction is high and the axial velocity is lower relative to the gas stream along the centre of the barrel. Due to the reduction in velocity of the gas phase in this region in the presence of a cooling gas the velocity of the 5 μm particles is reduced by roughly 200 ms^{-1} at the barrel exit as shown in Figures 4.8a and 4.8b. The greater gas expansion and velocity increase at the barrel exit which occurs in the presence of the cooling nitrogen gas slightly accelerates the 5 μm particles at the barrel exit as shown in Figure 4.8b. Despite this acceleration their maximum velocity remains lower than those which travel within the uncooled gas. The 5 μm particles are shown to disperse more than the 30 μm and 60 μm particles due to their small size and trajectory through the shear layer where the jet and atmosphere interact. In the presence of the nitrogen cooling gas, turbulent mixing in this region is enhanced and the dispersion of the 5 μm particles is increased, as depicted in Figure 4.7a. The further from the central jet the particles are displaced the lower their final velocities. For the case of 0.02 kgs^{-1} of nitrogen cooling the particles are further displaced from the centreline of the external jet and therefore can experience large velocity reductions. Figure 4.7a and the corresponding velocities plotted in Figures 4.8a and 4.8b show that the difference in velocity between the slowest, most displaced particles leaving the computational domain for cases without and with cooling is roughly 200 ms^{-1}.

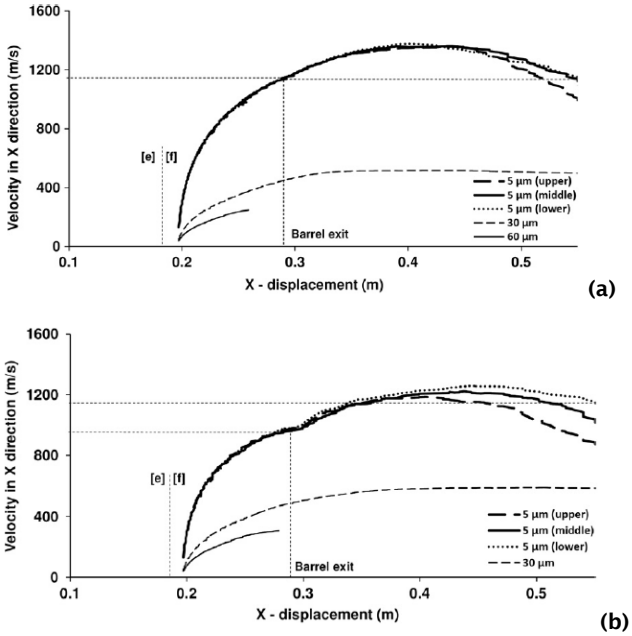

Figure 4.8: Particle velocity variation for 5μm, 30μm and 60μm particles without nitrogen cooling (a) and with 0.02 kgs^{-1} of nitrogen cooling (b).

4.3.3 Particle temperature variation

Figures 4.9a and 4.9b compare the temperature variation for the particles when travelling though the system, with and without the cooling nitrogen gas. When injected without cooling the 5 µm diameter particles are shown to first rapidly heat to their melting point. The temperature then levels while the latent heat of fusion is absorbed and a phase transition from solid to liquid takes place, depicted in Figure 4.9a. The temperature of the 5 µm particles then begins to increase while in the external jet-flame. For the 30 µm particles travelling through the system without cooling, the surface temperature begins to slowly decrease after exiting the barrel, as Figure 4.9 shows. The temperature profiles of the 60 µm particles have little time to develop before colliding with the barrel wall.

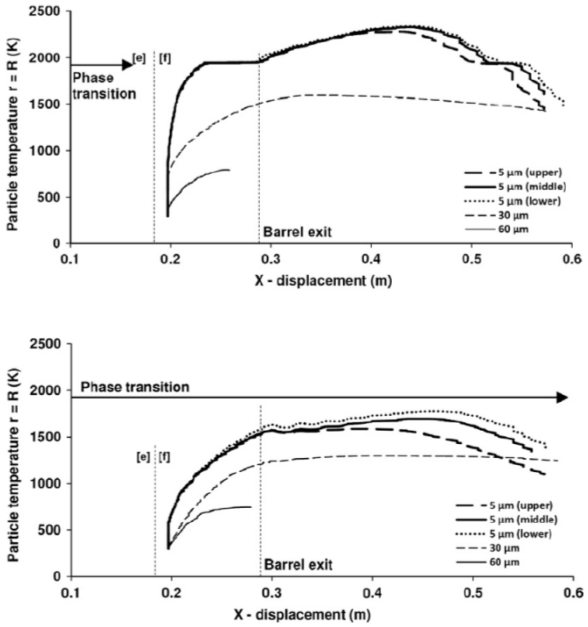

Figure 4.9: Graph showing the variation of particle surface temperatures through the system without cooling (a) and showing the variation of particle surface temperatures through the system with cooling 0.02 kgs^{-1} of nitrogen cooling **(b)**.

The 750 K decrease in gaseous temperature close to the barrel wall with 0.02 kgs^{-1} of nitrogen corresponds to the region were smaller particles are entrained. As the results presented Figures 4.9a and 4.9b indicate, the modified system is capable of cooling 5 µm titanium particles well below their melting point for all particles within the dispersion.

4.4 Discussion

The relative influence of the fluid phase on the trajectory of different size particles can be predicted by the particle Stokes number (St). St is derived as an extension, to Equations 2.1 and 2.2 from Chapter 2, and shows its fundamental importance within the drag equation. St (τ_p/τ_g) is defined as the characteristic response time of the particle divided by the characteristic response time of the fluid. Hence, if St is much less than 1, the particle's motion is tightly coupled to the fluid motion, and when injected in a cross flow, will swiftly change direction. However, as St increases the particle trajectory will be less affected by changes in velocity of the flowing fluid in which it resides.

$$m\frac{du_p}{dt} = \frac{1}{2}C_D A_p \rho\left(u_g - u_p\right)\left|u_g - u_p\right| \tag{4.18}$$

$$\frac{du_p}{dt} = \frac{18\mu_g}{\rho_p d_p^2}\frac{C_D Re_p}{24}\left(u_g - u_p\right)$$

$$\Rightarrow \quad \tau_p = \frac{\rho_p d_p^2}{18\mu_g}$$

$$St = \frac{\tau_p}{\tau_g} = \frac{\rho_p d_p^2 u_g}{18\mu_g D} \tag{4.19}$$

As Equation 4.19 shows, St is related to the square of the particle diameter. For this reason the smaller 5 μm diameter particles have a considerably lower St and therefore experience a more dramatic response to the gas flow. As a result these particles are entrained close to the barrel wall. For the application of the WS device being tested this cross flow drag phenomena plays an important role in its ability to cool the particles. The results indicate that small titanium powder particles with a diameter of roughly 5 μm will otherwise experience complete melting. The WS modification to existing HVOF thermal spray devices can be applied to prevent melting and therefore reduce the levels of oxidation occurring at the surface of smaller titanium particles as well as minimize the chance of molten splashing on impingement to the surface.

For future development of WS better mixing between the hot combustion gases and nitrogen cooling should be made. This would enable more stringent control of the particle temperatures, so that a compromise between the melting of smaller particles and softening of larger particles could be efficiently derived by adjusting the cooling gas flow rates. To ensure a fully mixed gas the barrel length could be increased. However, preferably, a better design should be sought by insuring that the nitrogen gas is mixed to a greater extent prior to the injection of the particle feedstock.

4.5 Conclusion

The combustion reaction and flow regime for a modified HVOF (warm spray) system is resolved for an industrial set of fuel injection parameters. By increasing the nitrogen flow rates the pressure upstream of the CD nozzle increases, which intensifies the under expanded flow regime at the nozzle exit.

Nitrogen cooling gas is concentrated around the barrel wall producing a nitrogen-rich boundary layer, where the gas temperature and axial velocity is lower. Small particles of roughly 5 μm diameter are swept along this outer region when injected. In the case of 0.02 kg/s of nitrogen cooling these particles are further displaced from the centreline of the jet and therefore can experience large velocity reductions. The difference between the slowest particles from this scenario and that without cooling is roughly 200 m/s.

The results of this investigation indicate that with the current design the extent of cooling of the particles is sensitive to their radial position within the barrel. The results show that by injecting nitrogen into the system at a flow rate of 0.02 kg/s at the location specified the otherwise expected melting of 5 μm particles can be avoided with their current injection velocity and angle.

4.6 Chapter nomenclature

General symbols

A_p	particle frontal area (m^2)
C_D	drag coefficient
C_p	specific heat capacity ($J\ kg^{-1}\ K^{-1}$)
C_μ	turbulence empirical constant (0.09)
d	diameter (m)
D	diameter of the nozzle (m)
E	empirical constant (9.793)
f	particle solid mass fraction
F_x	particle force source term ($N\ kg^{-1}$)
H_f	enthalpy of fusion ($J\ kg^{-1}$)
h	convective heat transfer coefficient ($W\ m^{-2}\ K^{-1}$)
k	thermal conductivity ($W\ m^{-1}\ K^{-1}$)
L_e	eddy length scale (m)
m	mass (kg)
Nu	Nusselt number

Pr	Prandtl number
r	radial distance from the centre of a particle (m)
r_p	particle radius (m)
Re_p	relative particle Reynolds number
t	time (s)
t_{cross}	eddy crossing time (s)
T	temperature (K)
T_l	liquidus temperature
T_s	solidus temperature
T_L	integral time scale (s)
u	velocity (m s^{-1})
u’	turbulent velocity fluctuation (m s^{-1})
U	mean velocity of the fluid at the near-wall node (m s^{-1})
y_p	distance from point P to the wall (m)
y*	dimensionless distance from the wall

Greek symbols

α	thermal diffusivity (m^2s^{-1}).
μ	viscosity (kgm^{-1} s^{-1})
ρ	density (kg m^{-3})
κ	von Karman constant (0.4187)
λ	turbulence kinetic energy at point P (m^2 s^{-2})
ζ	Gaussian random number

Subscript symbols

g	gas
l	liquidus
p	particle
R	particle radius
s	solidus

4.7 Chapter appendix

T (K)	k
0 ≤ T < 22.5	15.8
22.5 ≤ T < 125	35.3
125 ≤ T < 550	22.0
550 ≤ T < 1050	19.9
1050 ≤ T < 1550	22.8
1550 ≤ T < 1950	26.5
T ≥ 1950	28.0

Table A.2: Thermal conductivity of titanium, W/(m K) (Touloukian et al. 1970)

T (K)	C_p
T < 294.1	521.3
294.1 ≤ T < 622.7	564.84
622.7 ≤ T < 1079.2	694.1
1079.2 ≤ T < 1163.2	752.28
T ≥ 1163.2	699.6

Table A.3: Specific heat capacity of titanium, J/(kg K) (Touloukian & Buyco 1971)

5 Liquid droplet disintegration for nanostructured coatings

Thermal spray coatings produced from a liquid feedstock are receiving an increasing level of interest due to the more advanced, nanostructured coatings which are obtainable by these processes. In this chapter a HVOF thermal spray system is computationally investigated in order to make a scientific assessment of the liquid droplet behaviour on injection. An existing liquid-fuelled HVOF thermal spray gun is simulated using the CFD approach as outlined in Chapter 2. Discrete phase water droplets are injected at the powder injection port. Upon injection, the water droplets breakup and vaporize while being entrained through the acceleration barrel of the HVOF system. The results obtained give an insight to the mechanism which control the water droplet sizes and disintegration process, and serve as a fundamental reference for future development of liquid feedstock devices.

5.1 Chapter introduction

As outlined in Chapter 1, there is a growing desire to deposit nanostructured films. However, the deposition of submicron and nano-sized particles requires current techniques to be adapted. For both health and safety reasons as well as to avoid particle agglomeration during storage and feeding into the spray device, a nano-powder feedstock has to be mixed to form a suspension (suspension thermal spraying, STS) or a solution precursor (solution precursor thermal spraying, SPTS). In comparison to the conventional thermal spray methods, STS and SPTS are more complex due to the final particle morphology being largely controlled by the rates of fragmentation and vaporization of the liquid component of the feedstock upon injection. Detailed images of the initial disintegration of liquid feedstock injection are provided in (Meillot et al. 2008), exhibiting both stripping and catastrophic break-up of the droplets. Depending on the size of the liquid droplets, the intensity of the flow and the liquid feedstock properties, the droplets may precipitate their solid mass along one of many process routes, as depicted in Figure 5.1. A simulation study of liquid ceramic precursor droplets processed by plasma and HVOF spraying are presented in (Basu & Cetegen 2007) and (Basu & Cetegen 2008), providing some explanation to these different precipitation routes. These results show smaller feedstock droplets form a thicker precipitate shell and are more likely to form solid particles due to rapid heating and vaporization. Larger droplets however, undergo surface precipitation forming a shell. Depending on the shell porosity and ability to vent the evaporating liquid core this shell structure can erupt due to internal pressurization. Furthermore, the temperatures associated with HVOF are lower than plasma spray methods, leading to larger powder

particle diffusion times within feedstock droplets and therefore are more likely to produce a thick shell and solid uniform agglomerates (Basu & Cetegen 2008).

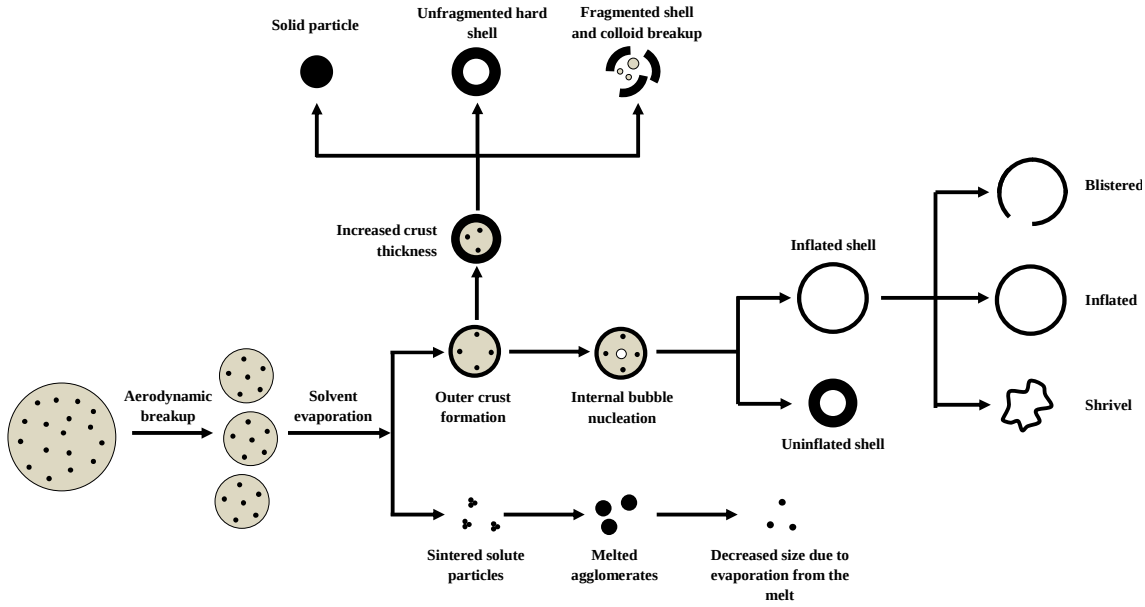

Figure 5.1: Variations in liquid feedstock droplet disintegration and drying.

Experiments using modified HVOF thermal spraying with a liquid feedstock indicate that if the feedstock is water based, poorer coatings might be created due to insufficient flame temperatures when mixing within the combustion chamber (Gadow et al. 2008). However, the water-based feedstock allows higher particle concentrations, are less expensive to produce, and are safer to handle compared to the organic alternatives (Tikkanen et al. 1997). Better coatings have been obtained when the feedstock is a combustible, organic-based compound. However, injecting a combustible liquid into the combustion chamber raises the pressure and can lead to instabilities in the flow (Fauchais & Montavon 2010).

Despite the work undertaken to date in the fields of STS and SPTS as outlined in Chapter 1, several investigations are still very necessary to improve our fundamental understanding of spray kinematics; suspension and solution feedstock properties; and injection systems. This present study investigates liquid droplet disintegration within a supersonic combustion flame, based on HVOF-type processing. A good overview of the combustion characteristics and supersonic flow field can be found in Chapters 2 and 4 (Tabbara & Gu 2009, Tabbara & Gu 2011) for the HVOF and modified HVOF systems respectively. The water droplets at room temperature and various sizes are introduced at the normal powder feeder location. A detailed study is then conducted to assess the manner of droplet disintegration within the barrel of a standard HVOF system, close to

the de Laval nozzle. By incorporating detailed thermophysical properties of water the primary and secondary break up regimes are captured and compared to the timescales involved with those of vaporizing droplets. The information obtained sheds new light on the process of water droplet disintegration and serves as a reference for future development of liquid feedstock devices.

5.2 Model description

5.2.1 An overview of the gas phase modelling techniques

A schematic diagram of the JP5000 thermal spray system is illustrated in Figure 5.2 highlighting the fuel-oxygen inlet, the combustion chamber, the convergent-divergent nozzle, and the barrel. Details of the computation domain, boundary conditions, and refinement regions are given in Chapter 2 (Tabbara & Gu 2009). The geometric parameters are the same as those listed in Chapter 2 (Tabbara & Gu 2009) and the inlet fuel flow conditions are listed in Chapter 4 (Tabbara et al. 2011).

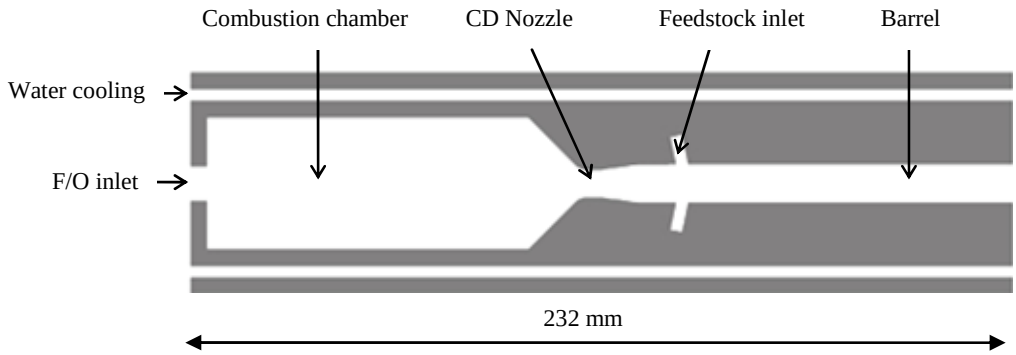

Figure 5.2: Schematic diagram of the JP5000 thermal spray system

The segregated solution algorithm (Van Doormal et al. 1987) is applied in this study with a control volume-based technique. This numerical method is chosen over the alternative coupled approach in order to aid convergence and avoid oscillations in the pressure and velocity fields. The pressure and velocity fields are linked using the SIMPLE (semi-implicit method for pressure linked equations) algorithm (Raithby & Schneider 1979) due to it being computationally economical and more stable in comparison to other algorithms. The second order upwind scheme is employed to discretise the transport equations. Details of these numerical schemes can be found in the appendix of this thesis.

The steady state flow field of the gaseous continuum is computed using the Reynolds averaged Navier-Stokes equations (RANS) and is assumed to behave as a compressible, ideal gas. The absolute pressure is represented by the sum of the

operating pressure and the static pressure of the flow. The variable density is calculated by taking into account the mass fraction of each species in the flow as given in Equation 5.1.

$$\rho = \frac{p_{op} + p}{RT \sum_i \frac{Y_i}{M_{\omega,I}}} \tag{5.1}$$

The continuity equation for the steady state, axisymmetric computations is given by Equation 5.2. The terms on the left hand side represent the mass entering and leaving a control volume and the change in mass due to a change in density. The S_m term is the additional mass contribution from the vaporizing kerosene fuel droplets, where x is the axial coordinate, r is the radial coordinate, v_x is the axial velocity, and v_r is the radial velocity. The individual water droplets are the focus of this study, and are injected as single droplets in order to make particular assessment of individual droplet behaviour. These droplets are one way coupled and therefore do not impact on the gas phase dynamics.

$$\frac{\partial}{\partial x}(\rho v_x) + \frac{\partial}{\partial r}(\rho v_r) + \frac{\rho v_r}{r} = S_m \tag{5.2}$$

The axial and radial momentum conservation equations are given in Equations 5.3 and 5.4 in their cylindrical form. The effective viscosity is equal to the sum of the physical dynamic viscosity and the artificial turbulent viscosity, which is used to account for the enhanced mixing due turbulent fluctuations within the mean flow. The flow in this case is compressible; hence the two equations below are Favre averaged. The radial and axial sources F_r and F_x represent the volumetric forces due to interaction with the dispersed kerosene fuel droplets.

$$\frac{1}{r}\frac{\partial}{\partial x}(r\rho v_x v_x) + \frac{1}{r}\frac{\partial}{\partial r}(r\rho v_r v_x) = -\frac{\partial p}{\partial x} + \frac{1}{r}\frac{\partial}{\partial x}\left[r\mu_{eff}\left(2\frac{\partial v_x}{\partial x} - \frac{2}{3}(\nabla \cdot \vec{v})\right)\right] \tag{5.3}$$

$$+\frac{1}{r}\frac{\partial}{\partial r}\left[r\mu_{eff}\left(\frac{\partial v_x}{\partial r} + \frac{\partial v_r}{\partial x}\right)\right] + F_x$$

$$\frac{1}{r}\frac{\partial}{\partial x}(r\rho v_x v_r) + \frac{1}{r}\frac{\partial}{\partial r}(r\rho v_r v_r) = -\frac{\partial p}{\partial r} + \frac{1}{r}\frac{\partial}{\partial x}\left[r\mu_{eff}\left(\frac{\partial v_r}{\partial x} + \frac{\partial v_x}{\partial r}\right)\right] \tag{5.4}$$

$$+\frac{1}{r}\frac{\partial}{\partial r}\left[r\mu_{eff}\left(2\frac{\partial v_r}{\partial r} - \frac{2}{3}(\nabla \cdot \vec{v})\right)\right]$$

$$-2\mu_{eff}\frac{v_r}{r^2} + \frac{2}{3}\frac{\mu_{eff}}{r}(\nabla \cdot \vec{v}) + F_r$$

Where,

$$\nabla \cdot \vec{v} = \frac{\partial v_x}{\partial x} + \frac{\partial v_r}{\partial r} + \frac{v_r}{r} \tag{5.5}$$

The energy conservation equation is given below, and is linked to the conservation of mass and momentum through the multi-species ideal gas law (Equation 5.1). The source term S_h represents the energy dissipated and received by the gas phase during the vaporization and exothermic combustion reaction of the kerosene fuel droplets within the combustion chamber.

$$\frac{\partial}{\partial x}[v_x(\rho E + p)] + \frac{\partial}{\partial r}[v_r(\rho E + p)] = \frac{\partial}{\partial x}(v_x\sigma_{xx} + v_r\tau_{xr} + q_x) + \frac{\partial}{\partial x}(v_x\tau_{xr} + v_r\sigma_{rr} + q_r) + S_h \tag{5.6}$$

$$\sigma_{xx} = 2\mu_{eff}\frac{\partial v_x}{\partial x} - \frac{2}{3}\mu_{eff}(\nabla \cdot \vec{v}) \tag{5.7}$$

$$\sigma_{rr} = 2\mu_{eff}\frac{\partial v_r}{\partial r} - \frac{2}{3}\mu_{eff}(\nabla \cdot \vec{v}) \tag{5.8}$$

$$\tau_{xr} = \tau_{rx} = \mu_{eff}\left(\frac{\partial v_x}{\partial r} + \frac{\partial v_r}{\partial x}\right) \tag{5.9}$$

$$q_x = K_{eff}\frac{\partial T}{\partial x} \tag{5.10}$$

$$q_r = K_{eff}\frac{\partial T}{\partial r} \tag{5.11}$$

The kerosene liquid fuel in the present study $C_{12}H_{26}$ is used to represent the average size of the kerosene hydrocarbon chain. The combustion reaction is represented by a single, one-step global reaction scheme, as given in Equation 5.12.

$$n_1C_{12}H_{26} + n_2O_2 \xrightarrow{-\Delta H} n_3CO_2 + n_4H_2O + n_5CO + n_6OH + n_7O_2 + n_8O + n_9H_2 + n_{10}H \tag{5.12}$$

The eddy-dissipation model (Magnussen & Hjertager 1976) is adopted to predict the rate of combustion reaction between kerosene and oxygen. This method is a turbulence-chemistry interaction model, where the rate ($R_{i,r}$) at which species i is produced due to reaction r, is given by the limiting value of Equations 5.13 and 5.14. An iterative approach is used (M. Li & Christophides 2009) in order to estimate the mole fraction of each product species appearing on the right hand side of Equation 5.12, in order to achieve the correct combustion chamber pressure and thermal flow field.

$$R_{i,r} = v'_{i,r}M_{\omega,i}A\rho\frac{\varepsilon}{k}\min_R\left(\frac{Y_R}{v'_{R,r}M_{\omega,R}}\right) \tag{5.13}$$

$$R_{i,r} = v'_{i,r}M_{\omega,i}AB\rho\frac{\varepsilon}{k}\left(\frac{\sum_P Y_P}{\sum_J^N v''_{j,r}M_{\omega,j}}\right) \tag{5.14}$$

The k-ε model (Launder & Spalding 1972) is the most frequently used turbulence model in computing flows within a practical engineering environment. The model assumes that the turbulent viscosity of the flow is isotropic and the flow is fully turbulent. One of the main downfalls of the standard k-ε model is its inability to accurately predict the spreading rate of an axisymmetric planar jet. This problem was thought to originate within the equation of turbulent dissipation. Hence, the realizable k-ε model (Shih et al. 1995) addresses this by containing a modified transport equation to describe the rate of turbulent dissipation. Equations 5.15 and 5.16 describe the transport of turbulent kinetic energy and the rate of turbulent dissipation.

$$\frac{\partial}{\partial r}(r\rho k v_r) + \frac{\partial}{\partial x}(r\rho k v_x) = \frac{\partial}{\partial x}\left(r\left(\mu + \frac{\mu_t}{\sigma_\kappa}\right)\frac{\partial k}{\partial x}\right) + \frac{\partial}{\partial r}\left(r\left(\mu + \frac{\mu_t}{\sigma_\kappa}\right)\frac{\partial k}{\partial r}\right) + r(G_k + G_b - \rho\epsilon - Y_M) \quad (5.15)$$

$$\frac{\partial}{\partial x}(r\rho\varepsilon v_x) + \frac{\partial}{\partial r}(r\rho\varepsilon v_r) = \frac{\partial}{\partial r}\left(r\left(\mu + \frac{\mu_t}{\sigma_\varepsilon}\right)\frac{\partial \varepsilon}{\partial r}\right) + \frac{\partial}{\partial x}\left(r\left(\mu + \frac{\mu_t}{\sigma_\varepsilon}\right)\frac{\partial \varepsilon}{\partial x}\right) \quad (5.16)$$

$$+ r\left(\rho C_1 S_\varepsilon - \rho C_2 \frac{\varepsilon^2}{k + \sqrt{\upsilon\varepsilon}} + \rho C_{1\varepsilon}\frac{\varepsilon}{k}\, C_{2\varepsilon} G_b\right)$$

The realizable model also considers the requirement of a more complete description of the normal stresses, which makes the model physically more complete. The normal stress is by definition, positive and to satisfy this requirement C_μ is made variable in relation to the mean flow and the turbulence, as defined in Equation 5.17. The variable C_μ is then directly applied to estimate the tubulent viscosity μ_t in Equation 5.18.

$$C_\mu = \frac{1}{A_0 + A_s(kU^*/\varepsilon)} \quad (5.17)$$

$$\mu_t = \rho_g C_\mu \frac{k^2}{\varepsilon} \quad (5.18)$$

5.2.2 Water droplet dynamics with heat and mass transfer

Spherical, discrete phase water droplets are injected vertically into the barrel at the standard powder inlet port, as shown in Figure 5.2. The acceleration of each droplet particle is calculated using Newton's second law, equating the inertia of each droplet with the forces applied by the continuum, described by Equation 5.19.

$$\frac{du_p}{dt} = \frac{18\mu}{\rho_p d_p^2}\frac{C_D Re_p}{24}\left(v - u_p\right) + F_t \quad (5.19)$$

Subsequently, the trajectory of each droplet is tracked by computing its displacement through time. F_t is a source term which accounts for the thermophoretic force. This force arises due to temperature gradients within the flow. As outlined in previous

studies (Crowe et al. 1998), in particle laden flows where the relative Mach number M_r exceeds 0.6 shock patterns form on the particle surface. Therefore, the calculation of the particle drag force should include both the particle Reynolds number and the relative Mach number. For this reason the drag force coefficient C_D is calculated using the model proposed by Henderson (1976), as given in Equations 5.20, 5.21 and 5.22.

IF M < 1: (5.20)

$$C_D = 24\left[Re + S\left\{4.33 + \left(\frac{3.65 - 1.53\frac{T_p}{T}}{1 + 0.353\frac{T_p}{T}}\right) \times exp\left(-0.247\frac{Re}{S}\right)\right\}\right]^{-1}$$

$$+ exp\left(-\frac{0.5M}{\sqrt{Re}}\right)\left[\frac{4.5 + 0.38\left(0.03Re + 0.48\sqrt{Re}\right)}{1 + 0.03Re + 0.48\sqrt{Re}} + 0.1M^2 + 0.2M^8\right]$$

$$+ \left[1 - exp\left(-\frac{M}{Re}\right)\right] 0.6\,S$$

IF M > 1.75: (5.21)

$$C_D = \frac{0.9 + \frac{0.34}{M_\infty^2} + 1.86\left(\frac{M_\infty}{Re_\infty}\right)^{0.5}\left[2 + \frac{2}{S_\infty^2} + \frac{1.058}{S_\infty}\left(\frac{T_p}{T}\right)^{0.5} - \frac{1}{S_\infty^4}\right]}{1 + 1.86\left(\frac{M_\infty}{Re_\infty}\right)^{0.5}}$$

IF $1 < M < 1.75$ (5.22)

$$C_D(M_\infty, Re_\infty) = C_D(1, Re_\infty) + \frac{4}{3}(M_\infty - 1)[C_D(1.75, Re_\infty) - C_D(1, Re_\infty)]$$

The droplet temperature during heating and vaporization is governed by Equation 5.23. The convective heat transfer coefficient between each droplet and the gaseous phase in which they are submersed is calculated using the Ranz-Marshall correlation (Ranz & Marshall 1952a, 1952b) in Equation 5.24. The variation in specific heat capacity with temperature for liquid water is applied using data presented in (Touloukian 1970).

$$m_p c_p \frac{dT_p}{dt} = hA_p\left(T_\infty - T_p\right) + \frac{dm_p}{dt} h_{fg} \tag{5.23}$$

$$Nu = \frac{hd_p}{K_\infty} = 2.0 + 0.6 Re_p^{\frac{1}{2}} Pr^{\frac{1}{3}} \tag{5.24}$$

During vaporization the reduction of the droplet's mass begins to reduce in accordance to Equation 5.25. If N_i is negative and hence the droplet temperature is

lower than the dew point a condensation condition would exist. In this instance N_i is set to zero, and the droplet will undergo inert heating and cooling. The vapour concentration at the droplet outer surface $C_{i,s}$ is calculated by assuming that the vapour partial pressure is equivalent to its saturation vapour pressure, p_{sat} at T_p. The relationship between the temperature of the droplet T_p and the saturation vapour pressure $P_{sat}(T_p)$ is calculated using the well know Clapeyron-Clausius relation (Cengal & Boles 2002).

$$m_p(t + \Delta t) = m_p\,(t) - N_i A_p M_{\omega,i} \Delta t \tag{5.25}$$

Where,

$$N_i = K_c(C_{i,s} - C_{i,\infty})$$

$$C_{i,s} = \frac{p_{sat}(T_p)}{RT_p}$$

$$C_{i,\infty} = X_i \frac{p_{op}}{RT_\infty}$$

The mass transfer coefficient is evaluated through the Sherwood number correlation (Ranz & Marshall 1952a, 1952b), given by Equation 5.26. The diffusion coefficient is calculated using the binary diffusion relation provided by (Bird 1960), whereby the average molecular weight of the gas phases is calculated using the mass-fraction of each gaseous species within the gas phase surrounding the vaporizing droplet.

$$k_c = \frac{D_{i,m}}{d_p}\left(2.0 + 0.6Re_p^{\frac{1}{2}}Sc^{\frac{1}{3}}\right) \tag{5.26}$$

5.2.3 Droplet breakup

For the simulation of primary droplet break up the wave breakup model (Reitz 1987) is applied which simulates the stripping breakup mechanism. This model is appropriate for high speed applications, where We > 100, as defined in Equation 5.27. The model considers the breakup of the droplets due to the relative velocity between the gas and liquid phases creating Kelvin-Helmholtz instabilities. The model assumes that the time of breakup and the resulting droplet sizes are related to the fastest-growing Kelvin-Helmholtz instabilities at the droplet surface where the droplet-gas interface exists.

$$We = \frac{\rho_\infty V_{rel}^2 d_p}{\sigma} \tag{5.27}$$

The droplet breakup is simulated by assuming the radius of the child droplets is proportional to the wavelength of the fastest-growing unstable surface wave on the

parent droplet, as described by Equation 5.28, and depicted in Figure 5.3, where B_0 is a model constant equal to 0.61 (Reitz 1987). The maximum growth rate, Ω, and its corresponding wavelength, Λ, are estimated by Equations 5.29 and 5.30 respectively.

$$r_p = B_0 \Lambda \tag{5.28}$$

$$\Omega = \frac{(0.34 + 0.38We_2^{1.5})}{(1+Oh)(1+1.4Ta^{0.6})}\left(\frac{\rho_1 a^3}{\sigma}\right)^{-1} \tag{5.29}$$

$$\Lambda = 9.02a\frac{(1+0.45Oh^{0.5})(1+0.4Ta^{0.7})}{(1+0.87We_2^{1.67})^{0.6}} \tag{5.30}$$

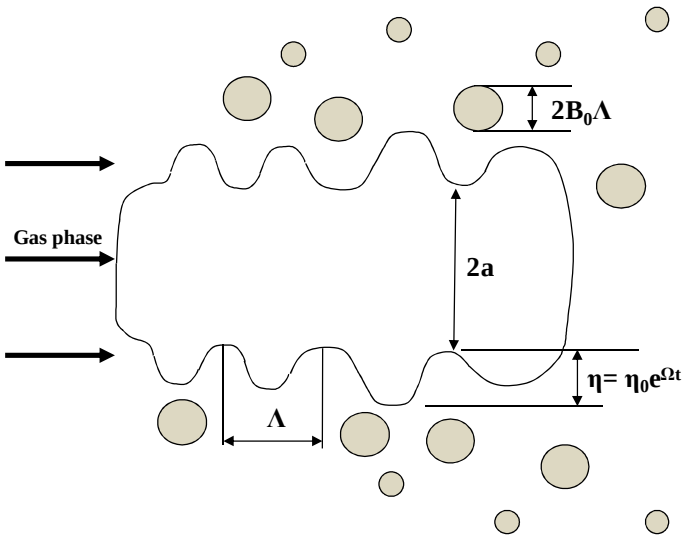

Figure 5.3: Diagram showing surface wave and breakup mechanism on a liquid blob droplet

The rate of change of droplet radius of the parent droplet is calculated by Equation 5.31, where the break-up time τ is given in Equation 5.32. The model constant B_1 is tested for values of 1 and 10. Variations in viscosity and surface tension with temperature for the liquid water droplets are applied using data correlations from (Deguchi et al. 2006) and (Kestin et al.1984) respectively.

$$\frac{da}{dt} = -\frac{(a - r_p)}{\tau_p} \tag{5.31}$$

$$\tau_p = \frac{3.726B_1 a}{\Lambda\Omega} \tag{5.32}$$

For the secondary droplets whose We are far less than 100, the Taylor analogy breakup (TAB) model is applied. This approach is based upon Taylor's analogy (Taylor 1963) between an oscillating and distorting droplet and a spring mass system. When the oscillations of the parent droplet grow to a critical value, break up occurs, and

several smaller droplets are created. The criterion for droplet break up is based on the distortion ratio. The non-dimensional mass, spring, damper system for the calculation of droplet distortion is given in Equation 5.33, where break up occurs if y > 1.

$$\ddot{y} = \frac{C_F}{C_b}\frac{\rho_g}{\rho_p}\frac{V_{rel}^2}{r_p^2} - \frac{C_k\sigma}{\rho_p r_p^3}y - \frac{C_d V_{rel}}{\rho_p r_p^2}\dot{y} \tag{5.33}$$

The droplet oscillation frequency and the undamped oscillation amplitudes are calculated using Equations 5.34 and 5.35. Breakup is only possible if the condition in Equation 5.36 is met.

$$A = \sqrt{(y^n - We_c)^2 + \left(\frac{(dy/dt)^n}{\omega}\right)^2} \tag{5.34}$$

$$\omega^2 = C_k\frac{\sigma}{\rho_l r^3} - \frac{1}{t_d^2} \tag{5.35}$$

$$We_c + A > 1 \tag{5.36}$$

If this condition is met, the breakup time is calculated based on the time required for *y* to equal unity. If the breakup time is greater than the droplet time at the next droplet time step then breakup will not occur during the current time step, and *y* and (*dy/dt*) are updated accordingly. On the other hand, if the current and next droplet time steps are lees than and greater than the droplet breakup time respectively, breakup will occur. The child droplet radii are determined by Equation 5.37, which is derived by equating the energy of the parent droplet to the combined energy of the child droplets.

$$r_{32} = \frac{r}{1 + \frac{8Zy^2}{20} + \frac{\rho_p r^3 (dy/dt)^2}{\sigma}\left(\frac{6Z-5}{120}\right)} \tag{5.37}$$

The empirical constants applied for the Wave Breakup Model and TAB model are based on recommended values, and the predicted breakup times and child droplet sizes compare well to experimental observations, as presented later in this investigation.

5.3 Results and discussion

5.3.1 Gas flow dynamics

The steady state, compressible flow field through the HVOF thermal spray system is captured based on the industrial fuel and oxygen injection flow rates. The simulated velocity distribution at the barrel exit is compared to experimental observations

(Hackett & Settles 1995) in Figure 5.4, with the simulated under expanded jet structure showing a good physical likeness.

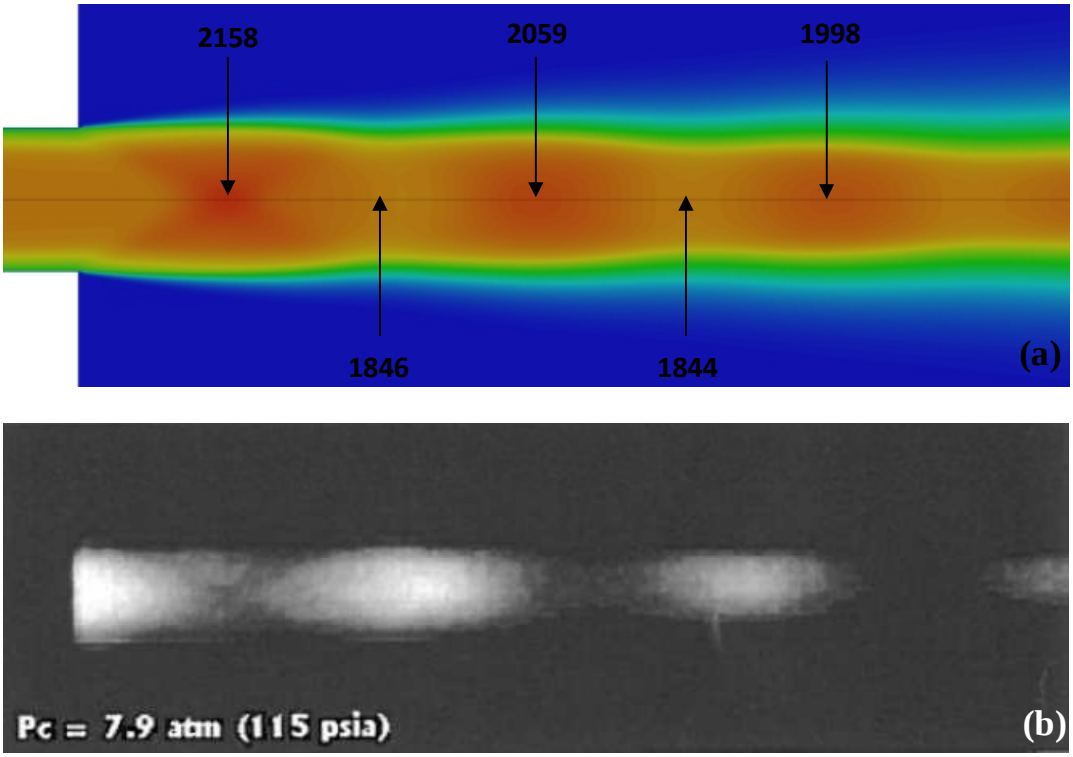

Figure 5.4: Comparison between simulated gas phase velocity contours (ms^{-1}) (a) and an experimental image (Hackett & Settles 1995) (b) of the under expanded flow regime at the JP5000 barrel exit.

The maximum flame temperature within the combustion chamber is compared to the expected values for varying equivalence ratios in Figure 5.5a, and the temperature variations at the exit of the barrel are also compared to experimental measurements (Swank et al. 1994) in Figure 5.5b, both showing good concordance. The pressure, temperature and velocity profiles along the centreline are plotted in Figure 5.6. Descriptions for similar scenarios can be found in Chapters 2 and 4.

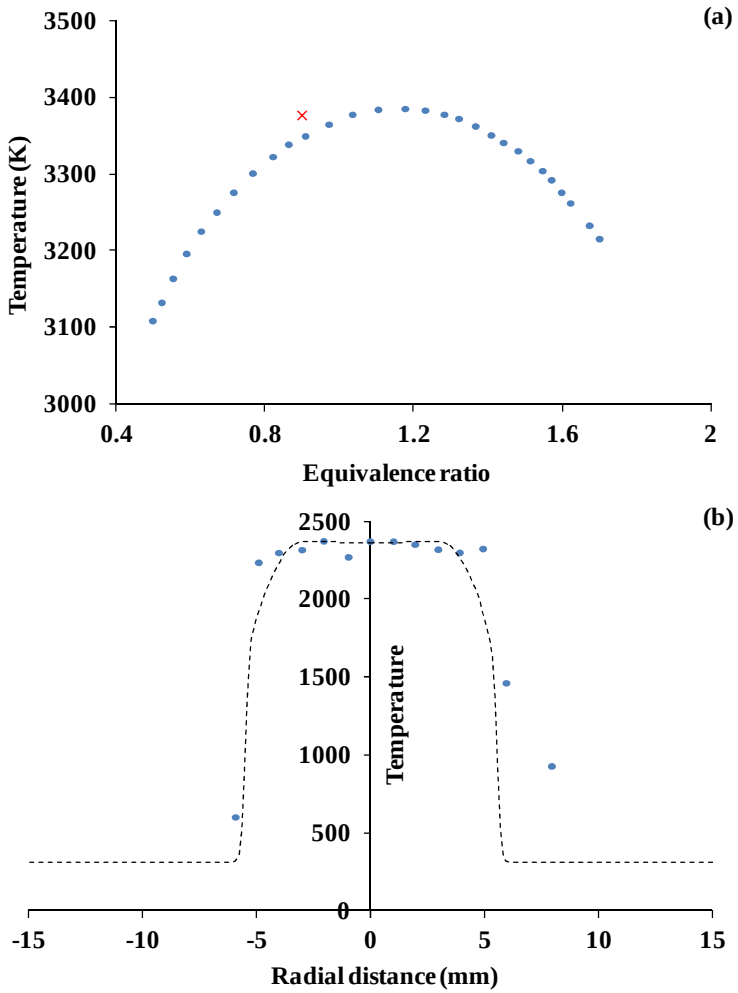

Figure 5.5: Graph showing the flame temperature variation for changes in equivalence ratio (a) and comparison between point measured temperatures (Swank et al. 1994) and modelled temperature distribution at the exit of the barrel (b)

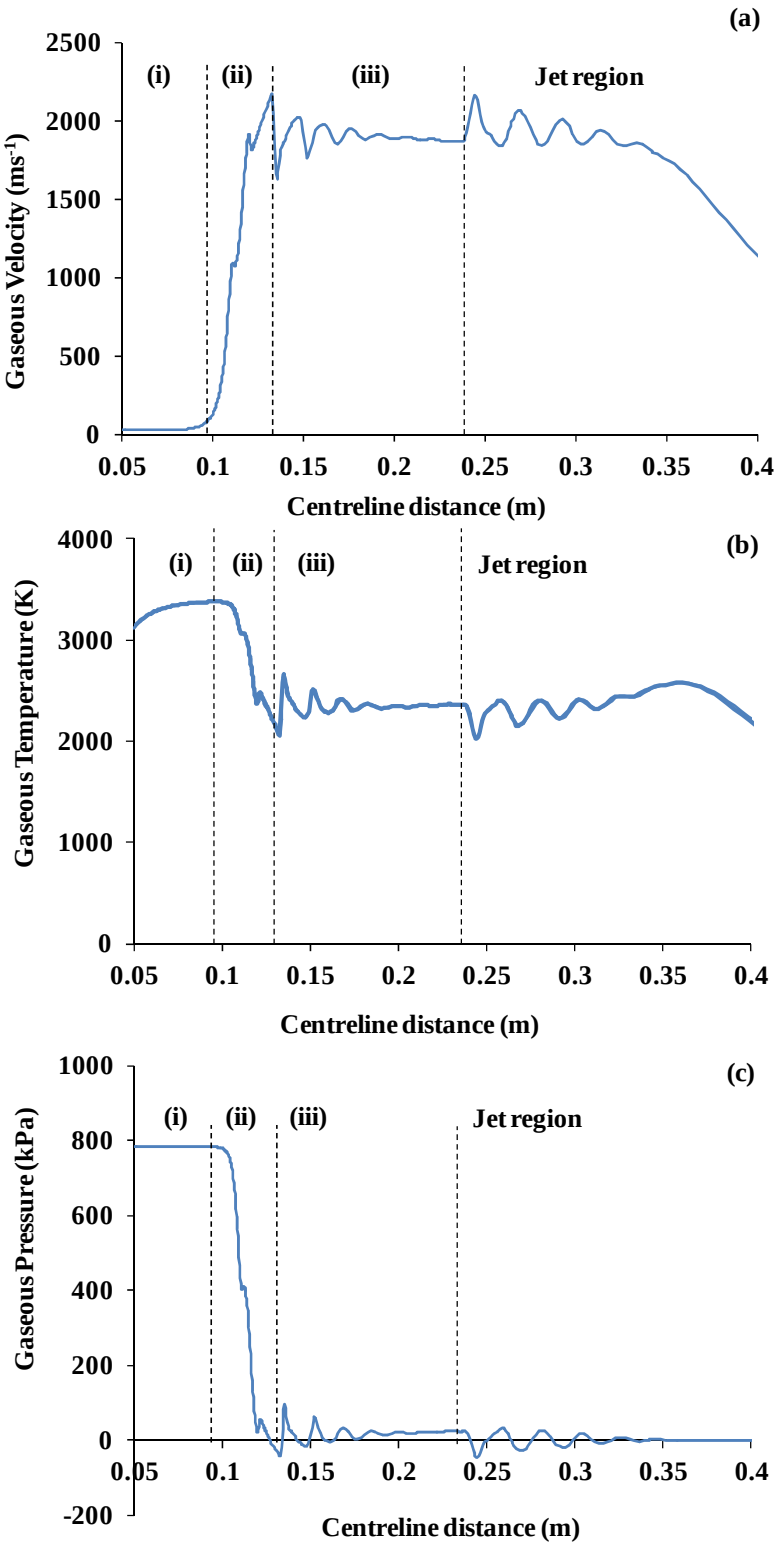

Figure 5.6: Variations in gaseous velocity (a), temperature (b), and pressure (c) along the centreline of the simulated HVOF torch.

5.3.2 Droplet investigation

Water droplets are injected radially into the barrel at the powder inlet port 0.138 m from the combustion chamber back wall, as depicted in Figure 5.2. Their initial droplet velocity is 20 ms^{-1}, and this process is repeated for droplet sizes varying between 50 µm and 500 µm. Firstly, the droplets are simulated to breakup without vaporisation as predicted by the Wave Breakup Model. Figure 5.7 describes the modelled linear decrease in a 50 µm parent droplet diameter as the child droplets are shed from its surface. The modelling constant B_1 is set to both 1 and 10. These values represent a lower and upper limit of this coefficient and directly control the rate at which the droplet breaks up (Equation 5.31).

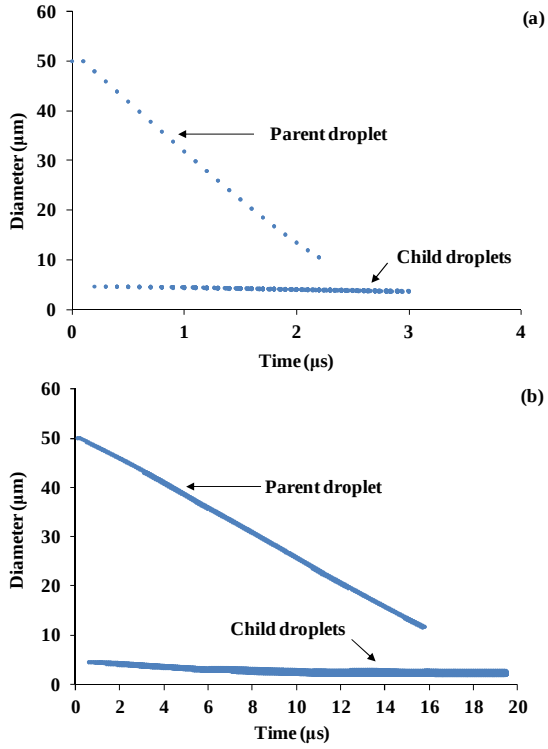

Figure 5.7: Graph describing the rate of decrease in 50 µm droplet diameter and the child droplet sizes for B_1 values of 1 (a) and 10 (b).

The time taken for the 50 µm parent droplet to completely breakup is therefore estimated to be between 2.2 µs and 16.5 µm. This process is repeated for increasing droplet sizes, and the time taken for each parent droplet to shed all of its mass is plotted in Figure 5.8 for both values of B_1. For the 500 µm parent droplet this time may therefore be between 17 µs and 115 µs.

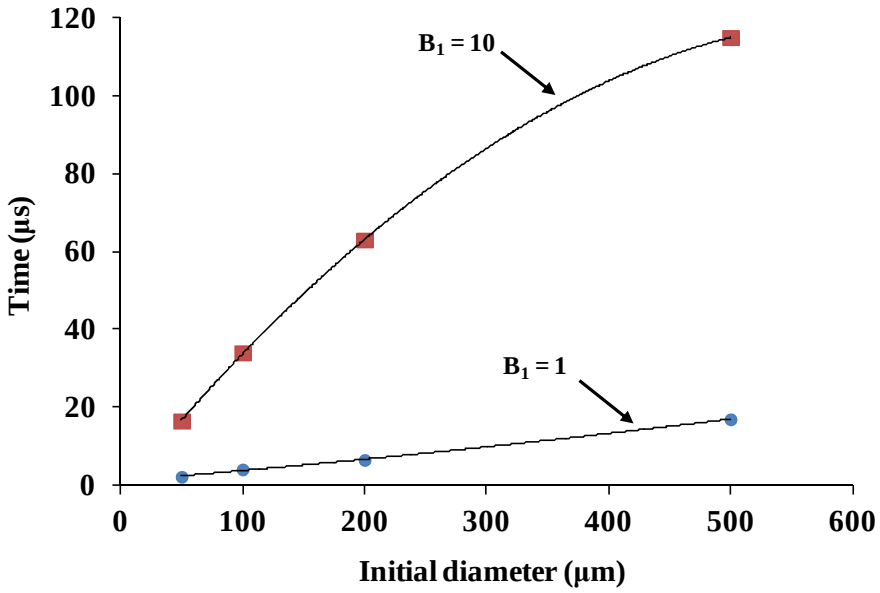

Figure 5.8: Graph comparing the time required for different sized initial parent droplets to shed all of their mass. Both sets of data for B_1 values of 1 and 10 are presented.

Figure 5.9a plots the converging size of the child droplets during the break-up process with initial parent droplet diameters varying from 50 µm to 500 µm, as predicted by the Wave Breakup Model. The dimensionless time in this graph represents the total time from injection of the initial parent droplet divided by the time taken for the initial parent droplet to completely disintegrate (see Figure 5.8) with a B_1 value of unity. Due to the continuing decrease in child droplet size beyond a dimensionless time of 1, it is clear a secondary atomization process is simulated. The primary child droplets are filtered from the data presented in Figure 5.9a and are plotted Figure 5.9b. The results indicate that the initial primary child droplets are roughly 4.5 - 4.6 µm in size for all of the tested parent droplets. The data obtained also indicates that as the intial parent droplet size is increased from 50 µm to 500 µm the average primary child droplet size decreases. Consequently, the minimum primary droplet size obtained is 2.3 µm for the 500 µm parent droplet.

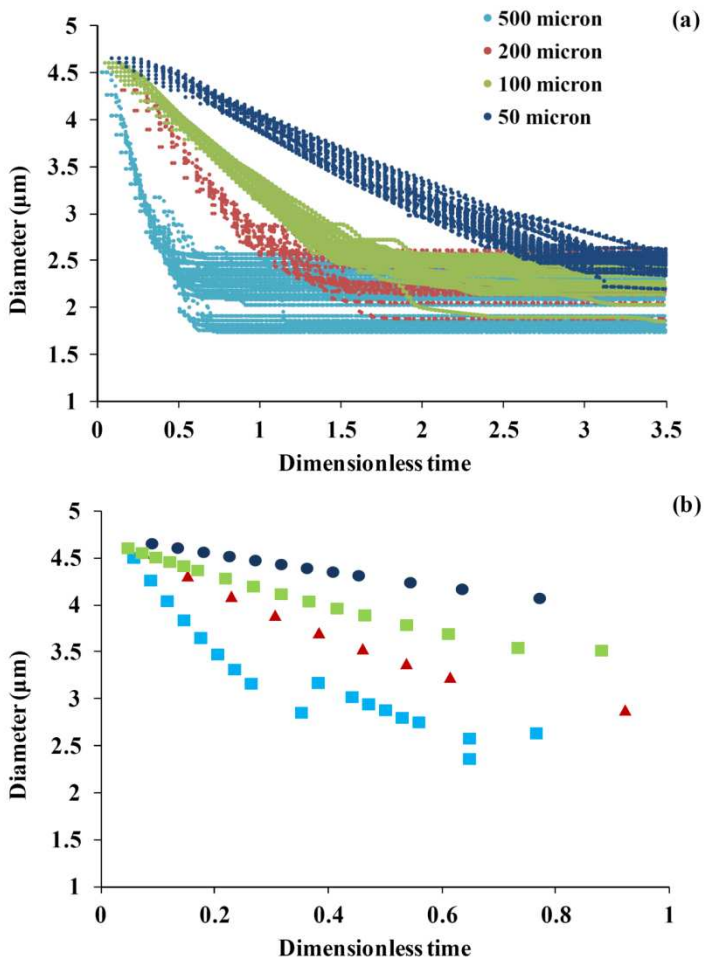

Figure 5.9: Stabilization of child droplet sizes for different initial parent droplets (a) and filtered results containing only initial primary child droplets (b).

Figure 5.10 describes the rate of evaporation and decrease in droplet diameter of a 50 µm droplet without breakup being modelled. The results indicate that a 50 µm diameter droplet only decreases by 6 µm in a time of 0.5 ms, at which point the parent droplet reaches the exit of the computational domain. Furthermore, the decrease in particle diameter due to evaporation within the time taken for the 50 µm droplet to shed its mass during breakup (i.e. between 2.2 µs to 16 µm) is at most 0.03%. From these result, it is clear that the primary droplet break up regimes for the tested parent droplets occur on a much smaller time scale compared to the vaporization process.

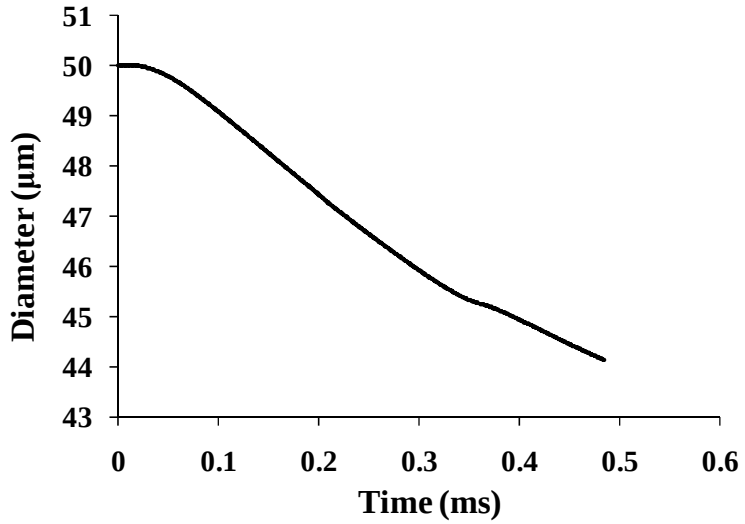

Figure 5.10: Graph showing the rate of decrease in diameter of an evaporating 50 µm droplet.

Figure 5.11 plots the times taken for a range of smaller sized droplets to decrease their mass by 10% due to vaporization alone, and also the time taken for these droplets to completely disintegrate due to breakup predicted by the TAB model. The initial displacement, velocity, and temperature of these droplets are representative of the droplets emitted by the wave breakup model. As the results suggest, for a 10 µm droplet the evaporation time far exceeds the break up time. As the droplet size is decreased these timescales become more comparable. When the droplet diameter is between 2.5 and 3 µm the breakup time increases rapidly. Within this small size range vaporization suddenly becomes the main driving force for the droplet disintegration.

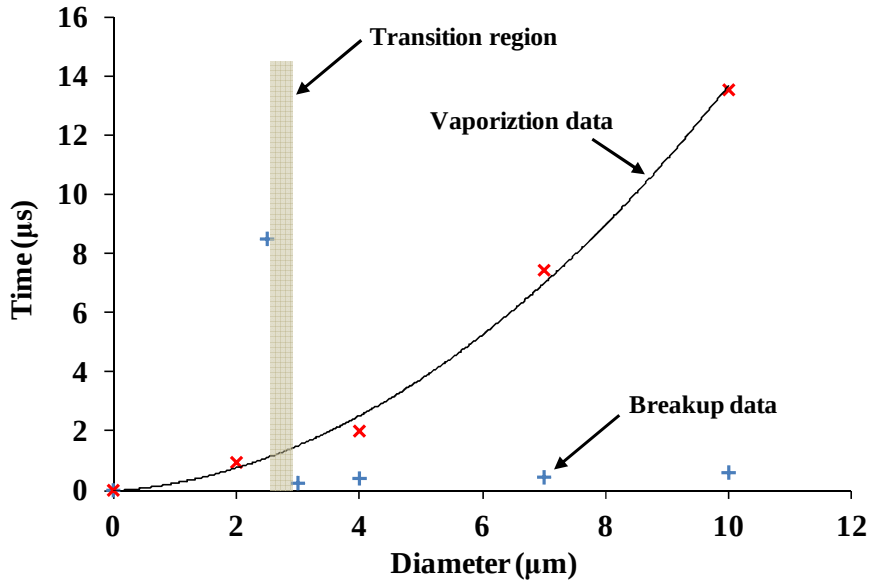

Figure 5.11: Time taken for various sized droplets to either breakup or for their mass to decrease by ten percent of their original mass due to vaporization.

In Figure 5.12, the breakup simulation results are presented alongside several different experimental observations showing a good level of agreement in all cases. Figure 5.12a compares the non-dimension child droplet sizes (d/D_0) with the initial parent droplet We. The experimental observations are taken from (Wolfe & Anderson 1964, Lane et al. 1949, Lane 1951, Lane & Dorman 1952) and the simulation points plotted include all tested particle sizes from 500 μm down to 2.5 μm. Figure 5.12b compares the dimensionless time taken to initiate breakup for particles with varying We, where the experimental observations are from (Wolfe & Anderson 1964) and the four simulation points plotted represent the dimensionless times for droplet sizes: 10, 7, 4 and 3 μm. The 2.5 μm droplet requires a dimensionless time of 60.0 for breakup to initialize, and therefore resides outside the plotted region. Finally, Figure 5.12c plots experimentally measured (Haas 1964) critical Weber number We_{crit} against the droplet Ohnesorge number. These results are compared to the simulation breakup of the small droplets: 10, 7, 4, 3 and 2.5 μm.

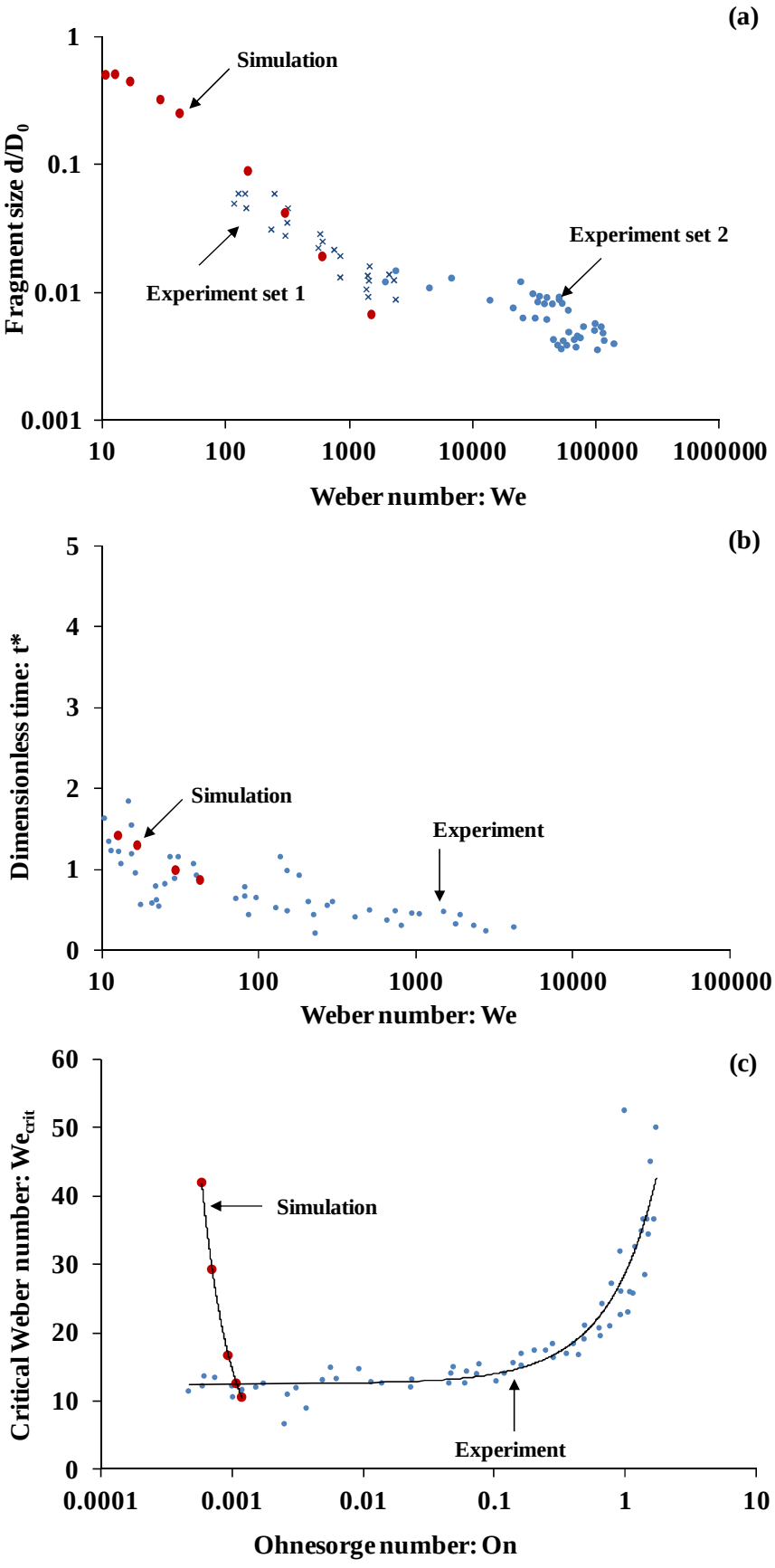

Figure 5.12: Comparisons between simulations and experimental observation: Time to initiate break up (a), child droplet sizes (b) and the critical We (c)

As Figure 5.12a illustrates, the child droplet sizes predicted by the wave breakup model are in close agreement with the experimental observations. While TAB breakup simulation results lie outside the experimental data range, their sizes follow a logical trend alongside the Wave Breakup Model. As exhibited, a maximum dimensionless child droplet size ratio exists in the region of the 2.5 μm and 3 μm parent droplets, with corresponding We of 10.5 and 12.6 respectively. Figure 5.12b illustrates how the time required to initiate breakup as predicted by the TAB model increases continuously with decreasing We number. For droplets below 3 μm and We less than 12.6 this time rapidly increases. Both the experimental and simulation results presented in Figure 5.12c are in agreement with Figure 5.12b, indicating that when the droplet size is reduced below 2.5 μm We falls below We_{crit} of roughly 12, resulting in exponential increases in breakup initiation times.

It is evident that the disintegration process of a water droplet between 50 μm and 500 μm injected into a HVOF-type system is dependant on both aerodynamic breakup and vaporization to varying degrees; and depends on the droplet fragmentation sizes produced. The respective mass-weighted average diameters of the primary child droplets shed from the 50 μm, 100 μm, 200 μm, and 500 μm parent droplets are: 4.403, 4.149, 3.798, and 3.342. The transition region highlighted in Figure 5.11 marks the region in which the vaporization mode becomes the dominant form of disintegration process. Looking back at Figure 5.9b, for a 200 μm parent droplet the smallest primary child droplets are close to the transition boundary, while for a 500 μm parent droplet roughly half of the primary child droplets reside within the transition zone. As a result, for an initial parent droplet smaller than 200 μm, the disintegration process for its primary child droplets is governed by breakup only. The resulting secondary child droplets then vaporize without breakup. For an initial parent droplet greater than 200 μm, the disintegration process for its primary child droplets may follow one of two routes. For the child droplets larger than 3 μm, disintegration is governed by aerodynamic breakup only, and then vaporization. For the droplets between 2.5 μm and 3 μm, disintegration is driven simultaneously by both vaporization and aerodynamic breakup. These investigated droplet disintegration regimes are finally summarized schematically in Figure 5.13.

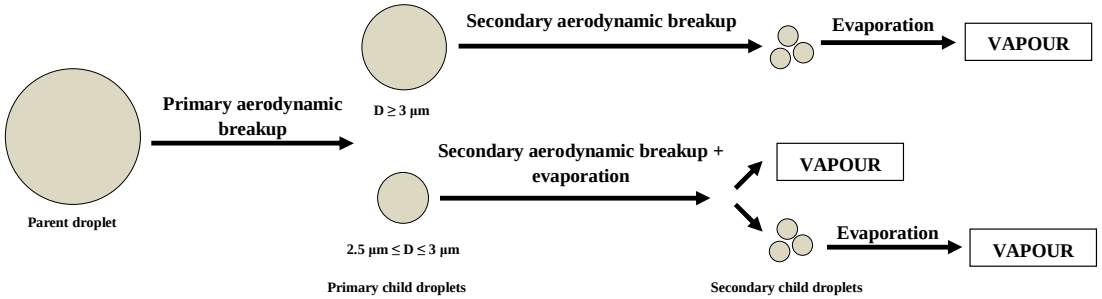

Figure 5.13: Path diagram showing the different water droplet disintegration routes when injected into a HVOF jet

The characterised disintegration process may be controlled to some extent, by the pre determined properties of the solution or suspensions being sprayed, and by doing so, the deposition process can be optimised for the spray method at hand.

For instance, fragmentation of the feedstock depends on the Weber (We) and Ohnesorge (Oh) numbers and can be tailored by adjusting the liquid viscosity. For example, in liquid precursor thermal spraying it has been shown that changing the moles of 7 wt.% yttria-stabilized zirconia from 0.6 moles to 2.4 moles raises the solution viscosity from 0.0014 to 0.007 Pa S (Chen at al., 2008). For suspensions, certain additives such as polyvinyl alcohol can be used to increase the suspension viscosity (Rampon et al. 2006, Rampon et al. 2008). The suspension solid volume fraction and particle size distribution influences the suspension viscosity, but to a less extent, and can be expected to raise the viscosity by no more than 50% (Roscoe 1952, Nguyen et al. 2008).

In general, the fundamental understanding of liquid feedstock thermal spraying is still in its infancy and the optimum feedstock configurations such as concentrations of solid particles, additives, dispersants, and precursor solutions, as well as the particle size and size distributions, and type of solvent used for different deposited materials and for different processing methods are not yet fully determined. Furthermore, the levels of experimental data trends for estimating the thermophysical properties such as viscosity, surface tension, specific heat capacity, and thermal conductivity during the complete liquid disintegration process are limited. The results presented serve as a baseline study for liquid feedstock injection by using detailed water properties to study the liquid droplet disintegration process. The insight gained from the study is a useful step forward in the understanding and ongoing developments of liquid feedstocks in thermal spraying.

5.4 Conclusion

The disintegration process of water droplets between 50 μm and 500 μm entering a HVOF-type system are simulated and the breakup time scales and droplet sizes compare well to experimental observations. The results obtained indicate that the droplet disintegration process is dependent on the initial parent droplet sizes. An initial parent droplet between 50 μm and 200 μm in size will breakup, forming droplets which then vaporize only. For a parent droplet between 200 μm and 500 μm, a fraction of the child droplets will undergo vaporization only, and a fraction will undergo further breakup and simultaneous vaporization.

5.5 Chapter nomenclature

General symbols

A_p	Surface area of a particle
A_0	Constant in realizable k-ε model (4.04)
A_s	Constant in eddy dissipation model (4.0)
a	Decreasing parent droplet radius
B_0	Wave breakup model constant
B_1	Wave breakup model constant
C_1	Constant for the linear pressure strain model (1.8)
$C_{1\square}$	Constant for the turbulent dissipation of energy (1.44)
C_2	Constant for the linear pressure strain model (0.6)
$C_{2\square}$	Constant for the turbulent dissipation of energy (1.92)
C_D	Drag coefficient
C_p	Specific heat capacity at constant pressure
C_b	TAB model constant (0.5)
C_d	TAB model constant (5)
C_F	TAB model constant (1/3)
C_k	TAB model constant (8)
d_p	Particle diameter
$D_{i,m}$	Diffusion coefficient of water vapour in the bulk flow
E	Total energy
F	Additional force term
G_b	Generation of turbulence energy due to buoyancy

G_k	Generation of turbulence energy due to mean velocity gradients
h	Convective heat transfer coefficient
h_{fg}	Enthalpy of vaporization
K	Thermal conductivity
k	Turbulent kinetic energy
k_c	Mass transfer coefficient
m	Mass
M	Mach number
$M_{□,i}$	Molecular weight of species i
N_i	Molar flux of vapour
Nu	Nusselt number
Oh	Ohnesorge number
P	Pressure
Pr	Prandtl number
P_{sat}	Saturated pressure
r	Radial distance from centreline
r_p	Particle radius
r_{32}	Sauter mean radius of the droplet size distribution
$R_{i,r}$	Net rate of production of species i due to reaction r
R	Universal gas constant
Re	Reynolds number
S	Molecular speed ratio
Sc	Schmidt number
S_m	Mass source term
Ta	Taylor number
t	Time
T	Temperature
u_p	Particle velocity
v	Gas phase velocity
v_{rel}	Relative velocity magnitude between the gas phase and discrete droplet
$v'_{i,r}$	stoichiometric coefficient for reactant i in reaction r
$v''_{j,r}$	stoichiometric coefficient for product i in reaction r

We	Weber number
X_i	Local bulk mole fraction
Y	Local bulk mass fraction
y	Non dimensional distortion
Y_M	Contribution of the fluctuating dilatation in compressible turbulence to dissipation rate
Z	Ratio of total energy in distortion and oscillation to the energy in the fundamental mode

Greek symbols

ε	Turbulent kinetic energy dissipation rate
μ	Dynamic viscosity
ρ	Density
σ	Particle surface tension
Λ	Wavelength of most unstable wave on droplet surface
τ_p	Particle breakup time
Ω	Maximum growth rate for the droplet surface instability waves
υ	Kinematic viscosity
σ_k	Turbulent Prandtl number for k
σ_ε	Turbulent Prandtl number for ε

Subscripts

eff	Sum of the physical and turbulent values
i	Refering to one of many species
p	Particle
r	Radial coordinate direction
R	Reactant
t	Thermophoretic
x	Axial coordinate direction
∞	Free stream conditions

Mathematical operators

∂	Partial differential

∇	Del operator
Δ	Difference between two quantities of a variable
$\vec{v}$	Vector form of variable
$\dot{v}$	Time derivative
$\ddot{v}$	Double time derivative

6 Molten metallic droplet impingement

A fundamental understanding of the splat formation can pave the way for future developments in thermal spray technology. Numerical modelling is applied in this investigation which simulates the detailed transient flow of a molten metal droplet impacting, deforming, and solidifying on a flat, solid substrate. The computations are carried out on a fixed Eularian structured mesh using a volume of fluid method to simulate the boundary between the metallic and atmospheric-gas phases. The results shed light on the break-up phenomena on impact and describe in detail how the solidification process varies with an increasing impact velocity.

6.1 Chapter introduction

This close-up stage of the modelling process involves the simulation of particle impingement. To date, the simulations of fully molten droplet impingements have improved the understanding of particle deformation in thermal spraying, and have been recently reviewed by Chandra & Fauchais (2009). At present the latest models are capable of describing several physical phenomena which arise during the process of molten droplet impingement and their modelling strategies are outlined as follows.

Computational fluid dynamics (CFD) based volume of fluid method (VOF) is utilized in almost all cases to track the deforming surface of a single molten droplet (Ivosevic et al. 2006, Kamnis & Gu 2005, Ahmed & Rangel 2002, Bussmann et al. 1999). The fluid surface tension force at the boundary between the droplet and the surrounding gas is included as a body force in the momentum conservation equation (Kamnis & Gu 2005, Bussmann et al. 1999). The solidification process has been equated using different methods. The decrease in velocity due to solidification may be mathematically described by introducing a sink term within the momentum conservation equation (Kamnis & Gu 2005). Alternatively, a fixed velocity method is adopted by Pasandideh-Fard et al. (1998), whereby the velocity vector within the momentum conservation equation is directly multiplied by the liquid phase fraction within the associated computational cell. Hence, if the cell is fully solid then the contents of the cell are stationary. During both of these solidification methods an enthalpy formulation takes into account the combined sensible enthalpy and the latent heat of solidification, which completes the energy equation and allows prediction of the temperature profile through the impinging droplet. The investigations found in (Kamnis & Gu 2005, Ahmed & Rangel 2002, Pasandideh-Fard et al. 1998) couple the heat energy transfer between the droplet and the substrate which is shown to play a vital role in simulating the splat morphology by controlling the rate of cooling and

solidification. The more advanced computational models include a thermal contact resistance (Kamnis & Gu, 2005), which is physically created by air enclosed within the roughness of the substrate and acts as a resistance to the coupled heat transfer process.

Validation of these models has highlighted their ability to successfully predict the rate of spreading and solidification of a single molten droplet impingement (Kamnis & Gu 2005, M. Pasandideh-Fard at al. 1998) with the correct number of fingers surrounding the splat in three dimensions (Kamnis et al. 2008b). Recent image based validations have been targeted towards simulating more than one droplet and with the inclusion of uneven substrate surfaces, which also compare extremely well alongside state of the art photographic imaging (Ghafouri-Azar et al. 2004, Ghafouri-Azar et al. 2005, M. Pasandideh-Fard at al. 2002a).

This study builds upon previous studies by closely examining the impingement process during impact and solidification. The work sheds light on the interaction between the molten metal droplet and the ambient air during its initial stages of impact. Additionally, the work demonstrates for the first time that modelling using the CFD methods can produce high levels of detail at the particle/substrate interface, which can be utilised in the future to explain mechanical bonding structures. The impact velocity in this investigation is increased to bridge the gap between the previous low velocity simulations and the realistic velocities found during thermal spraying.

6.2 Summary of numerical methods

A 2.2 mm molten tin (Sn) particle at an initial uniform temperature of 519 K is simulated to impact onto a flat, stainless steel substrate at a temperature of 298 K. The simulated droplet impact velocities are: 4 ms^{-1}, 10 ms^{-1}, 100 ms^{-1} and 400 ms^{-1}. The Biot number (Bi) of the spherical droplet can be estimated by calculating the convective heat transfer coefficient at the surface of the droplet using the correlation by Ranz & Marshall (1952a, 1952b) as outlined in Equation 6.1. The values of the Bi number for the molten droplet travelling through air at atmospheric condition are given in Table 6.1, along with the constituent values of Nu, Re and Pr. The Bi numbers for all scenarios are well below unity and therefore indicate that a uniform temperature distribution through the droplet is a realistic assumption.

$$Nu = 2 + 0.6Re_g^{\frac{1}{2}}Pr^{\frac{1}{3}} \quad (6.1)$$

	4 ms^{-1}	10 ms^{-1}	100 ms^{-1}	400 ms^{-1}
Nu	15.345	23.101	68.727	135.454
Re_g	602.000	1506.091	15060.914	60243.657
Pr	0.744	0.744	0.744	0.744
Bi	0.011	0.017	0.050	0.098

Table 6.1: Values of Nu, Re, Pr and Bi for a 2.2 mm molten tin droplet at a temperature of 519 K travelling through air under standard atmospheric condition.

The dimensions for the axisymmetric domain are provided in Figure 6.1, including the initial particle-substrate separation distance. The 2D axisymmetric domain consists of 240,000 structured computational cells and a refined grid is utilized at the substrate surface. The flow and thermal modelling approach is outlined below.

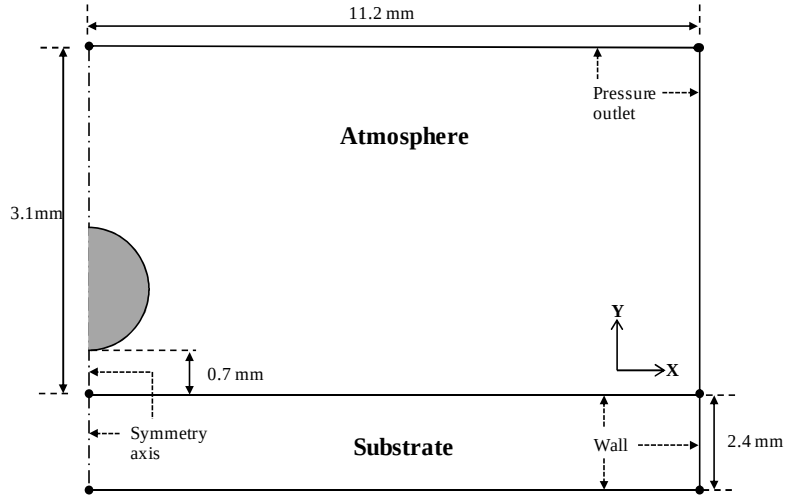

Figure 6.1: Schematic diagram of the axisymmetric computational domain for the simulated impingement of a 2.2mm molten tin droplet.

6.2.1 Flow model

The VOF model is used to track the droplet and air as two immiscible fluids by solving a single set of momentum equations. This method is carried out by tracking the volume fraction of each of the fluids throughout the computational domain. The Compressive Interface Capturing Scheme (CICSAM) by Ubbink & Issa (1999) is applied

as the discretization scheme due to its suitability for flows with high viscosity ratios between the immiscible phases.

The tracking of the interface between the gas phase and molten droplet phase is based on the volume fraction continuity equation, as given by Equation 6.2, where *v* is the velocity, *ρ* is the density, *α* is the volume fraction and *t* is the time. The subscript *q* implies one of the phases. For the surrounding air, which is treated as the primary phase, the volume fraction is computed using the constraint shown in Equation 6.3, where *n* is the number of phases and is equal to 2. The density *ρ* and viscosity *μ* within each computational cell are calculated based on the volume fraction of each phase, as in Equations 6.4 and 6.5, where the subscripts *1* and *2* represent the primary and secondary phases respectively.

$$\frac{1}{\rho_q}\left[\frac{\partial}{\partial t}\left(\alpha_q \rho_q\right) + \nabla \cdot \left(\alpha_q \rho_q \vec{v}_q\right)\right] = 0 \tag{6.2}$$

$$\sum_{i=1}^{n} \alpha_i = 1 \tag{6.3}$$

$$\rho = \alpha_2 \rho_2 + (1 - \alpha_2)\rho_1 \tag{6.4}$$

$$\mu = \alpha_2 \mu_2 + (1 - \alpha_2)\mu_1 \tag{6.5}$$

The volume-fraction-averaged material properties are then applied in the momentum and energy conservation equations and are given in Equation 6.6 and 6.7, where *g* is the gravitational acceleration, *H* is the total heat, *k* is the thermal conductivity, *p* is the pressure, and *T* is the temperature. The resulting velocity and energy fields are therefore shared between the two phases.

$$\frac{\partial}{\partial t}(\rho \vec{v}) + \nabla \cdot (\rho \vec{v} \vec{v}) = -\nabla p + \nabla \cdot [\mu(\nabla \vec{v} + \nabla \vec{v}^T] + \rho \vec{g} + F_{vol} + S \tag{6.6}$$

$$\frac{\partial}{\partial t}(\rho H) + \nabla \cdot (\rho \vec{v} H) = \nabla \cdot (k \nabla T) \tag{6.7}$$

The continuum surface tension force, F_{vol}, is calculated by the method of Brackbill et al. (1992) using the fluid densities at the interface and the droplet surface tension. Its value appears on the right-hand-side of the momentum equation as a source term. The methods of Brackbill et al. are also utilized to predict the curvature of the droplet surface close to the wall using the computed tangential and normal flow velocity components along the wall, and the contact angle of the droplet at the substrate surface (Brackbill et al. 1992).

It is important to specify accurately the contact angle between the droplet and substrate when conducting such simulations, which is difficult without appropriate experimental observations. The simulation set up in this instance is selected based on the fact that detailed experimental results are available. Hence, the contact angles are obtained from the measured results of Aziz & Chandra (2000). In this instance an initial angle of 70° is introduced and the dimensionless transition time t^* (as defined in the table of dimensionless numbers in the appendix of this chapter) from 70° to 140° is calculated to be 0.07. A sensitivity test was also conducted whereby the contact angle was set to a constant 90 degrees. While this value is not significantly different to the experimentally measured value, a final spread factor difference between the accurately calibrated and the constant value case of almost 20% was found. The droplet spread factors for both simulation cases are plotted in Figure 6.3.

Many mathematical techniques have been developed to numerically solve moving boundary problems, and a good review of these techniques is given by Crank (1984). The majority of these reviewed methods are conduction based heat transfer problems without convection. One method of solving the moving liquid-solid interface is by applying a deforming grid. However, simpler fixed grid solutions of convection-diffusion phase change problems are numerically more efficient, flexible and better suited to more complex problems such as the case of molten droplet impingement (Voller et al. 1990).

The fixed-grid enthalpy-porosity technique is applied in this chapter to model the solidification/melting process of the tin droplet, whereby the liquid fraction of each computational cell volume is computed. The liquid fraction is computed at each iteration step, based on an enthalpy balance, as described within the following chapter section. A mushy zone is defined as a region where the liquid fraction lies between 0 and 1, and is taken as a "pseudo" porous medium. The porosity is equal to the liquid fraction within an individual cell. Hence, a fully solidified region has no porosity, which reduces the cell velocity to equal 0. The porosity function applied, known as the Darcy Law (Equation 6.8), acts as a sink term (S) within the momentum equation (see Equation 6.6 for the momentum equation). The solidifying liquid incurs a decrease in momentum until the droplet becomes stationary due to complete solidification. Where, A_{mush} is the mushy constant, β is the liquid fraction and χ is a constant equal to 0.001. The directional velocity vector is represented by $\vec{v}$, and is set according to the direction of the momentum equation being solved. Further details of the enthalpy-porosity method are given in Voller and Prakash (1987).

$$S = \frac{(1-\beta)^2}{(\beta^3+\chi)} A_{mush} \vec{v} \tag{6.8}$$

6.2.2 Thermal model

The particle is initialized with a uniform temperature of 519 K. An enthalpy balance is used in order to calculate the liquid fraction of solid and liquid within a computational cell during the solidification of the droplet. The total enthalpy of the material, H, is calculated as the sum of the sensible enthalpy, h, and latent heat, ΔH, as given in Equation 6.9. A computational cell may reach a temperature which lies between the solidus and liquidus temperatures. Within this region the material is said to be within its mushy state, consisting of both solid and liquid phases. The liquid fraction within the mushy region is termed β and L is the latent heat when in liquid phase.

$$H = h + \Delta H \tag{6.9}$$

where,

$$h = h_{ref} + \int_{T_{ref}}^{T} C_p dT \tag{6.10}$$

$$\Delta H = \beta L \tag{6.11}$$

As the temperature increases or decreases during the transition between liquid and solid, the latent heat is either absorbed or dissipated respectively. This change in temperature determines the fractional change in liquid concentration. The calculation of temperature is therefore achieved by a sub-iteration to match the total enthalpy from the energy equation (Equation 6.7) with the combined values of sensible enthalpy and latent heat (Equation 6.9) as outlined in Figure 6.2. The latent heat source term is a function of the volumetric solid fraction, which in turn is a function of temperature. For the applied approach a linear relationship is assumed (See Equations 6.11 and 6.12). For many real systems the solid fraction-temperature relationship will not take such a simple form, such as for binary alloys. However, for pure tin this approach is deemed appropriate.

$$\beta = 0 \; if \; T < T_{solidus} \tag{6.12}$$

$$\beta = 1 \; if \; T > T_{liquidus}$$

$$\beta = \frac{T - T_{solidus}}{T_{liquidus} - T_{solidus}} \; if \; T_{solidus} < T < T_{liquidus}$$

The heat transfer process through the substrate is by conduction. In reality air is entrapped within the roughness of the material surface which acts as thermal resistance. The model takes into account the air entrapment by applying a thermal resistance to the flow of heat energy to the substrate. A value of 1.8×10^{-6} m^2 K W^{-1} for

the thermal contact resistance is applied which corresponds to a stainless steel substrate roughness of 0.06 μm (Shakeri & Chandra 2002). The droplet and substrate material properties are summarized in Table 6.2.

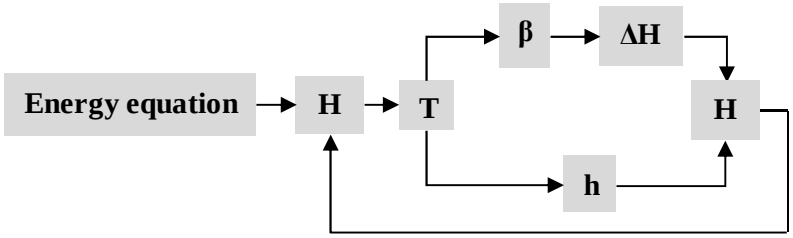

Figure 6.2: Iterative enthalpy formulation during phase transition, including the latent heat of solidification.

Impinging droplet material	Tin (Sn)
Substrate material	Stainless Steel (SS)
Droplet initial temperature	519 K
Substrate initial temperature	298 K
Solidus temperature (Sn)	504 K
Liquidus temperature (Sn)	506 K
Thermal conductivity (liquid Sn)	33.6 W (m K)$^{-1}$
Thermal conductivity (solid Sn)	62.2 W (m K)$^{-1}$
Thermal conductivity (SS)	14.9 W (m K)$^{-1}$
Density (liquid Sn)	6980 kg (m)$^{-3}$
Density (solid Sn)	7200 kg (m)$^{-3}$
Density (SS)	7900 kg (m)$^{-3}$
Droplet surface tension	0.566 N (m)$^{-1}$
Specific heat capacity (Sn)	244 J (kg K)$^{-1}$
Specific heat capacity (SS)	477 J (kg K)$^{-1}$
Latent heat of solidification	58500 J (kg)$^{-1}$

Table 6.2: Material properties for the simulation of a tin droplet impinging onto a stainless steel substrate.

6.3 Results and discussion

6.3.1 Experimental comparisons and background

The variation in spread factor (D/D_0) with time of the simulated particle is plotted alongside experimental measurements in Figure 6.3. The experimental results are of the same scenario, whereby a 2.2 mm Sn droplet at 519 K impacts at a velocity of 4 ms^{-1} on a substrate of 0.06 μm roughness (Shakeri & Chandra 2002). The results show a good level of concordance during all stages of spreading, retardation, and recoil. The final splat diameter of the modelled droplet and the experimental image are also physically similar as compared in Figure 6.4, with a thin, uneven central surface and thick, solidified rim around the outside edge.

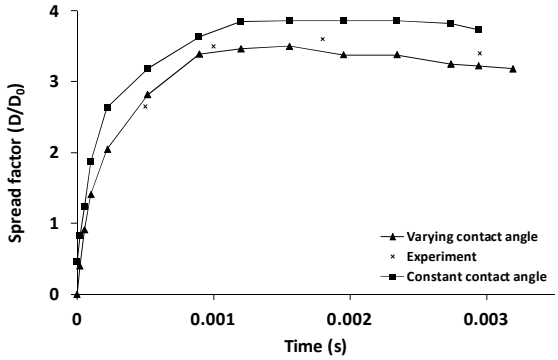

Figure 6.3: Comparison of simulated and experimentally measured (Shakeri & Chandra, 2002) spread factors for a molten tin droplet impinging at 4 ms^{-1} and initial temperature of 519K onto a stainless steel substrate at an initial temperature of 298K.

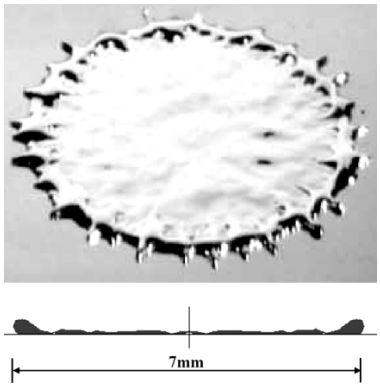

Figure 6.4: Physical comparison between simulated and experimental splat shape for an impact velocity of 4 ms^{-1} (Shakeri & Chandra, 2002).

The transient motion of the simulated droplet impacting at 4 ms^{-1} is depicted in Figure 6.5 showing a good likeness to previous numerical simulations. The particle impinges onto the surface, where it deforms and begins to spread outwards. The molten material then begins to slow and cool due to heat transfer to the substrate. Solidification and retardation at the periphery of the splat creates matter to be ejected, as shown in Figure 6.5. Several experimental and numerical studies have commented on this process of matter ejection (Chandra & Fauchais 2009, Kamnis & Gu 2005, Mostaghimi et al. 2002, Pasandideh-Fard et al. 2002b, Fukumoto & Huang 1999) and a later study in Chapter 7 (Tabbara & Gu 2011) characterises this process in detail.

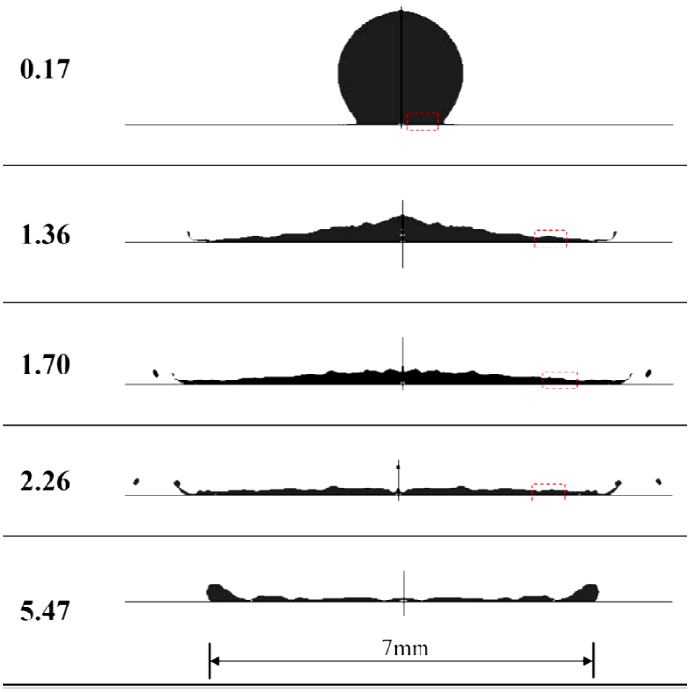

Figure 6.5: Development of the splat formation with an impingement velocity of 4 ms^{-1}.

6.3.2 Spreading

Figure 6.6 plots the variation of spread factor with dimensionless time, t*, for the simulated 2.2 mm droplet impinging at 4, 10, 100 and 400 ms^{-1}. The values of droplet Weber number (We) and droplet Reynolds number (Re_d) are listed in Table 6.3, and greatly exceed unity in all cases. This information indicates that both the surface tension and viscous forces play a negligible role in controlling the motion of the droplet at the time of impact compared to the inertial forces.

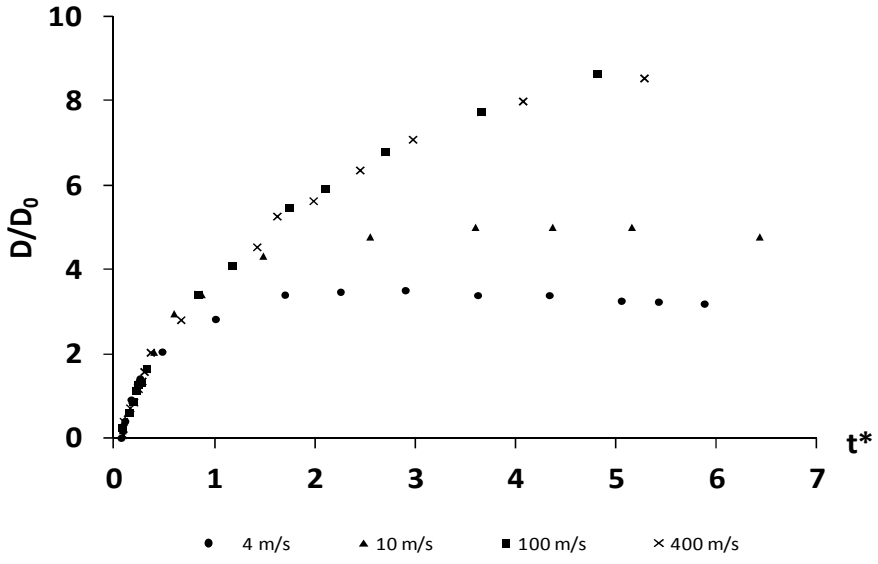

Figure 6.6: Comparison of droplet spread factors with increasing impact velocity.

Dimensionless parameter	4 ms^{-1}	10 ms^{-1}	100 ms^{-1}	400 ms^{-1}
Re_d	27920	69800	698000	2792000
We	434.0	2713	271307	4340918
Pe	1.892	4.73	47.3	189.2

Table 6.3: Dimensionless numbers for a 2.2 mm molten tin droplet at a temperature of 519 K travelling through air at standard temperature and pressure.

When impacting at 4 ms^{-1} the droplet reaches its maximum splat diameter after roughly 0.002 s. The modelled spat of a droplet impacting at 10 ms^{-1} is given in Figure 6.7, revealing a thinner, more even internal surface and smaller sized rim when compared to the 4 ms^{-1} droplet.

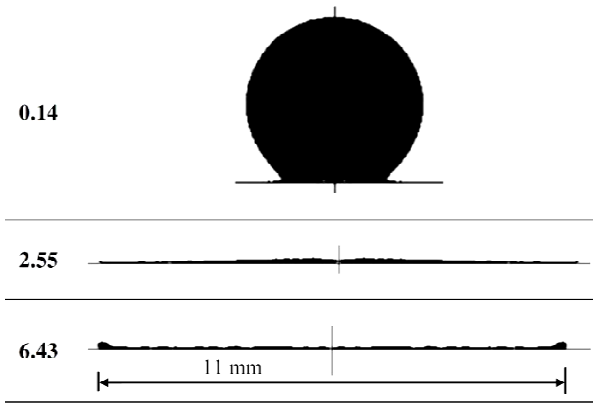

Figure 6.7: Splat formation with an impingement velocity of 10 ms^{-1}.

The solidification and spreading kinetics are linked by the droplet Peclet number (Pe). If Pe greatly exceeds unity then one can assume the spreading rate is far greater than the heat conduction and solidification, and therefore solidification bears a negligible effect on the final splat shape. This is demonstrated by the simulation of the Sn droplet impacting at 100 ms^{-1} and 400 ms^{-1}. For these higher velocity impingements, Pe is equal to 47 and 189 respectively, and the splat spreads to the outside edge of the computational domain in a short space of time. During this period, solidification has made little affect on the spreading kinetics and is controlled by the droplet momentum. For this reason the spread factor variation against dimensionless time is simulated to be almost identical for an impacting droplet at 100 ms^{-1} and 400 ms^{-1}, as depicted in Figure 6.6, implying that during this period both droplets exhibit the same overall impact characteristics, but at a different rates.

6.3.3 Impact phenomena

This section investigates the impacting droplet flow and break-up phenomena around the initial impact zone during the early stages of impingement. The simulations indicate that the droplet break-up around the initial impact zone at an impact velocity of up to 10 ms^{-1} is negligible. However, when the velocity is increased to 100 ms^{-1} the Rayleigh-Taylor instabilities form at the droplet-air interface due to the increased air resistance against the flow of the droplet, producing an uneven surface boundary. As the magnitude of these perturbations grows the molten liquid, by virtue of its surface tension, minimizes its surface by creating small fragmented droplets, as exhibited in Figures 6.8a and 6.8b. The vorticies at the edge of the impinging droplet further destabilize the surface and are strengthened with higher impact velocities.

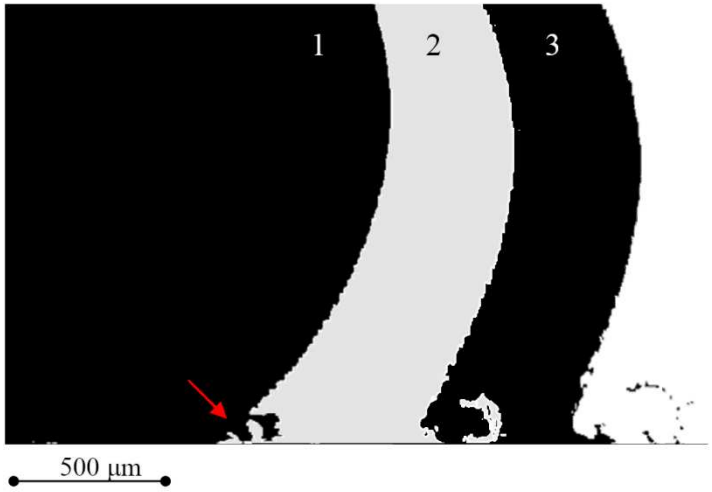

a) $t_1^* = 0.15, t_2^* = 0.20, t_3^* = 0.22$

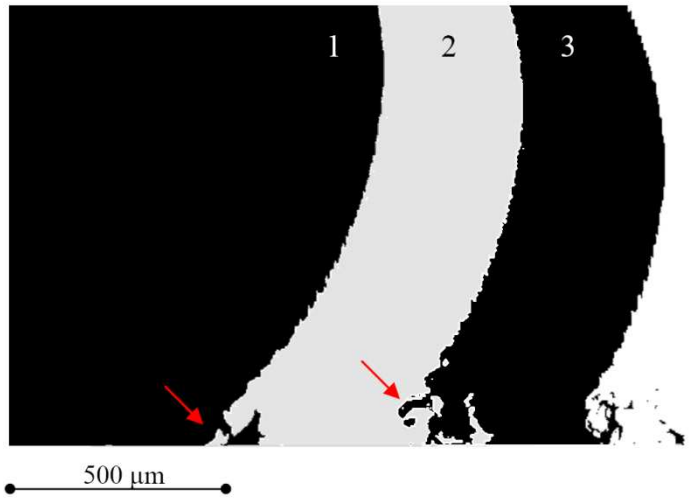

b) $t_1^* = 0.15, t_2^* = 0.19, t_3^* = 0.21$

Figure 6.8: The process of droplet break-up on impact at a) 100 ms^{-1} and b) 400 ms^{-1} with air entrapments indicted by the arrows.

At high impact velocities of 100 ms^{-1} and 400 ms^{-1} the air is entrapped within the particle through the underside of the droplet on impact and by penetration of the vortex at the outside surface, as shown in Figure 6.8. The entrapped gas is then forced outwards due to the spreading of the droplet and higher pressure at the centre of the impact zone. Together the Rayleigh-Taylor instabilities and the air entrapment cause shedding of small particles on impact. Figure 6.8 also highlights how by increasing the velocity from 100 to 400 ms^{-1} the molten droplet is woven inwards creating larger pores.

6.3.4 Solidification process

The transient impact morphology of the 2.2 mm Sn particle impacting at 4 ms^{-1} is exhibited in Figure 6.5, and the process of solidification within the highlighted zones are depicted in Figure 6.9. At $t^* = 0.17$ (9.42×10^{-5} s) planar solidification begins, producing a smooth level sheet of solidified Sn at the substrate surface. At $t^* = 1.36$ (7.47×10^{-4} s) the solidified Sn begins to build up unevenly and by $t^* = 1.7$ (9.36×10^{-4} s) the peaks of solidified Sn reach their maximum amplitude of roughly 15 μm. A wave like process is then initiated whereby the liquid material is woven inwards as it solidifies, as depicted in Figure 6.9. The molten fluid vorticities produced are known as Kelvin-Helmholtz instabilities and occur due to velocity shearing. This folding phenomenon was hypothesised to occur at the substrate surface of thermal spray coatings by G. Grujicic et al. (2003) and has been recently observed in thermal spraying when carrying out TEM scans of a final coating cross section (Brossard et al. 2010). These TEM scans show that the particles melt the substrate surface on impact and mechanical interlocking (also known as mechanical keying) occurs. This mechanical interlocking has been documented to chiefly determine the adhesion strength of a coating to the substrate in thermal spray coatings (Sobolev et al. 1997).

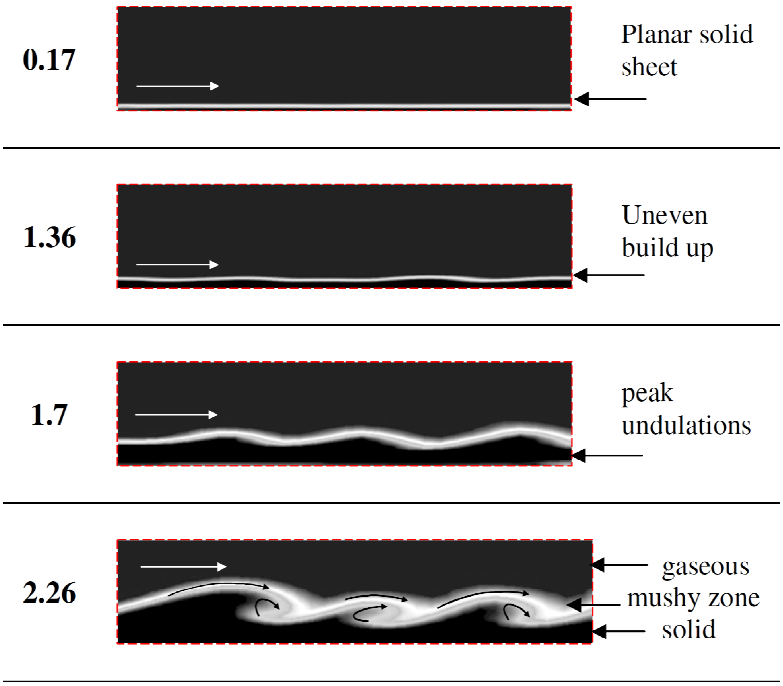

Figure 6.9: Simulated solidification process with an impingement velocity of 4 ms^{-1}. Sections taken from highlighted zones in figure 6.5. The white arrows show the direction of spreading.

In this case, for the impinging 10 ms^{-1} particle the size of the undulating peaks are found to be too shallow to produce wave mixing because of its higher Pe. As a result the molten droplet does not solidify rapidly enough to create solid peaks with amplitude great enough to induce wave-like mixing. The results of this case indicate that beyond 100 ms^{-1} the rate of spreading occurs so rapidly that conduction of heat becomes negligible. As a result at an impact of 100 ms^{-1} and 400 ms^{-1} little or no solidification is observed and the splat film spreads to the edge of the computational domain.

6.4 Conclusion

The simulation results for a 2.2 mm tin droplet at 519 K and impact velocity of 4, 10, 100 and 400 ms^{-1}. The simulated splat formation of a droplet impacting at 10 ms^{-1} reveals a thinner, more even internal surface and smaller sized rim when compared to the 4 ms^{-1} droplet. For the higher velocity impingements the splat spreads to the outside edge of the computational domain in a short space of time and the extent of solidification is negligible.

The simulations indicate that for a 2.2 mm Sn droplet at 519 K little or no fragmentation will occur around the initial impact zone at impact velocities of up to 10 ms^{-1}. When the impact velocity is increased to 100 ms^{-1} fine fragmented droplets are

produced. With an impact velocity of 400 ms^{-1} the droplet is woven inwards creating large pores.

The solidification process may consist of up to three stages: planar solidification; uneven solidification and wave mixing. The detailed development of the solidifying splat morphology presented in this study highlights the potential of this computational method to be capable of modelling mechanical interlocking structures. Future modelling work can now focus on the detailed interaction of more than one micron sized droplet and a melted substrate surface so that a deeper understanding of the mechanical bonding structure at the substrate can be established.

6.5 Chapter nomenclature

General symbols

C_p	Specific heat capacity at constant pressure
D_0	initial particle diameter
g	gravitational acceleration
h_c	convective heat transfer coefficient between the droplet and atmosphere
h	sensible heat
H	total heat
ΔH	latent heat content
k	thermal conductivity
L	Latent heat when in liquid phase
t	time
T	temperature
V_0	initial particle velocity
v	velocity

Greek symbols

α	thermal diffusivity
β	liquid fraction
μ	viscosity
σ	surface tension
ρ	density

Dimensionless numbers

Biot number	$Bi = \frac{h_c D_0}{k_d}$
Nusselt number	$Nu = \frac{h_c D_0}{k_g} = 2 + 0.6 Re^{1/2} Pr^{1/3}$
Peclet number	$Pe = \frac{t_c}{t_s} = \frac{D_0 V_0}{\alpha}$
Prandtl number	$Pr = \frac{C_p \mu_g}{k_g}$
Reynolds number	$Re_g = \frac{\rho_g V_0 D_0}{\mu_g}$ or $Re_d = \frac{\rho_d V_0 D_0}{\mu_d}$
Time	$t^* = \frac{V_0 t}{D_0}$
Weber number	$We = \frac{\rho_d V_0^2 D_0}{\sigma}$

Subscript symbols

d	droplet
g	atmospheric gas
p	primary phase
q	one of several phases
w	wall
∞	bulk region

7 Partially molten droplet impingement

Due to the low thermal conductivity of ceramics large temperature gradients are present through the powder particles during plasma spray deposition. As a result the particles often impinge at the substrate in a semi-molten form. This in turn substantially affects the final characteristics of the coating being formed. This study is dedicated to the novel modelling development and simulation of a semi-molten droplet impingement. The study examines the impingement process during impact, spreading and solidification of semi-molten zirconia. The simulation provides an insight to the heat transfer process during impact and solidification of a semi-molten powder particle and illustrates the freezing-induced break-up mechanism at the splat periphery.

7.1 Chapter introduction

Thermal spray technology encompasses several processes which are used to create coatings for a variety of different applications. Plasma spraying in particular is characterized by extremely high process temperatures of roughly 6000 to 15,000 °C (Davies, 2004) and is commonly utilized to deposit oxide ceramics such as zirconia (ZrO_2) in the size range of 20–90μm (Pawlowski, 2008b). However, due to the high plasma temperature and low thermal conductivity of the ceramic powders, these particles often impinge at the substrate in a semi-molten form. A good overview of modelling arc plasma spray processes can be found in (Trelles et al. 2009).

The most developed finite element simulations for un-melted, solid particle impingements can be found in (W. Y. Li at al. 2009, W. Y. Li & Gao 2009) for copper powder deposited by cold spray, and in (Kamnis & Gu 2010, Gu & Kamnis 2009, Kamnis et al. 2009) for tungsten-carbide cobalt (WC-Co) powder deposited by HVOF combustion spray. The modelling developments for fully-molten, metallic droplets are well reviewed by Chandra & Fauchais (2009). The most effective and current modelling strategies for the impingement of fully-molten droplets are summarized in Chapter 6.

Despite the lack of detailed understanding for the deposition of semi-molten droplet impingement, little modelling and simulation effort has been targeted towards its case due to the difficulties which arise when trying to model both solid and liquid phases. A rule-based approach by Shi & Christophides (2004) presents an efficient and unique way of estimating the porosity created during the coating build up of molten and semi-molten droplets. However, this method is not able capture the detailed physics during the particle impingement process. The works presented in (Zirari et al. 2010) and (Wu et al. 2009) are limited to 2D simulations, and lack details such as

substrate heat transfer and solidification respectively, which are crucial elements in determining the splat morphology. Furthermore, a central core is not modelled as a moving solid in both cases. This investigation is the first of its kind, to simulate a semi-molten droplet impingement using the CFD approach. The 3D study particularly examines the impingement process during impact, spreading, and solidification. The results give an insight to the transient heat transfer process, and illustrate the freezing-induced break-up mechanism at the splat periphery.

7.2 Numerical methods

A semi-molten ziconia (ZrO_2) droplet with an outside diameter of 50 μm and solid core diameter of 30 μm is simulated to impact on a smooth, flat, stainless steel substrate. The particle impact velocity is 10 ms^{-1}. A cross section of the full 3D domain is provided in Figure 7.1, showing the main dimensions and the particle-substrate separation distance. The 3D domain consists of 7 million unstructured computational cells with a refined grid at the substrate surface and around the initial droplet location, as highlighted in Figure 7.1.

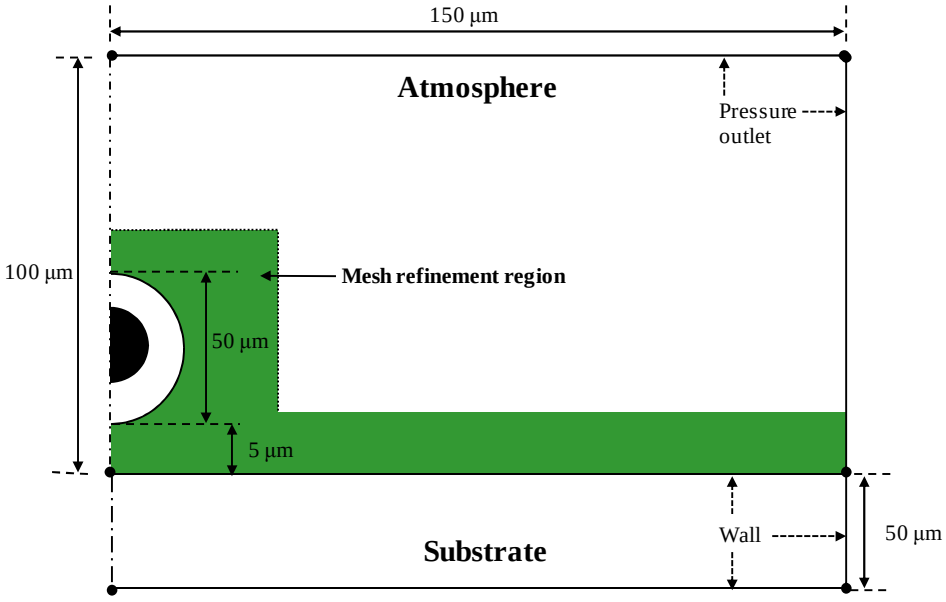

Figure 7.1: A schematic diagram showing a slice of the 3D computational domain for simulating the partially-molten zirconia droplet.

The method for predicting the initial temperature profile through the impinging droplet and the mesh adaptation techniques are outlined in the following sections. The flow and thermal modelling techniques are given in Chapter 6. The thermal-physical properties of the materials present in the simulation are summarised in Table 7.1.

Impinging droplet material	Zirconia (ZrO_2)
Substrate material	Stainless Steel (SS)
Substrate initial temperature	300 K
Solidus temperature (ZrO_2)	2949 K
Liquidus temperature (ZrO_2)	2951 K
Thermal conductivity (liquid ZrO_2)	2.00 W (m K)$^{-1}$
Thermal conductivity (solid ZrO_2)	2.32 W (m K)$^{-1}$
Thermal conductivity (SS)	14.9 W (m K)$^{-1}$
Density (liquid ZrO_2)	5890 kg (m)$^{-1}$
Density (solid ZrO_2)	5890 kg (m)$^{-1}$
Density (SS)	7900 kg (m)$^{-1}$
Droplet surface tension	0.507 N (m)$^{-1}$
Specific heat capacity (solid ZrO_2)	580 J (kg K)$^{-1}$
Specific heat capacity (liquid ZrO_2)	713 J (kg K)$^{-1}$
Specific heat capacity (SS)	477 J (kg K)$^{-1}$
Latent heat of fusion	707000 J (kg)$^{-1}$

Table 7.1: Material properties for the simulation of a partially-molten zirconia droplet impinging onto a stainless steel substrate.

7.2.1 Initial particle temperature profile

In this investigation a 50 μm zirconia particle is simulated to travel within a plasma jet with a realistic average plasma flame temperature T_f and particle convective heat transfer coefficient h_c of 6250 K and 22000 W/m^{2}K respectively (Xiong et al. 2005). The particle heat transfer and melting model is based on the work outlined in Chapter 4 for titanium particles. In this chapter radiation heat transfer in included. The heat transfer between the plasma and the particle surface is determined by convection and radiation and the resulting heat transfer through the particle is calculated in spherical coordinates by Equation 7.1, which includes the latent heat of fusion H_s, thermal conductivity k and the specific heat capacity C_p. Equation 7.1 is then reduced to Equation 7.2 by introducing the $\psi(T)$ term, as defined in Equation 7.3, where α is the thermal diffusivity.

$$\rho C_p \frac{\partial T}{\partial t} = k\left(\frac{\partial^2 T}{\partial r^2} + \frac{2}{r}\frac{\partial T}{\partial r}\right) + H_s \rho \frac{df}{dt} \tag{7.1}$$

$$\frac{\partial T}{\partial t} = \frac{\alpha}{\psi(T)}\left(\frac{\partial^2 T}{\partial r^2} + \frac{2}{r}\frac{\partial T}{\partial r}\right) \tag{7.2}$$

$$\psi(T) = \begin{cases} if\ T_s \le T \le T_L\ \ 1 + \dfrac{H_f}{C_p(T_l - T_s)} \\ else\ 1 \end{cases} \tag{7.3}$$

The boundary conditions at the particle surface and centre are defined in Equation 7.4 and 7.5 respectively, where the subscripts *R* and *f* represent the particle outer radius and plasma flame respectively. The emissivity ε is equal to 0.5 as recommended in (Bansal & Zhu, 2005) and (Carslaw & Jaeger, 1959). Equation 7.2 is discretized using the Crank-Nicholson method as outlined in Equation 7.6 where η is the Stefan-Boltzmann constant.

$$4\pi R^2 k \frac{\partial T}{\partial r}\bigg|_{r=R} = 4\pi R^2 h_c\left(T_f - T_R\right) - 4\pi R^2 \varepsilon\eta\left(T_R^4 - T_f^4\right) \tag{7.4}$$

$$\frac{\partial T}{\partial r}\bigg|_{r=0} = 0 \tag{7.5}$$

$$\alpha\frac{\Delta t}{\Delta^2 r}(i^{-1} - 1)T_{i-1}^{n+1} + \left(2\psi_i^n + 2\alpha\frac{\Delta t}{\Delta^2 r}\right)T_i^{n+1} - \alpha\frac{\Delta t}{\Delta^2 r}(i^{-1} - 1)T_{i+1}^{n+1} \tag{7.6}$$

$$= \alpha\frac{\Delta t}{\Delta^2 r}(1 - i^{-1})T_{i-1}^{n} + \left(2\psi_i^n - 2\alpha\frac{\Delta t}{\Delta^2 r}\right)T_i^{n} - \alpha\frac{\Delta t}{\Delta^2 r}(i^{-1} + 1)T_{i+1}^{n}$$

$where, i = 1, 2, 3 \ldots\ldots N - 1$

N is the number of discretization points along the radius of the droplet. After successive refinement it was found that 20 intervals are required to successfully capture the temperature gradient through the droplet. The discretization of Equation 7.4 at the particle surface boundary is given in Equation 7.7. At the centre of the droplet Equation 7.5 is indeterminate. By applying the theorem of L'Hospital Equation 7.5 is transformed to Equation 7.8, which is descretized to Equation 7.9.

$$-T_{N-1}^{n+1} + \left(1 - \frac{h^n \Delta r}{k_i^n}\right)T_N^{n+1} = \frac{h^n \Delta r}{k_i^n}T_f - \frac{\varepsilon\eta\Delta r}{k_i^n}\left[(T_{N-1}^n)^4 - T_f^4\right] \tag{7.7}$$

$$\frac{\partial T}{\partial t} = 3\frac{\alpha}{\psi(T)}\frac{\partial^2 T}{\partial r^2} \tag{7.8}$$

$$\left(\psi_0^n + 3\alpha\frac{\Delta t}{\Delta^2 r}\right)T_0^{n+1} - \left(3\alpha\frac{\Delta t}{\Delta^2 r}\right)T_1^{n+1} = \left(\psi_0^n - 3\alpha\frac{\Delta t}{\Delta^2 r}\right)T_0^n + \left(3\alpha\frac{\Delta t}{\Delta^2 r}\right)T_1^n \tag{7.9}$$

The discretized equations are solved using the Gauss Seidel iterative method. The simulation time step is 10^{-7} seconds. The convergence condition is tested and set to 10^{-7}. The resulting temperature profile through the particle at 0.0024 seconds is depicted

in Figure 7.2. This temperature profile is then applied as the initial condition for the particle at the start of the simulation, with a central solid core of 30 μm.

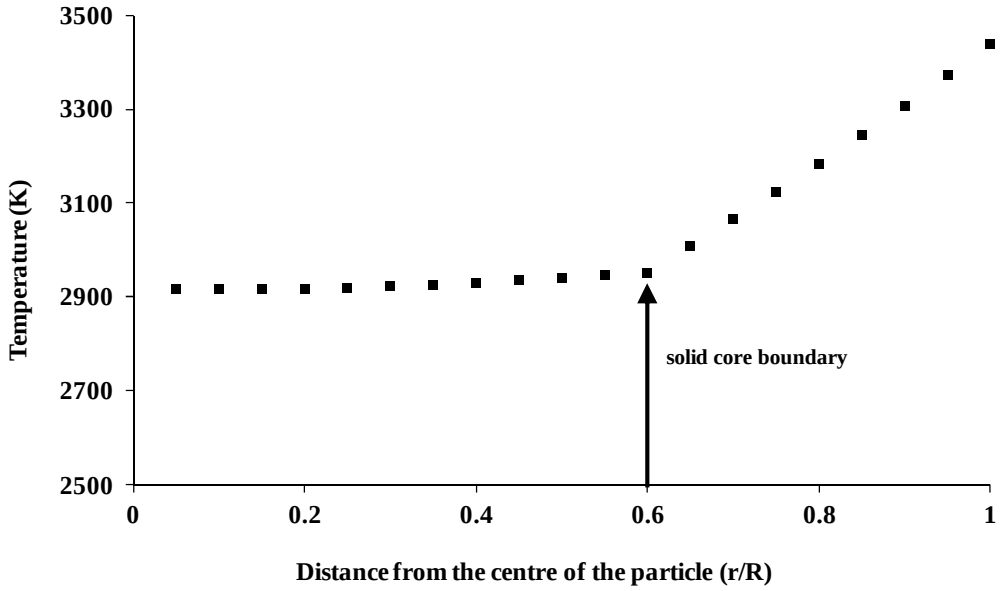

Figure 7.2: Graph showing the temperature profile though the partially-molten zirconia droplet at the start of the impingement simulation

7.2.2 Mesh adaptation technique

The computational mesh surrounding the moving core is dynamically modified after every simulation time step in order to accommodate the motion of the solid core boundary at the centre of the droplet. The pressure and shear stress forces acting on the solid core are used to compute the motion of its centre of gravity. The computational volume mesh is updated after each time step based on the new positions of the solid core boundary surface. This mesh adaptation is calculated by combining spring-based smoothing and local re-meshing as available in Ansys fluent 12.

In summary, for the spring-based smoothing the mesh edges are modelled as a network of ideal springs which obey Hooke's law. Hence, a displacement of one node induces a force proportional to the displacement on the connected nodes, as in Equation 7.10.

$$\vec{F}_i = \sum_j^{n_i} c_{ij}(\Delta\vec{x}_j - \Delta\vec{x}_i) \tag{7.10}$$

The stiffness c_{ij} applied in this investigation is equal to 1. The final equilibrium position of each mesh node is found by iterating using Equation 7.11 and performing a Jacobi

sweep over all interior nodes so that the net force at each node is equal to 0. Once convergence is reached the nodal positions are updated using Equation 7.12.

$$\Delta\vec{x}_i^{m+1} = \frac{\sum_j^{n_i} c_{ij}\Delta\vec{x}_j^m}{\sum_j^{n_i} c_{ij}} \tag{7.11}$$

$$\vec{x}_i^{n+1} = \vec{x}_i^n + \Delta\vec{x}_i^{m,converged} \tag{7.12}$$

In Equation 7.12 *n* and *n+1* represent the current and next time step respectively. The skewness of a cell is defined in Equation 7.13. During the simulation the mesh cells are updated if the skewness value is greater than 0.8, if its length scale is smaller than 10^{-7} m or if its length is greater than $1.5\text{x}10^{-5}$.

$$Skewness = \frac{optimal\ cell\ volume - cell\ volume}{optimal\ cell\ volume} \tag{7.13}$$

7.3 Results and discussion

The computational methodology for the impingement and solidification of a fully molten metal droplet is tested in Chapter 6 using a 2D axisymmetric computational domain, where the experimental and simulated results are of the same scenario show a good level of concordance during all stages of spreading, retardation and recoil.

7.3.1 Semi solid droplet impact and heat transfer

When a droplet impacts onto a substrate surface, the splat development may follow one of two main processes. The particle may simply impinge, deform intact and then solidify. On the other hand, it may impinge, deform and splash to some degree. This break-up process may be triggered by either low heat transfer to the substrate leading to splat fragmentation; or freezing-induced break-up where the heat transfer to the substrate is rapid (Dhiman et al., 2007). The substrate temperature can therefore largely determine the splat morphology. A critical temperature termed the transition temperature (Fuchais et al. 2004) T_T is the temperature below which heat transfer is rapid, leading to freezing-induced break-up.

Experimental observations of zirconia droplets impacting onto a quartz glass substrate of temperatures between 300K and 760K are carried out in (Shinoda & Murakami 2010) leading to a vast difference in final splat morphology patterns. For these observations a substrate temperature of 300 K is shown to reside well below the transition temperature, creating a fragmented splat shape due to freezing-induced break-up. In fact, T_T is predicted to be 513 K < T_T < 673 K. For the simulated stainless steel substrate the thermal conductivity is 14.9 W/(mK), which is roughly 20 times

higher than quartz glass (Dhiman & Chandra, 2005). For this reason T_T of stainless will be considerably higher than the experimental quartz glass substrate. As a result, freezing-induced break-up also develops during the simulation due to the initial substrate temperature of 300 K.

The final simulated splat morphology is compared alongside the experimental observation in Figure 7.3, deposited by hybrid plasma spraying. The two morphologies show a good likeness. An uneven central splat remains at the impact site. The splat has an uneven boundary with an undulating circumference consisting of different sized, but relatively short fingers. The majority of the satellite droplets are not resolved in the simulation towards the outside of the computational domain due to the coarser mesh in this region.

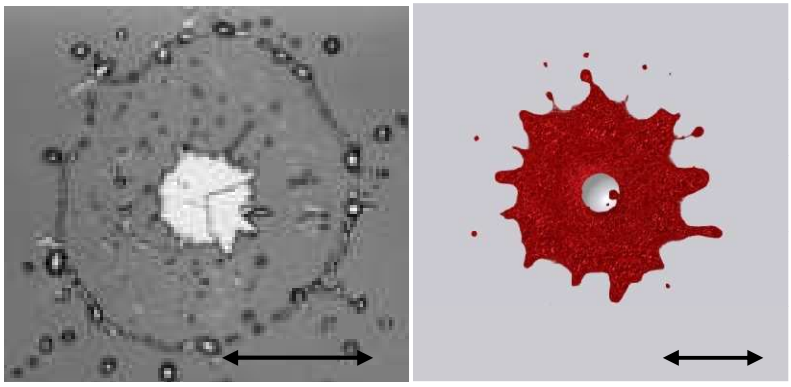

Figure 7.3: Comparison between experimental and simulated zirconia droplet impinging onto a substrate at a temperature of 300 K, deposited by hybrid plasma spraying (Shinoda & Murakami 2010). Scale represents 100 μm.

A cross section of the solidified splat shape is shown in Figure 7.4. A thin shell cups the solid centre and porosity is present around the bottom-side of the spherical solid centre. These two factors, in reality, would inhibit the chance of successful adhesion of the solid core.

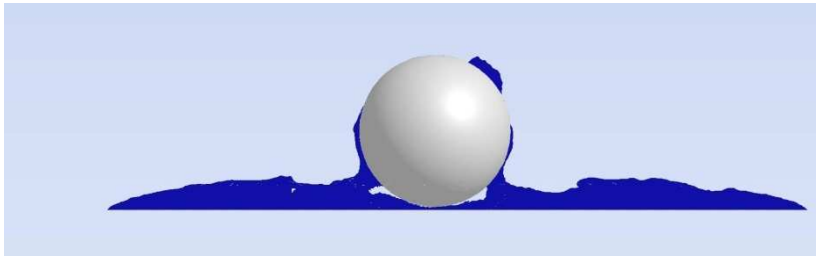

9.67×10^{-2} s

Figure 7.4: Fully solidified splat of semi-molten zirconia droplet with 30 μm central core

Figure 7.5 shows the transient impact, deformation and break-up of the simulated semi-solid ZrO_2 droplet, which leads to the final splat shape discussed in the previous paragraph. The droplet initially spreads in a uniform manner until 3.62×10^{-6} s. The circumference of the droplet then begins to deform at the periphery producing fingers, which are induced by surface tension forces. At the tip of the fingers satellite droplets are emitted in a radial direction.

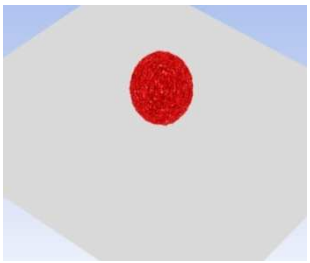

0.00 s

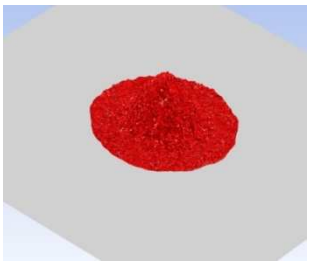

3.62x10^{-6} s

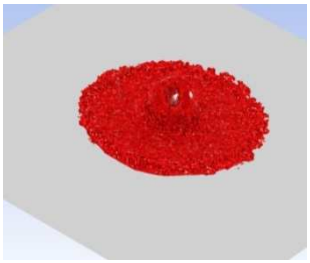

5.87x10^{-6} s

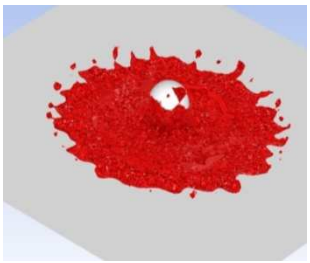

1.17x10^{-5} s

1.69 x10^{-5} s

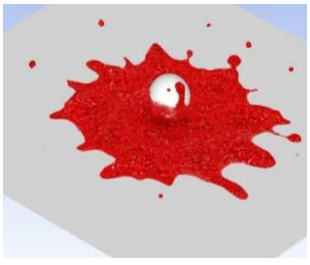

2.87 x10^{-5} s

Figure 7.5: Simulated splat development of 50 μm semi-molten zirconia droplet impinging at 10 ms^{-1} onto a stainless substrate.

This freezing-induced break-up mechanism is illustrated in detail in Figure 7.6, where the solid region represents the solidified ZrO_2 and the contour defines the liquid air boundary. The contours indicate that the ejection of matter in this instance is not caused by the solidified material creating an obstruction to the flow of the molten material, as is commonly thought (Dhiman et al. 2007, Dhiman & Chandra, 2005). Rather, the solidification process decelerates the splat, causing the solid and liquid components to separate.

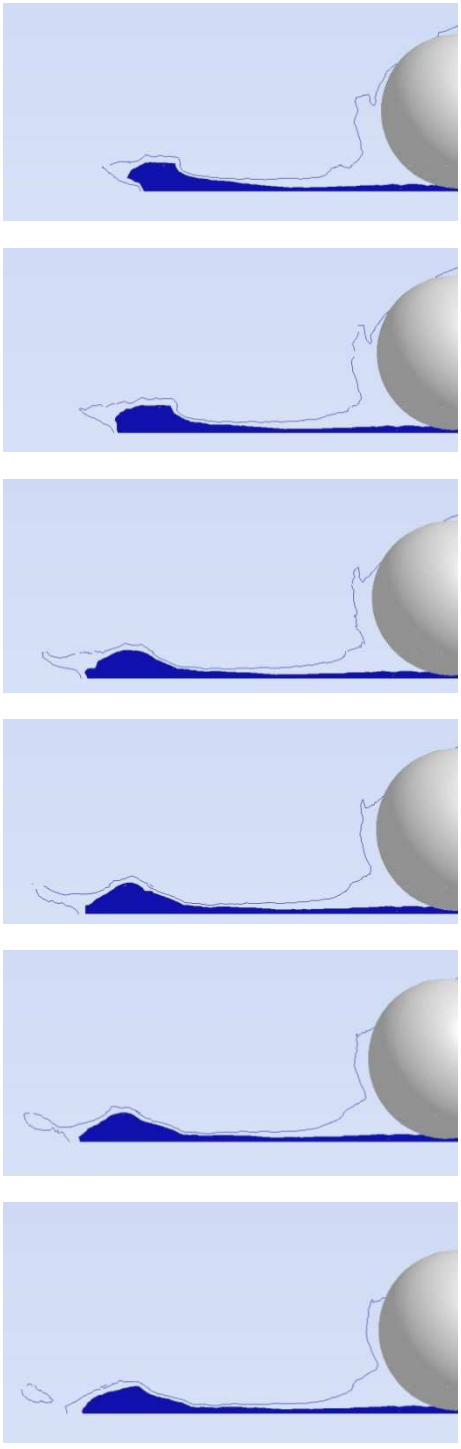

Figure 7.6: Freezing-induced break-up mechanism for the 50 μm semi-molten zirconia droplet impinging at 10 ms^{-1} onto a stainless substrate.

The vertical temperature variation with time through the centre of the computational domain is shown in Figure 7.7. Region 1 describes the flow of thermal energy at the substrate centre. Here, the temperature initially rises rapidly to roughly 1100 K, heated by the central core. After $7.27x10^{-5}$ s the rate of thermal energy conducted away from this central region of the substrate is greater than the heat

energy absorbed from the solid core. As a result, the temperature begins to decrease. The rate of heating and cooling at the substrate surface is critical, and can determine the chance of melting at the impact zone. In this instance the substrate temperature remains below the melting throughout the simulation duration. Region 2 of Figure 7.7 describes the rate of cooling through the centre of the solid core. Even after the particle has reached its final splat shape at 2.87×10^{-5}, the solid core temperature through its centre is almost unchanged. The direction of heat transfer is downwards, via conduction to the substrate. Interestingly, the total time required to completely solidify is much larger than expected. The splat solidifies at roughly 9.67×10^{-2} s, compared to 2.87×10^{-5} s to completely spread. The core acts as a central heat source which delays the rate of solidification of the liquid droplet material around the core. This region bonds the central core to the substrate. If the surrounding zirconia remains in a liquid state for a prolonged period, as in this instance, it is likely that the core would physically detach from the substrate.

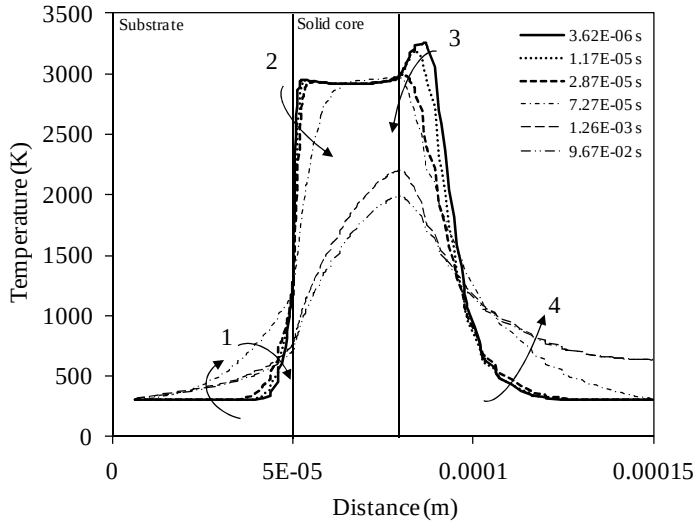

Figure 7.7: Vertical temperature profile through the centre of the computational domain at different time intervals.

7.4 Conclusion

For the first time a semi-molten droplet is simulated to impact onto a solid substrate, which consists of an undeforming, moving, solid core. The impact, spreading and break-up of a 50 μm zirconia droplet with a solid centre of 30 μm is simulated, with a final splat which shows a good likeness to experimental comparison. Furthermore, the freezing induced break-up phenomenon at the splat periphery is described in detail.

In some cases an artificial perturbation can be applied in order to trigger the fingering process at the splat periphery (Bussmann et al. 2000). In the case if this simulation it is likely that the solidification process triggered the instability required to induce the fingering process, as was also found by Mehdizadeh et al. (2004). A notable aspect of this simulation case is a splat shape which is not symmetric (see Figure 7.5). Rather, the splat periphery possesses a seemingly random shape which is similar to the real deposited droplets. This phenomenon highlights the sensitivity of the simulation to minute residual differences that lead to the development of organic morphologies like those found in reality.

While the common approach for these types of simulation would be to capture only a quarter slice of the 3D computational domain with a periodic boundary, the downside to the current methodology is that the domain has to be modelled in its entirety in order to apply the mesh adaptation scheme. This unfortunately leads to a high computational expense. The next step of this investigation should aim to investigate the effects of solid mass fraction and overall particle size on the impact mechanisms and final splat morphologies.

8 Thesis conclusions

Supersonic flow phenomena, combustion, discrete droplet and particle migration with heating, phase change and disintegration, and particle Impingement phenomena at the substrate are studied in this thesis. Each published set of results provide an individual understanding of the underlying physics which control different aspects of thermal spray systems. Parametric studies have been carried out for HVOF, warm spray, and cold spay systems which help to build up a more thorough understanding of process design requirements for supersonic thermal spray systems. A detailed description of the gas phase characteristics through liquid fuelled HVOF, warm spray, and cold spray systems are built and the interrelations between the gas and powder particle phases are discussed. A further study looks in detail at the disintegration of discrete phase water droplets, providing a new insight to the mechanisms which control droplet disintegration with HVOF; providing a step forward in the understanding of liquid feedstock devices and nanostructured coatings. In parallel with these gas-particle-droplet simulations, the impingement of molten and semi-molten powder droplets at the substrate are investigated and the models applied simulate the impingement, spreading and solidification. The results obtained shed light on the break-up phenomena on impact and describe in detail how the solidification process varies with an increasing impact velocity. The results obtained also visually describe the freezing induced break-up phenomenon at the splat periphery.

8.1 Novel contributions to the science of thermal spraying

This project has investigated through numerical simulation several different thermal spray techniques in order to provide a detailed understanding of the current supersonic thermal spraying for powder based coatings, as well as impingement characteristics of the powders at the substrate. The following are a list of the chapter by chapter novel contributions made during this project. All contributions are published within peer reviewed journals which can be found in the *List of publications* section of this thesis.

- *Chapter two* reveals in detail for the first time the compressible gas phase phenomena through the most widely used liquid fuelled HVOF thermal spray system, the JP5000. This CFD modelling approach incorporates: combustion with discrete phase fuel droplets, turbulence, and compressible flow and is used to build a scientific understanding of the geometric design consideration for liquid fuelled HVOF processing.

- *Chapter three* examines for the first time the effects of changing the nozzle cross-section shape on the particle distribution and velocities within cold gas dynamic spraying. The results show that relative to the elliptical cross section, the circular and square cross-sections have the least dispersed powder distribution as well as the greatest average particle velocities. Therefore a circular or square cross section should be selected in order to achieve the very highest particle velocities. However the velocity reduction within the elliptical flow is relatively small, at a maximum of roughly 20 ms^{-1}. A more dispersed particle flow is advantageous for the buildup of an evenly distributed coating, and hence the elliptical cross-sectional shape is deemed the most appropriate design.

- *Chapter three* also investigates the use of a contoured shape for the diverging section of the nozzle with a minimum length using the MOC. A barrel of constant diameter is then added to the exit of the short contoured nozzle making it equivalent in length to the original, with the same throat and exit diameters. The simulated gas and particle velocities are then examined in contrast to the original conical design. The gas flow in the contoured nozzle is accelerated rapidly and the velocity profile remains higher than the conical design throughout the expanding section of the de Laval nozzle. However, due to a decrease in gas density a slightly lower particle velocity is observed for the minimum length MOC nozzle design at the exit and within the stand-off region. However, this difference is negligible. In order to improve the manufacturability of the nozzle one may alternatively produce a minimum length nozzle with an attached barrel of appropriate length.

- *Chapter four* looks at an up-and-coming development of the HVOF thermal spray system, known as warm spray. The effects of injecting a cooling gas on the gas and particle dynamics are examined for the first time. The most poignant results show that the injected cooling gas can be concentrated around the barrel wall producing a cooling boundary layer, where the gas temperature and axial velocity is lower. Small particles of 5 μm diameter are swept along this outer region when injected. The results generated give an improved insight to the interrelations between the gas and particle phases in warm spray, as well as highlight the advantage of warm spray for the deposition of oxygen sensitive materials such as titanium.

- *Chapter five* studies the disintegration of discrete phase water droplets by comparing the time scales of different breakup modes with the rates of evaporation. The results obtained indicate that the droplet disintegration process is dependant on the initial parent droplet sizes. An initial parent droplet between 50 μm and 200 μm in size will breakup, forming droplets which then vaporize only.

For a parent droplet between 200 μm and 500 μm, a fraction of the child droplets will undergo vaporization only, and a fraction will undergo further breakup and simultaneous vaporization. The results obtained in this chapter give a new insight to the mechanisms which control droplet disintegration within HVOF thermal spraying and serve as a fundamental reference for future development of liquid feedstock devices using water based suspensions.

- *Chapter six* applies the volume of fluid method to simulate the boundary between the metallic and atmospheric-gas phases during the impingement of a molten, millimeter sized tin droplet impacting at increasing velocities onto a cold, stainless steel substrate. The results shed light on the break-up phenomena on impact and for the first time describe in detail how the dynamic solidification process varies with an increasing impact velocity. Furthermore, the detailed solidification process is simulated, indicating three unique stages: planar solidification; uneven solidification and wave mixing.

- *Chapter seven* describes a new modelling approach for the simulation of a semi-molten droplet impacting onto a solid substrate, consisting of an undeforming, moving, solid core. The impact, spreading and break-up of a 50 μm zirconia droplet with a solid centre of 30 μm is simulated. The results obtained also visually describe the freezing induced break-up phenomenon at the splat periphery.

8.2 The next steps in thermal spray coatings and the role of numerical simulation

As outlined in the latter stages of *Section 1.1* of this thesis, a great deal of interest has developed over recent years for the thermal spraying of nano-scale and submicron sized powders in order to pursue more complex thermal spray coatings (Fauchais et al. 2011, Killinger et al. 2011, Fauchais & Montavon 2010, Pawlowski 2008a, Pawlowski 2009).

Manufacturing coatings using thermal spray techniques can provide a deposition rate an order of magnitude higher than its closest competitors: Chemical Vapour Deposition (CVD) and Physical Vapour Deposition (PVD). Furthermore, CVD and PVD are unable to produce thick coatings beyond 10 μm. While a variety of thermal spray methods have been utilized in pursuit of depositing nanoparticles from a liquid feedstock, including: plasma, flame, and HVOF, the coatings are difficult to reproduce consistently by the current thermal spraying methods on a large scale.

The deposition of nano-scale and submicron-scale powders requires the current thermal spray techniques to be developed further. The liquid feedstock method is a necessary component of this design in order to give the powders the required momentum to enter the centre of the thermal spray jet and for health and safety reasons during transport and storage. Unfortunately there is a knowledge gap which is preventing thermal spray technology from making the next step forward and entering the commercial market.

In comparison to the conventional spraying of micron-sized particles, liquid processing is far more complex due to the fragmentation and vaporization of the liquid component of the feedstock. The figure below depicts some common clusters formed by a liquid feedstock droplet, and includes: *a)* Thick shell *b)* Inflated thin shell *c)* Fragmented shell *d)* Sintered clusters *e)* Solid melted agglomerates. A full description of these shapes is given in Chapter 5 of this thesis. It is the formation of these unique shapes within the complex thermal spray jet which requires close control in order to create a consistent coating with the required coating architecture.

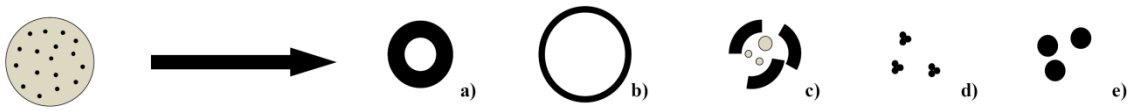

Figure 8.1: Variations in nanopowder cluster shapes during thermal spraying of a liquid feedstock

In order to design and develop the next generation of thermal spray technologies it is highly necessary to simulate and compare the broad range of thermal spray conditions which are achievable using the current technologies. A summary of the expected particle velocities and temperatures achieved by the main industrial thermal spray processes can be found in *Figure 1.3*. By creating these numerical simulations a full spectrum of thermal spray velocities and temperatures could be simulated and the interrelations between the liquid droplets and processing gas could be investigated. This thesis includes the simulation of HVOF, Warm Spray, and Cold Spray. Hydrogen flame and plasma spray are now required.

The simulated trajectory of the droplets and particles, as well as their vaporization and breakup characteristics within HVOF thermal spraying have been studied in *Chapter 5* of this thesis. However, the vaporization and break-up are not simulated simultaneously, and this is a key requirement for the next stages of study. The following bullet-points summarise the key numerical simulation requirements in order to study the complete liquid feedstock droplet disintegration and predict the resulting cluster shapes:

- Plasma flame simulation and validation
- Subsonic and supersonic Hydrogen flame spray simulation and validation
- Thermal and physical property correlations for of nano-porous solids
- Thermal and physical property correlations and nano-fluids
- Diffusion and precipitation of nano-particles within liquid droplets

By coupling the above discrete phase models with the different processing gas conditions the required processing windows for the specific coating architectures depicted in Figure 8.1 can be calculated, and doing so, the mode of thermal spraying for the next generation of nano-powder deposition can be established.

9 Thesis appendix A – computational methodology

9.1 General flow description

This chapter contains further descriptions of the models applied in this project. The CFD approach is based on the assumption of a continuum, where:

$$\begin{bmatrix} rate\ of\ change\ of \\ property\ in\ Vol \end{bmatrix} = \begin{bmatrix} rate\ of\ property \\ being\ created\ in\ Vol \end{bmatrix} + \begin{bmatrix} property\ flowing \\ into\ Vol \end{bmatrix} + \begin{bmatrix} property\ flowing \\ out\ of\ Vol \end{bmatrix}$$

The dynamical behavior of fluid flow is accounted for by the conservation mass, momentum and energy. The droplets and particles which combine with the combined continuum flow field are simuated using the Lagrangian approach, which is also known as the discrete particle model (DPM).

The complete system made by the integral expressions of the three conservation laws is given in Equation 9.1, where Ω represents the control volume and S is the surface that encloses Ω. The first term $\vec{W}$ has five components: representing mass, momentum in all three directions and energy. The terms $\vec{F}_c$ and $\vec{F}_v$ are the convective flux and viscous flux vectors respectively. The vector $\vec{Q}$ includes the contribution of all external volume source and sink terms.

$$\frac{\partial}{\partial t}\int_{\Omega}\vec{W}d\Omega + \int_{S}\left(\vec{F}_c - \vec{F}_v\right)dS = \int_{S}\vec{Q}dS \qquad (9.1)$$

The expanded expressions of the column vectors are given in 9.2.

$$\vec{W} = \begin{bmatrix} \rho \\ \rho u \\ \rho v \\ \rho w \\ \rho E \end{bmatrix}; \vec{F}_c = \begin{bmatrix} \rho V \\ \rho uV + n_x p \\ \rho vV + n_y p \\ \rho wV + n_z p \\ \rho HV \end{bmatrix}; \vec{F}_v = \begin{bmatrix} 0 \\ n_x\tau_{xx} + n_y\tau_{xy} + n_z\tau_{xz} \\ n_x\tau_{yx} + n_y\tau_{yy} + n_z\tau_{yz} \\ n_x\tau_{zx} + n_y\tau_{zy} + n_z\tau_{zz} \\ n_x\Theta_x + n_y\Theta_y + n_z\Theta_z \end{bmatrix}; Q = \begin{bmatrix} 0 \\ \rho f_{ex} \\ \rho f_{ey} \\ \rho f_{ez} \\ \rho\vec{f}_e \cdot \vec{v} + \dot{q}_h \end{bmatrix} \qquad (9.2)$$

In a Newtonian fluid the viscous stresses are proportional to the rate of deformation. The three dimensional form of Newton's law of viscosity for compressible flows includes two constants: the dynamic viscosity μ (relating to linear deformations) and

the second viscosity λ (relating to volumetric deformations). The term τ is the symmetric viscous stress tensor and is defined as:

$$\tau_{ij} = \mu\left(\frac{\partial u_i}{\partial x_j} + \frac{\partial u_j}{\partial x_i}\right) + \delta_{ij}\lambda\vec{\nabla}\cdot\vec{v} \tag{9.3}$$

The effect of the bulk viscosity λ is small in practice and is approximated using Equation 9.4 (Schlichting, 1979).

$$\lambda = -\frac{2}{3}\mu \tag{9.4}$$

The external forces $\bar{f}_e$ (also called body forces) represent all the typology acting directly on the mass: examples are gravitational, Coriolis and buoyancy forces. The total enthalpy *H* is given by the relation in Equation 9.5, where *e* is the internal energy per unit of mass. For a perfect gas the internal energy is given by the equation, where γ is the specific heat ratio (C_p/C_v).

$$H = e + \frac{|v|^2}{2} + \frac{p}{\rho} \tag{9.5}$$

$$e = \frac{p}{\rho(\gamma - 1)} \tag{9.6}$$

9.2 An overview of turbulence modelling

Above a critical Reynolds number a fluid flow becomes random and chaotic. This flow regime is termed turbulent. The modelling of turbulent flow is one of the most unexplainable and challenging concepts within science today. The inherent features of turbulent flow can be summarized by:

- Three dimensional random fluctuations in flowfield variables. As a result the turbulent motion strong increases the mixing behavior of the flow compared to sole molecular diffusion. From a mathematical point of view, the mixing activity is directly related to the presence of gradients in the time-averaged flow.

- The presence of eddies of different size, from a characteristic dimension down to the smallest eddy scaled known as the Kolmogorov length scale.

- The small-scale eddies work against the action of viscous stresses, and the energy associated with the small-scale eddy motion is dissipated and converted into thermal energy.

Most flow regimes encountered in engineering are of a turbulent nature. The only way to obtain a complete description of the flow field in time and space is to solve numerically the Navier-Stokes equations using Direct Numerical Simulation (DNS). Unfortunately the DNS approach is not practical for engineering applications due to the large range of time scales which need to be resolved. For this reason, the instantaneous turbulent flow is solved but is based on approximated solution.

Turbulence models can be divided in to three groups: first order closure, second order closure, and Large eddy simulation (LES). The first order closure models are typically based on the linear eddy viscosity hypothesis introduced by Boussinesq. RSM models employ the exact equations for the Reynolds-stresses $\overline{v_i' v_j'}$ while the closure is necessary for higher order correlation terms $\overline{v_i' v_j' v_k'}$. These two approaches belong to the class known as RANS (Reynolds Averaged Navier Stokes) equations. On the other hand, the Large Eddy Simulation solves the large vortex structures and models the influence of small structure which have a more homogeneous character.

9.3 The RANS equations

Assuming that there are no sources or sink terms acting on the flow, the differential form of the Navier Stokes equations are given in Equation 9.11. The compact notation for the viscous stress tensor is given in Equation 9.12.

$$\begin{aligned}
&\frac{\partial \rho}{\partial t} + \frac{\partial}{\partial x_i}(\rho v_i) = 0 \\
&\frac{\partial}{\partial t}(\rho v_i) + \frac{\partial}{\partial x_i}(\rho v_j v_i) = -\frac{\partial p}{\partial x_i} + \frac{\partial \tau_{ij}}{\partial x_j} \\
&\frac{\partial}{\partial t}(\rho E) + \frac{\partial}{\partial x_j}(\rho v_j H) = \frac{\partial}{\partial x_j}(v_i \tau_{ij}) + \frac{\partial}{\partial x_j}\left(k \frac{\partial T}{\partial x_j}\right)
\end{aligned} \qquad (9.11)$$

$$\tau_{ij} = 2\mu S_{ij} - \left(\frac{2\mu}{3}\right)(\vec{\nabla} \cdot \vec{v})\delta_{ij} \qquad (9.12)$$

The strain rate tensor and the rotation rate tensor are as stated in Equation 9.13.

$$S_{ij} = \frac{1}{2}\left(\frac{\partial v_i}{\partial x_j} + \frac{\partial v_j}{\partial x_i}\right); \quad \Omega_{ij} = \frac{1}{2}\left(\frac{\partial v_i}{\partial x_j} - \frac{\partial v_j}{\partial x_i}\right) \tag{9.13}$$

The underling concept in the statistical analysis which forms the RANS equations is that each flow variable *u* can be decomposed into a fluctuating component u' about its mean value $\overline{u}$, as given in Equation 9.14.

$$u = \overline{u} + u' \tag{9.14}$$

In order to obtain the mean value, there are four possible averaging procedures that can be used, as follows:

a. Time averaging ($\overline{u}$ varies only in space).

b. Spatial averaging ($\overline{u}$ varies only in time).

c. Ensemble averaging ($\overline{u}$ varies with both space and time).

d. Density weighted averaging (Favre decomposition).

The first three methods are also known as Reynolds averaging and when the turbulent flow is stationary and homogeneous they are equivalent. The Favre method is necessary for compressible flows: The analytical expressions for the four methods are:

$$\begin{aligned} &a)\ \overline{u}_i = \lim_{\Delta t\to\infty}\frac{1}{\Delta t}\int_t^{t+\Delta t} u_i dt; \quad b)\ \overline{u}_i = \lim_{\Omega\to\infty}\frac{1}{\Omega}\int_{\Omega} u_i d\Omega; \\ &c)\ \overline{u}_i = \lim_{N\to\infty}\frac{1}{N}\sum_{n=1}^{N} u_i; \quad d)\ \overline{\overline{u}}_i = \frac{1}{\overline{\rho}}\lim_{\Delta t\to\infty}\frac{1}{\Delta t}\int_t^{t+\Delta t}\rho u_i dt; \end{aligned} \tag{9.15}$$

The mean of the fluctuating term is zero, $\overline{u_i'} = 0$, and the mean of the product of the two fluctuating terms not $\overline{u_i' u_j'} \neq 0$. For the Favre decomposition method $\overline{\overline{\rho u_i}} = \overline{\rho}\,\overline{\overline{u}}_i$ and $\overline{\overline{\rho u_i''}} = 0$. The application of the Favre averaging to the equations Navier-Stokes equations outlined in Equation 9.1 yields the so called RANS equations, as given in Equation 9.16, which includes the Reynolds-stress tensor (Equation 9.17).

$$\frac{\partial \overline{\rho}}{\partial t}+\frac{\partial}{\partial x_i}\left(\overline{\rho}\,\overline{\overline{v_i}}\right)=0$$

$$\frac{\partial}{\partial t}\left(\overline{\rho}\,\overline{\overline{v_i}}\right)+\frac{\partial}{\partial x_i}\left(\overline{\rho}\,\overline{\overline{v_j}}\,\overline{\overline{v_i}}\right)=-\frac{\partial \overline{p}}{\partial x_i}+\frac{\partial}{\partial x_j}\left(\overline{\overline{\tau_{ij}}}-\overline{\rho}\,\overline{\overline{v_i''v_j''}}\right) \qquad (9.16)$$

$$\frac{\partial}{\partial t}\left(\overline{\rho}\,\overline{\overline{E}}\right)+\frac{\partial}{\partial x_j}\left(\overline{\rho}\,\overline{\overline{v_j}}\,\overline{\overline{H}}\right)=\frac{\partial}{\partial x_j}\left[\overline{\overline{v_i}}\left(\overline{\overline{\tau_{ij}}}-\overline{\rho}\,\overline{\overline{v_i''v_j''}}\right)\right]+\frac{\partial}{\partial x_j}\left(k\frac{\partial \overline{\overline{T}}}{\partial x_j}-\overline{\rho}\,\overline{\overline{v_j''h''}}+\overline{\overline{\tau_{ij}v_i''}}-\overline{\rho}\,\overline{\overline{v_j''K}}\right)$$

The turbulent kinetic energy is given by the sum of the normal stresses, as given in Equation 9.18.

$$\tau_{ij}^{R}=-\overline{\rho}\,\overline{\overline{v_i''v_j''}} \qquad (9.17)$$

$$\overline{\rho}\,\overline{\overline{K}}=\frac{1}{2}\overline{\rho}\,\overline{\overline{v_i''v_i''}}$$

(9.18)

$$\frac{\partial}{\partial x_j}\left(\overline{\rho}\,\overline{\overline{v_j''h''}}\right) \qquad (9.19)$$

After the averaging procedure there are six more unknown terms introduced in to the system of equations. Furthermore, there are three extra terms for the three components of the turbulent heat-flux vector (Equation 9.19).

9.4 Prandtl mixing length and turbulent viscosity

For a fully-developed and uni-directional flow with a velocity u_1 in the direction x_1, the RANS momentum equation given in Equation 9.6 simplifies to form Equation 9.20. Prandtl (1925) suggests that for this specific flow the fluctuating velocities are given by Equations 9.21 and 9.22.

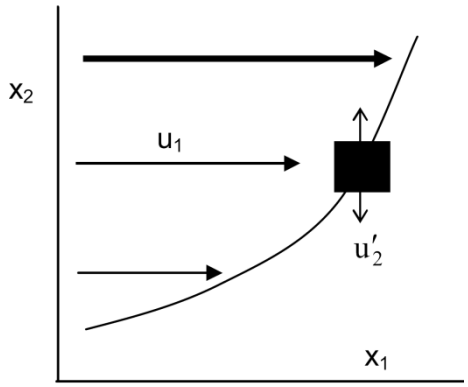

Figure 9.1: Diagram depicting turbulent mixing

Equation 9.22 is the Prandtl mixing length hypothesis, where the Prandtl mixing length l_m is a characteristic length scale for the largest turbulence-containing eddies interacting with the mean flow.

$$\frac{d}{dx_2}\left[\mu\frac{du_1}{dx_2}\right] = \frac{dp}{dx_1} + \frac{d}{dx_2}\left(\rho\overline{u_2'u_1'}\right) \tag{9.20}$$

$$u_1' \propto \frac{du_1}{dx_2} \; and \; u_2' \propto -u_1' \tag{9.21}$$

$$-\rho\overline{u_2'u_1'} = \rho l_m^2 \left|\frac{du_1}{dx_2}\right| \frac{du_1}{dx_2} \tag{9.22}$$

The effect of this turbulent stress term is similar qualitatively to molecular diffusion. One of the major effects of turbulence on fluid flow is to enhance the mixing, with an increase in the apparent viscosity. Boussinesq (1877) proposed the use of a turbulent viscosity μ_t to define the turbulent shear stress by analogy with the Newtonian shear stress in a laminar flow, as outlined in Equation 9.23.

$$(\tau_{21}) = (\tau_{21})_{\;laminar} + (\tau_{21})_{turbulent} \tag{9.23}$$

$$= \mu\frac{du_1}{dx_2} + \left(-\rho\overline{u_2'u_1'}\right)$$

$$= \mu \frac{du_1}{dx_2} + \mu_t \frac{du_1}{dx_2}$$

$$= (\mu + \mu_t) \frac{du_1}{dx_2}$$

The turbulent viscosity is not a physical property of the fluid, but represents the effect of turbulence on the average flow behaviour. The effective viscosity, $\mu_{eff} = \mu + \mu_t$, is typically around a thousand times larger than the molecular viscosity in a fully turbulent flow.

9.5 Summary of the k-ε turbulence model

This two-equation turbulence model includes the solution of two additional transport equations for the turbulent kinetic energy $\overline{\overline{K}}$ and one for the turbulent kinetic energy dissipation rate ε. The standard K-ε expression implemented is given in Equation 9.24.

$$\frac{\partial \overline{\rho}\,\overline{\overline{K}}}{\partial t} + \frac{\partial}{\partial x_j}\left(\overline{\overline{K}}\,\overline{\rho}\,\overline{\overline{v_j}}\right) = \frac{\partial}{\partial x_j}\left[\left(\mu + \frac{\mu_T}{Pr_K}\right)\frac{\partial \overline{\overline{K}}}{\partial x_j}\right] - \overline{\rho}\varepsilon - P_K - P_b - 2\overline{\rho}\varepsilon M_T^2$$
$$P_K = \overline{\rho}\,\overline{\overline{v_i'' v_j''}}\,\frac{\partial \overline{\overline{v_i}}}{\partial x_j}; \quad P_b = g_i \frac{\mu_T}{\overline{\rho}\,Pr_T}\frac{\partial \overline{\rho}}{\partial x_i}; \quad M_T = \sqrt{\frac{\overline{\overline{K}}}{a^2}} \qquad (9.24)$$

where P_K and P_b are the production of turbulent kinetic energy due to main velocity gradients and buoyancy, respectively. The expression for approximating the dissipation of turbulent kinetic energy is given in Equation 9.25. The quantity Pr_K and Pr_ε are the Prandtl number for $\overline{\overline{K}}$ and ε with values 1.0 and 1.3 respectively. The eddy viscosity is given by Equation 9.26. The coefficients for C_{ε_1}, C_{ε_2}, and C_μ are 1.44, 1.92 and 0.09 respectively.

$$\frac{\partial \overline{\rho}\varepsilon}{\partial t} + \frac{\partial \overline{\rho}\varepsilon \overline{\overline{v_j}}}{\partial x_j} = \frac{\partial}{\partial x_j}\left[\left(\mu + \frac{\mu_T}{Pr_\varepsilon}\right)\frac{\partial \varepsilon}{\partial x_j}\right] - \left(C_{\varepsilon 1} P_K + C_{\varepsilon 2}\overline{\rho}\varepsilon + C_{\varepsilon 3} P_b\right)\frac{\varepsilon}{\overline{\overline{K}}} \qquad (9.25)$$

$$\mu_T = C_\mu \overline{\rho}\,\frac{\overline{\overline{K^2}}}{\varepsilon} \qquad (9.26)$$

The coefficient $C_{\varepsilon 3}$ is expressed as a function as given in Equation 9.27 where V_n is the velocity component aligned to the gravity direction and V_n is the velocity component normal to the force of gravity.

$$C_{\varepsilon 3} = tanh\left|\frac{v_t}{v_n}\right| \qquad (9.27)$$

9.6 Summary of the Reynolds stress turbulence model

The Reynolds stress model (RSM) is the most complete type of turbulence model that can be applied, and is without the isotropic eddy-viscosity hypothesis that is applied in the k-ε model. The RSM closes the Reynolds-averaged Navier-Stokes equations by solving transport equations for the Reynolds stresses together with an equation for the dissipation rate. Hence, five additional transport equations are required in 2D flows and seven in 3D. Since the RSM accounts for the effects of streamline curvature, swirl, rotation, and rapid changes in strain rate in a more rigorous manner than one-equation and two-equation models, it has greater potential to give accurate predictions for complex flows. The exact transport equations for the transport of the Reynolds stresses are as follows in Figure 9.2.

$$\underbrace{\frac{\partial}{\partial t}(\rho\,\overline{u_i'u_j'})}_{\text{Local Time Derivative}} + \underbrace{\frac{\partial}{\partial x_k}(\rho u_k \overline{u_i'u_j'})}_{C_{ij}\equiv\text{Convection}} = \underbrace{-\frac{\partial}{\partial x_k}\left[\rho\,\overline{u_i'u_j'u_k'} + \overline{p\left(\delta_{kj}u_i' + \delta_{ik}u_j'\right)}\right]}_{D_{T,ij}\equiv\text{Turbulent Diffusion}}$$

$$+ \underbrace{\frac{\partial}{\partial x_k}\left[\mu\frac{\partial}{\partial x_k}(\overline{u_i'u_j'})\right]}_{D_{L,ij}\equiv\text{Molecular Diffusion}} \underbrace{-\rho\left(\overline{u_i'u_k'}\frac{\partial u_j}{\partial x_k} + \overline{u_j'u_k'}\frac{\partial u_i}{\partial x_k}\right)}_{P_{ij}\equiv\text{Stress Production}} \underbrace{-\rho\beta(g_i\overline{u_j'\theta} + g_j\overline{u_i'\theta})}_{G_{ij}\equiv\text{Buoyancy Production}}$$

$$+ \underbrace{\overline{p\left(\frac{\partial u_i'}{\partial x_j} + \frac{\partial u_j'}{\partial x_i}\right)}}_{\phi_{ij}\equiv\text{Pressure Strain}} - \underbrace{2\mu\overline{\frac{\partial u_i'}{\partial x_k}\frac{\partial u_j'}{\partial x_k}}}_{\epsilon_{ij}\equiv\text{Dissipation}}$$

$$\underbrace{-2\rho\Omega_k\left(\overline{u_j'u_m'}\epsilon_{ikm} + \overline{u_i'u_m'}\epsilon_{jkm}\right)}_{F_{ij}\equiv\text{Production by System Rotation}} + \underbrace{S_{\text{user}}}_{\text{User-Defined Source Term}}$$

Figure 9.2: Transport equation for the Reynolds Stresses in the RSM (Ansys Fluent 12.0 Theory Guide)

The value of Pr_k is different from the one used in the standard k-ε model and is equal to 0.82. The turbulent kinetic energy and the dissipation rate are calculated using equations with the same format as k-ε, with coefficient values: Pr_k =0.82 and $Pr_{\square}$ =1. The values of the turbulent kinetic energy obtained from its transport equation are applied as boundary conditions. The computation of k is then from the Reynolds stresses transport equations. The turbulent viscosity in the same way as k-ε model,

with the constant where C_μ=0.09.

9.7 The QUICK discretization scheme

The QUICK scheme can be utilised to compute a higher-order value of the convection term at a face. The QUICK schemes (Leonard & Mokhtari, 1990) are combine a weighted average of second-order-upwind and central interpolations of the variable. For face e in Figure 9.3, and assuming the fluid flow is travelling from the left hand side to the right, the value ϕ_e can be determined by Equation 9.28.

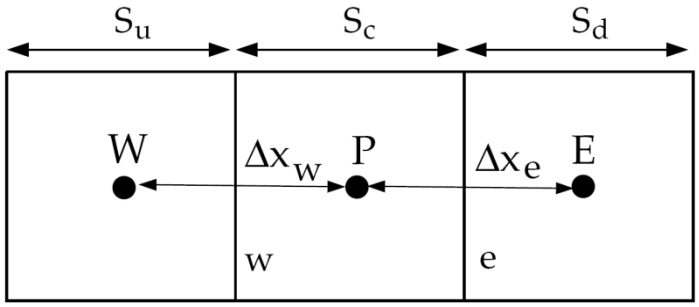

Figure 9.3: Depiction of a one-dimensional control volume

$$\phi_e = \theta\left[\frac{S_d}{S_c+S_d}\phi_P + \frac{S_c}{S_c+S_d}\phi_E\right] + (1-\theta)\left[\frac{S_u+2S_c}{S_u+S_c}\phi_P - \frac{S_c}{S_u+S_c}\phi_W\right] \quad (9.28)$$

In Equation x, setting θ =1 provides a central second-order interpolation whereas θ=0 creates a second-order upwind value. Traditionally the QUICK scheme is solved using θ=1/8.

9.8 Numerical scheme and pressure correction

The segregated pressure-based solver computes the solution of the governing equations sequentially. These governing equations are non-linear and coupled, and therefore the solution is looped iteratively to reach a converged numerical solution. The individual governing equations for the solution variables (e.g., u, v, w, p, T, k, ε, etc) are solved one after another, and hence are “decoupled” or “segregated” from other equations. This method is memory-efficient because the equations only to be stored in the memory one at a time, but solution convergence is relatively slow. Each iterating step consists of the following and loop until the convergence criteria are met:

1. Update fluid properties (density, viscosity, specific heat, thermal conductivity, turbulent viscosity) based on the current solution.
2. Solve the momentum equations, one after another, using the recently updated values of pressure and face mass fluxes.

3. Solve the pressure correction equation using the recently obtained velocity field and mass-flux.
4. Correct face mass fluxes, pressure, and the velocity field using the pressure correction obtained from Step 3.
5. Solve the equations for additional scalars, if any, such as turbulent quantities, energy, species, using the current values of the solution variables.
6. Update the source terms arising from the interactions among different phases (e.g., source term for the carrier phase due to discrete particles).

The discretised continuity equation (see Equation 9.11 for differential form) is used to estimate the required correction to the computed pressure field at each solution point and then produce a velocity field that satisfies continuity. An example grid arrangement is shown in Figure 9.4 and the integrated form of the basic continuity condition for incompressible flow for the 2D control volume shown in Figure 9.4 is given in Equation 9.29 using "backwards staggered" storage notation.

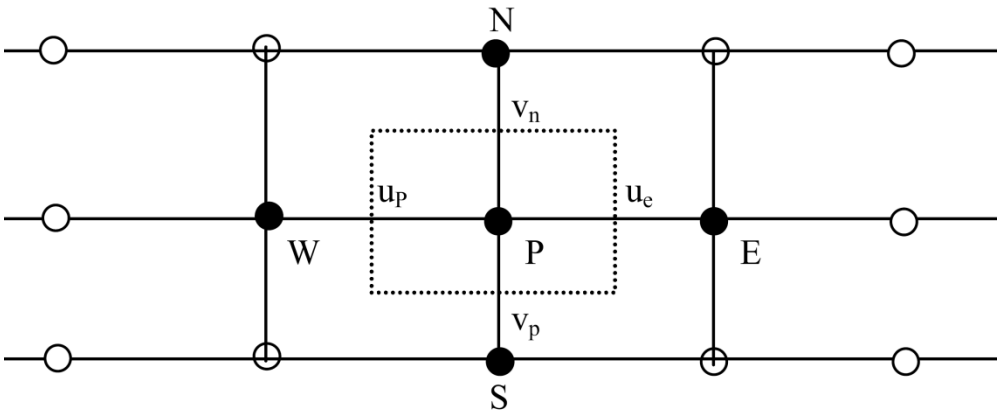

Figure 9.4: Control volume and velocity locations for pressure-correction method

$$(\rho uA)_e - (\rho uA)_p + (\rho vA)_n - (\rho vA)_p = 0 \tag{9.29}$$

Similarly, the momentum equations with perpendicular velocities to the cell faces can be described using the East and North cell faces as examples in Equations 9.30 and 9.31 where a_e and a_p are written in the form of Equation 9.32.

$$a_e u_e = \sum_{nodes}^{neighbour} a_i u_i - (p_E - p_p)A_e + S_{ue} \tag{9.30}$$

$$a_p v_p = \sum_{nodes}^{neighbour} a_i v_i - (p_p - p_S)A_s + S_{vp} \tag{9.31}$$

$$a_i = \left[\frac{\Gamma_\Phi A}{\delta x_1} - \frac{(\rho u_i A}{2}\right]_p \tag{9.32}$$

The momentum equations are solved iteratively in a sequence as outlined above, until a converged solution is achieved. The unknown final solutions to the momentum equations are related to the currently computed fields by corrections to the current values, as outlined in Equation 9.30, where (*) indicates the unknown solution and (^{c}) is the correction required to achieve the converged true solution.

$$u^* = u + u^c \tag{9.33}$$

$$v^* = v + v^c$$

$$p^* = p + p^c$$

The momentum equations in the form of Equations 9.30 and 9.31 can then be written in the form of a true solution and the current solution. Assuming that the source terms are identical, and subtracting one from the other leads to Equation 9.34. By applying the correction terms from Equation 9.33, Equation 9.35 is formed.

$$a_e(u_e^* - u_e) \sum_{nodes}^{neighbour} a_i(u_i^* - u_i) - (p_E^* - p_E)A_e + \left(p_p^* - p_p\right)A_e \tag{9.34}$$

$$a_e u_e^c = \sum_{nodes}^{neighbour} a_i u_i^c - p_E^c A_e + p_p^c A_e \tag{9.35}$$

It is then also assumed that the summation term of the velocity corrections in Equation 9.35 is negligible and a simple relationship between velocity correction and pressure correction term is formed. These velocity corrections can be inserted into Equation 9.36 to form the pressure correction equation, as given in Equation 9.37.

$$(\rho u^c A)_e - (\rho u^c A)_p + (\rho v^c A)_n - (\rho v^c A)_p = (\rho u A)_p - (\rho u A)_e + (\rho v A)_p - (\rho v A)_n \tag{9.36}$$

$$a_p p_p^c \sum_{nodes}^{neighbour} a_i p_i^c + S_{pc}\,, \qquad where\ S_{pc} = (\rho u A)_p - (\rho u A)_e + (\rho v A)_p - (\rho v A)_n \tag{9.37}$$

The method is known as the SIMPLE (Semi-Implicit Method for Pressure-Linked Equations), and is used in many general-purpose codes because of its reliability.

10 Bibliography

Ahmed, A. M. Rangel, R. H. Sobolev, V. V. Guilemany, J. M. (2001) In-flight oxidation of composite powder particles during thermal spraying. *Int. J. Heat Mass Transfer*, 44 (2) 4667-1677.

Ahmed, A. M. Rangel, R. H. (2002) Metal droplet deposition on non-flat surfaces; effects of substrate morphology. *Int. J. Heat Mass Transfer* , 45 (5) 1077-1091.

Alkhimov, A. P. Kosarev, V. F. Papyrin, A. N. (1990) A method of "cold" gas-dynamic deposition, *Sov. Phys. Dokl.,* 35 (12) 1047-1049.

Assadi, H. Gartner, F. Stoltenhoff, T. Kreye, H. (2003) Bonding mechanisms of cold gas spraying. Acta. Mater., 51 (15), 4379-4394.

Anderson, J. D. (2007) Fundamentals of aerodynamics, 4th ed. New York: McGraw-Hill.

Aziz, S. D. Chandra, S. (2000) Impact recoil and splashing of molten metal droplets. *Int. J. Heat. Mass. Transfer*, 43 (16), 2841-2857.

Bae, G. Xiong, Y. Kumar, S. Kang, K. Lee, C. (2008) General aspects of interface bonding in kinetic sprayed coatings. *Acta. Mater.,* 56 (17), 4858-4868.

Bai, X. More, K. Rouleau, C. M. Rabiei, A. (2010) functionally graded hydroxyapatite coating doped with antibacterial components. *Acta Biomaterialia,* 6 (6), 2264-2273.

Balani, K. Agarwal, A. Seal, S. Karthikeyan, J. (2005) Transmission electron microscopy of cold sprayed 1100 aluminum coating. Scripta. Mater., 53, 845-850.

Bansal, N. P. Zhu, D. (2005) Thermal conductivity of zirconia–alumina composites. *Ceram. Int.,* 31 (7), 911-916.

Basu, S. Cetegen, B. M. (2007) Modelling of thermo-physical processes in liquid ceramic precursor droplets injected into a plasma jet. *Int. J. Heat Mass Transfer*, 50 (7-8), 3278-3290.

Basu, S. Cetegen, B. M. (2008) Modeling of liquid ceramic precursor droplets in a high velocity oxy-fuel flame jet, Acta Materialia, 56 (12), 2750–2759.

Bird, R. B. (1960) *Transport phenomena*. USA: John Wiley & Sons.

Bolelli, G. Rauch, J. Cannillo, V. Killinger, A. Lusvarghi, L. Gadow, R. (2009) Microstructural and tribological investigation of high-velocity suspension flame sprayed (HVSFS) Al_2O_3 coatings. *J. Therm. Spray Technol.*, 18 (1), 35-49.

Bonini, M. Bardi, U. Berti, D. Neto, C. Baglioni, P. (2002) A new way to prepare nanostructured materials: flame spray of microemulsions. *J. Phys. Chem. B*, 106 (24). 6178-6183.

Boussinesq, J. (1877) Essai sur la The'orie des Eaux Courantes. Mém. présentés par div.sav. à 1'Acad. des Sci.

Boyer, R. R. (1996) An overview on the use of titanium in the aerospace industry. *Mater. Sci. Eng. A,* 213 (1-2), 103-114.

Brackbill, J. U. Kothe, D. B. Zemach, C. (1992) A continuum method for modelling surface tension. *J. Comput. Phys.*, 100 (2), 335-354.

Brossard, S. Munroe, P. R. Tran, A. Hyland, M. M. (2010) Study of the splat-substrate interface for a NiCr coating plasma sprayed onto polished aluminium and stainless steel substrates. *J. Therm. Spray Techn.*, 19 (1-2), 24-30.

Browning, J. A. (1992) Thermal spray method and apparatus for optimizing flame jet temperature. US patent number 5330798.

Bussmann, M. Mostaghimi, J. Chandra, S. (1999) On a three-dimensional volume tracking model of droplet impact. *Phys. Fluids,* 11 (6), 1406-1417.

Bussmann, M. Chandra, S. Mostaghimi, J. (2000) Modelling the splash of a droplet impacting on a solid surface. *Phys. Fluids,* 12, 3121-3132.

Cannillo, V. Lusvarghi, L. Sola, A. (2008) Production and characterization of plasma-sprayed TiO_2–hydroxyapatite functionally graded coatings. *J. Eur. Ceram. Soc.*, 28 (11), 2161–2169.

Cengal, Y. A. Boles, M. (2002) *Thermodynamics: An Engineering Approach, 4t^h Ed* McGraw-Hill.

Carslaw, H. S. Jaeger, J. C. (1959) Conduction of heat in solids *2nd edition.* Oxford, UK: Clarendon press.

Cetegen, B. M. Basu, S. (2009) Review of Modeling of Liquid Precursor Droplets and Particles Injected into Plasmas and High-Velocity Oxy-Fuel (HVOF) Flame Jets for Thermal Spray Deposition Applications. *J. Therm. Spray Techn.*, 18 (5-6), 769-703.

Chandra, S. Fauchais, P. (2009) Formation of solid splats during thermal spray deposition. *J. Therm. Spray Techn.*, 18 (2), 148-180.

Chen, D. Jordan, E. H. Gell, M. (2008) Effect of solution concentration on splat formation and coating microstructure using the solution precursor plasma spray process. *Surf. Coat. Technol.,* 202, 2132–2138.

Cheng, D. Xu, Q. Trapaga, G. Lavernia, E. J. (2001) A numerical study of high-velocity oxygen fuel thermal spraying process. Part I: Gas phase dynamics. *Metall. Mater. Trans. A,* 32 (7), 1609-1620.

Cheng, D. Trapaga, G. J. McKelliget, W. Lavernia, E. J. (2003) Mathematical modelling of high velocity oxygen fuel thermal spraying of nanocrystalline materials: an overview. *Modelling Simul. Mater. Sci. Eng.,* 11, R1-R31.

Crank, J. (1984) Free and moving boundary Problems. Clarendon Press, Oxford.

Crowe, C. T. Sommerfeld, M. Tsuji, Y. (1998) *Multiphase flows with droplets and particles*. London: CRC Press.

Davies, J. R. (2004) *Hand book of thermal spray technology*. USA: ASM International.

Deguchi, S. Ghosh, S. K. Alargova, R. G. Tsujii, K. (2006) Viscosity Measurements of Water at High Temperatures and Pressures Using Dynamic Light Scattering. *J. Phys. Chem. B,* 110 (37), 18358-18362.

Dent, A. H. Horlock, A. J. McCartney, D. G. Harris S. J. (2000) Microstructure formation in high velocity oxy-fuel thermally sprayed Ni–Cr–Mo–B alloys. *Mater. Sci. Eng. A,* 283 (1-2), 242–250.

Dhiman, R. Chandra, S. (2005) Freezing-induced splashing during impact of molten metal droplets with high Weber numbers. *Int. J. Heat Mass Transfer*, 48 (25-26), 5625-5638.

Dhiman, R. McDonald, A. G. Chandra, S. (2007) Predicting splat morphology in a thermal spray process. *Surf. Coat Tech.* 201(18), 7789-7801.

Donachie Jr., M. J. (2000) *Titanium: A technical guide, 2nd ed.* Ohio: ASM International.

Donner, K. -R. Gaertner, F. Klassen, T. (2011) Metallization of Thin Al_2O_3 Layers in Power Electronics Using Cold Gas Spraying. *J. Therm. Spray. Techn.,* 20 (1-2) 299-306.

Ducos, M. Durand, J. -P. (2001) Thermal coatings in Europe: a business perspective. *J. Therm. Spray Technol.*, 10 (3), 407–411.

Fan, S. -Q. Li, C. -J. Li, C. -X. Liu, G. J. Yang, G. -J. Zhang, L. -Z. (2006) Preliminary study of performance of dye sensitized solar cell of nano-TiO_2 coating deposited by vacuum cold spray. *Mater. Trans.,* 47 (7), 1703-1709.

Fauchais, P. Fukumoto, M. Vardelle, A. Vardelle, M. (2004) Knowledge concerning splat formation: An invited review. *J. Therm. Spray. Techn.,* 13 (3), 337-360.

Fauchais, P. Montavon, G. (2010) Latest Developments in Suspension and Liquid Precursor Thermal Spraying. *J. Therm. Spray Technol.*, 19 (1-2), 226-239.

Fauchais, P. Montavon, G. Lima, R. S. Marple, B. R. (2011) Engineering a new class of thermal spray nano-based microstructures from agglomerated nanostructured particles, suspensions and solutions: an invited review. *J. Phys. D: Appl. Phys.,* 44 (9), 1-53.

Fauchais, P. and Vardelle, A. (2011) Innovative and Emerging Processes in Plasma Spraying: from micro- to nano- structured coatings *J. Phys. D: Appl. Phys.*, 44 (19), 1-14.

Freese, H. L. Volas, M. G. Wood, J. R. (2001) Metallurgy and technological properties of titanium and titanium alloys IN: Brunette, D. M. Tengvall, P. Textor, M. Thomsen, P., *Titanium in Medicine: Material Science, Surface Science, Engineering, Biological Responses and Medical Applications*, Berlin: Springer, 25-52.

Fukumoto, M. Huang, Y. (1999) Flattening mechanisms in thermal sprayed nickel particle impinging on a flat substrate surface. *J. Therm. Spray Techn.*, 8 (3), 427-432.

Gadow, R. Killinger, A. Rauch, J. (2008) New Results in High Velocity Suspension Flame Spraying (HVSFS). *Surf. Coat. Technol.*, 202 (18) 4329-4336.

Ghafouri-Azar, R. Mostaghimi, J. Chandra, S. (2004) Numerical study of impact and solidification of a droplet over a deposited frozen splat. *Int. J. Comput. Fluid. D.,* 18 (2) 133-138.

Ghafouri-Azar, R. Yang, Z. Chandra, S. Mostaghimi, J. (2005) Impact of molten metal droplets on the tip of a pin projecting from a flat surface. *Int. J. Heat. Fluid. Fl.*, 26 (2) 334-347.

Dykhuizen, R. C. Smith, M. F. (1998) Gas dynamic principles of cold spray. *J. Therm. Spray Technol.,* 7 (2), 205-212.

Gibson, M. M. Launder, B. E. (1978) Ground effects on pressure fluctuations in the atmospheric boundary layer. *J. Fluid Mech.,* 86 (3), 491–511.

Grujicic, M. Saylor, J. R. Beasley, D. E. De Rosset, W. S. Helfritch, D. (2003) Computational analysis of the interfacial bonding between feed-powder particles and the substrate in the cold-gas dynamic-spray process. *Appl. Surf. Sci.*, 219 (3-4), 211-227.

Grujicic M., Zhao C.L., De Rosset W.S., Helfritch D. (2004) Adiabatic shear instability based mechanism for particles/substrate Bonding in the Cold-Gas Dynamic-Spray Process, Mat. Des.. 25 (8), 681-688.

Gu, S. Eastwick, C. N. Simmons, K. A. McCartney, D. G. (2001) Computational Fluid Dynamic Modeling of Gas Flow Characteristics in a High-Velocity Oxy-Fuel Thermal Spray System. *J. Therm. Spray Technol.*, 10 (3), 461-469.

Gu, S. & Kamnis, S. (2009) Bonding Mechanism from the Impact of Thermally Sprayed Solid Particles. *Metall. Mater. Trans. A*, 40 (11), 2664-2674.

Gutwein, L. G. Webster, T. J. (2004) Increased Viable Osteoblast Density in the Presence of Nanophase Compared to Conventional Alumina and Titania Particles. Biomaterials, 25 (18), 4175-4183.

Haas, F. C. (1964) Stability of droplets suddenly exposed to a high velocity gas stream. *AICHE. J*, 10 (6), 920-924.

Hackett, C. M. Settles, G. S. (1995) The influence of the nozzle design on HVOF spray particle velocity and temperature. IN: *Proceedings of the 8th National Thermal Spray Conference*, September 11-15, Houston, Texas, USA.

He, J. Ice, M. Schoenung, J. M. Shin, D. H. Lavernia, E. J. Thermal Stability of Nanostructured Cr_3C_2-NiCr Coatings. *J. Therm. Spray Technol.,* 10 (2), 293-300.

d'Haese, R. Pawlowski, L. Bigan, M. Jaworski, R. Martel, M. (2010) Phase evolution of hydroxapatite coatings suspension plasma sprayed using variable parameters in simulated body fluid. 205 (8), 1236–1246.

Henderson C. B. (1976) Drag coefficients of spheres in continuum and rarefied flows. *AIAA J*, 14 (6), 707–708.

Heine, M. C. Pratsinis, S. E. (2005) Droplet and particle dynamics during flame spray synthesis of nanoparticles. *Ind. Eng. Chem. Res.*, 44 (16), 6222-6232.

Huang, Y. Song, L. Liu, X. Xiao, Y. Wu, Y. Chen, J. Wu, F. Gu, Z. (2010) Hydroxyapatite coatings deposited by liquid precursor plasma spraying: controlled dense and porous microstructures and osteoblastic cell responses. *Biofabrication*, 2 (4), 1-10.

Ivosevic, M. R. Cairncross, A. Knight, R. (2006) 3D prediction of thermally sprayed polymer splats: modelling particle acceleration, heating and deformation on impact with a flat substrate. *Int. J. Heat Mass Transfer*, 49, 3285-3297.

Jen, T. C. Li, L. Cui, W. Chen, Q. and Zhang, X. (2005) Numerical investigations on cold gas dynamic spray process with nano- and microsize particles, *Int. J. Heat Mass Transfer*, 48 (21-22), 4384-4396.

Jodoin, B. Gindrat, M. Dorier, J.-L. Hollenstein, C. H. Loch, M. Barbezat, G. Modelling and diagnostics of a supersonic DC plasma jet expanding at low pressure. IN: *Proceedings of the 2002 international thermal spray conference*, March 4-6, Essen, Germany.

Kadirov, E. (1996) Gas-Particle Interaction in Detonation Spraying Systems. *J. Therm. Spray Technol.,* 5 (2), 185-195.

Kamnis, S. Gu, S. (2005) Numerical modelling of droplet impingement. *J. Phys. D*: Appl. Phys., 38 (19), 3664.

Kamnis, S. Gu, S. (2006) 3-D modelling of kerosene-fuelled HVOF thermal spray gun. *Chem. Eng. Sci.*, 61 (16), 5427-5439.

Kamnis, S. Gu, S. Zeoli, N. (2008a) Mathematical modelling of Inconel 718 particles in HVOF thermal spraying. *Surf. Coat. Technol.*, 202 (12), 2715-2724.

Kamnis, S. Gu, S. Lu, T. J. Chen, C. (2008b) Numerical modelling of sequential droplet impingements. *J. Phys. D*, 41 (16), 1-7.

Kamnis, S. Gu, S. Lu, T. J. Chen, C. (2009) Numerical modeling the bonding mechanism of HVOF sprayed particles. *Comput. Mater. Sci*. 46 (4), 1038-1043.

Kamnis, S. & Gu, S. (2010) Study of In-Flight and Impact Dynamics of Nonspherical Particles from HVOF Guns. *J. Therm. Spray Techn.* 19 (1-2), 31-41.

Karimi, M. Fartaj, A. Rankin, G. Vanderzwet, D. Birtch W. and Villafuerte, J. (2006) Numerical simulation of the cold gas dynamic spray process. *J. Therm. Spray Technol.,* 15 (4), 518-523.

Katanoda, H. Kuroda, S. Kawakita, J. Fukanuma, H. Matsuom, K. A study of gas and particle flow characteristics in HVOF thermal spray process. IN: *Proceedings of the 2004 international thermal spray conference*, May 10-12, Osaka, Japan.

Katanoda, H. Fukuhara, M. and Lino, N. (2007) Numerical study of combination parameters for particle impact velocity and temperature in cold spray. *J. Therm. Spray Technol.*, 16 (5-6), 627-633.

Katanoda, H. Kagoshima, J. Kawakita, J. Kuroda, S. Tsukuba, J. Numerical modeling of warm spray (two-stage HVOF) process. IN: *Proceedings of the 2008 international thermal spray conference,* June 2-4, Maastricht, The Netherlands.

Kawakita, J. Kuroda, S. Fukushima, T. Katanoda, H. Kazuyasu, M. Fukanuma, H. (2006) Dense titanium coatings by modified HVOF spraying. *Surf. Coat. Technol.*, 201 (3-4), 1250-1255.

Kawakita, J. Katanoda, H. Watanabe, M. Yokoyama, K. Kuroda, S. (2008) Warm Spraying: An improved spray process to deposit novel coatings. *Surf. Coat. Technol.*, 202 (18), 4369-4373.

Kestin, J. Sengers, J. V. Kamgar-Parsi, B. Levelt-Sengers, J. M. H. (1984) Thermophysical properties of fluid H_2O. *J. Phys. Chem. Ref. Data,* 13 (1) 175-183.

Killinger, A. Kuhn, M. Gadow, R. (2006) High-Velocity Suspension Flame Spraying (HVSFS), A New Approach for Spraying Nanoparticles with Hypersonic Speed. *Surf. Coat. Technol.*, 201 (5), 1922-1929.

Killinger, A. Gadow, R. Mauer, G. Guignard, A. Vaßen, R. Stöver, D. (2011) Review of New Developments in Suspension and Solution Precursor Thermal Spray Processes. *J. Therm. Spray Technol.,* 20 (4), 677-695.

Kim, K. Watanabe, M. Kawakita, J. Kuroda, S. (2009a) Effects of temperature of in-flight Particles on bonding and microstructure in warm-sprayed titanium deposits. *J. Therm. Spray Technol.*, 18 (3), 392-400.

Kim, K. Watanabe, M. Kawakita, J. Kuroda, S. (2009b) Grain refinement in a Single titanium powder particle impacted at high velocity. *Scripta. Mater.*, 59 (7), 768-771.

King, P. C. Zahiri, S. H. Jahedi, M. (2008) Focused ion beam micro-dissection of cold-spray particles, Acta Mater., 56 (19), 5617-5626.

Klinkov, S. V. Kosarev, V. F. Rein, M. (2005) Cold spray deposition: Significance of particle impact phenomena. *Aerosp. Sci. Technol.,* 9 (7), 582-591.

Kumar, A. Bae, G. Kang, K. Yoon, S. and Lee, C. (2009) Effect of powder state on the deposition behaviour and coating development in kinetic spray process. *J. Phys. D: Appl. Phys.,* 42 (7), 1-8.

Kuroda, S. Watanabe, M. Kim, K. Katanoda, H. (2011) Current Status and Future Prospects of Warm Spray Technology. *J. Therm. Spray Technol.*, 20 (4), 653-676.

Kuroda, S. Kawakita, J. Watanabe, M. Katanoda, H. (2008) Warm spraying - a novel coating process based on high-velocity impact of solid particles. *Sci. Technol. Adv. Mater.,* 9 (3), 1-17.

Latka, L. Pawlowski, L. Chicot, D. Pierlot, C. Petit, F. (2010) Mechanical properties of suspension plasma sprayed hydroxyapatite coatings submitted to simulated body fluid. *Surf. Coat. Technol.,* 205 (4), 954-960.

Lane, W. R. Prewett, W. C. Edwards, J. (1949) *Some experiments on the shatter of drops by transient blasts of air,* Technical Paper, Porton England, No. 115.

Lane, W. R. (1951) Shatter of drops in stream of air. *Ind. Eng. Chem.*, 43 (6), 1312-37.

Lane, W. R. Dorman, R. G. (1952*) Further experiments on the shattering of drops by a supersonic air blast,* Technical paper, Porton England, No. 279,

Launder, B. E. Spalding, D. B. (1972) Lectures in Mathematical Models of Turbulence. London, England: Academic Press.

Launder, B. E. Spalding, D. B. (1974) The numerical computation of turbulent flows. *Comput. meth. Appl. Mech.* Eng., 3 (2), 269–289.

Launder, B. E. Reece, G. J. Rodi, W. (1975) Progress in the development of a Reynolds-stress turbulence closure. *J. Fluid Mech.,* 68 (3), 537–566.

Launder, B. E. (1989) Second-moment closure: present... and future? *Int. J. Heat Fluid Flow* ,10 (4), 282–300.

Leonard, B. P. Mokhtari, S. (1990) ULTRA-SHARP Nonoscillatory Convection Schemes for High-Speed Steady Multidimensional Flow. NASA TM 1-2568 (ICOMP-90-12), NASA Lewis Research Center.

Li, C. -J. Li, W. -Y. (2003) Deposition characteristics of titanium coating in cold spraying. *Surf. Coat. Technol.,* 167 (2–3), 278–283.

Li, C. -J. Yang, G-J. Wang, Z. (2003) Formation of nanostructured TiO_2 by flame spraying with liquid feedstock. *Mater. Lett.*, 57 (13-14), 2130-2134.

Li, M. Shi, D. Christofides, P. D. (2004) Diamond Jet Hybrid HVOF Thermal Spray: Rule-Based Modeling of Coating Microstructure. *Ind. Eng. Chem. Res.,* 43 (14), 3632-3652

Li, M. Christofides, P. D. (2005) Multi-scale modeling and analysis of an industrial HVOF thermal spray process. *Chem. Eng. Sci.*, 60 (13), 3649-3669.

Li, M. Christophides, P. D. (2009) Modelling and control of High-Velocity Oxygen-Fuel (HVOF) Thermal Spray: A tutorial review. *J. Therm. Spray Technol.,* 18 (8-9), 753-768

Li, W. Y. and Li, C.J. (2005) Optimal design of a novel coldspray gun nozzle at limited space. *J. Therm. Spray Technol*., 14 (3), 391-396.

Li, W. Y. Liao, H. L. Wang, H. T. Li, C. J. Zhang, G. and Coddet, C. (2006) Optimal design of a convergent-barrel cold spray nozzle by numerical method. *Appl. Surf. Sci.,* 253 (2), 708-713..

Li, W. Y. Liao, H. L. Douchy G. and Coddet, C. (2007) Optimal design of a cold spray nozzle by numerical analysis of particle velocity and experimental validation with 316L stainless steel powder, *Mater. Des.*, 28 (7), 2129-2137.

Li, W. Y. Zhang, C. Guo, X.P. Zhang, G. Liao, H.L. Li C.J. and Coddet, C. (2008) Effect of standoff distance on coating deposition characteristics in cold spraying. Mater. Des., 29 (2), 297-304.

Li, W. Y. Zhang, C. Li, C. J. Liao, H. J. (2009) Modeling Aspects of High Velocity Impact of Particles in Cold Spraying by Explicit Finite Element Analysis. *Therm. Spray Techn.* 18 (5-6), 921-933.

Li, W. Y. Gao, W. (2009) Some aspects on 3D numerical modelling of high velocity impact of particles in cold spraying by explicit finite element analysis. *Appl. Surf. Sci*. 255 (18), 7878-7892.

Lima R. S. and Marple B. R. (2007) Thermal Spray Coatings Engineered from Nanostructured Ceramic Agglomerated Powders for Structural, Thermal Barrier and Biomedical Applications: A Review. *Therm. Spray Techn.* 16 (1), 40-63.

Lu, Y. -P. Li, M. -S. Li, S. -T. Wang, Z. -G. Zhu, R. -F. (2004) Plasma-sprayed hydroxyapatite+titania composite bond coat for hydroxyapatite coatingon titanium substrate. *Biomaterials*, 25 (18) 4393–4403.

Lupoi, R. O'Neill, W. (2011) Powder stream characteristics in cold spray nozzles. Surf. Coat. Technol., 206 (6), 1069–1076.

Magnussen, B.F. Hjertager, B.H. On mathematical modeling of turbulent combustion with special emphasis on soot formation and combustion. IN: *Proceedings of the 1976*

international symposium on combustion, August 15-20, Cambridge, Massachusetts, USA.

Mäkelä, J. M. Keskinen, H. Forsblom, T. Keskinen, J. (2004) Generation of metal and metal oxide nanoparticles by liquid flame spray process. *J. Mater. Sci.*, 39 (8), 2783-2788.

Maric, R. Roller, J. Neagu. R. (2011) Flame-Based Technologies and Reactive Spray Deposition Technology for Low-Temperature Solid Oxide Fuel Cells: Technical and Economic Aspects. *Therm. Spray Techn.* 20 (4), 696-718.

Marrocco, T. McCarney, D. G Shipway, P. H. Sturgeon, A. J. (2006) Production of titanium deposits by cold-gas dynamic spray: numerical modeling and experimental characterization. *J. Therm. Spray Technol.*, 15 (2), 263 - 272.

Mehdizadeh, N. Z. Raessi, M. Chandra, S. Mostaghimi, J. (2004) Effect of substrate temperature on splashing of molten tin droplets. *Journal of Heat Transfer,* 126, 445-452.

Meillot, E. Vert, R. Caruyer, C. Damiani, D. Vardelle, M. (2011) Manufacturing of nanostructured YSZ coatings by suspension plasma spraying (SPS): effect of injection parameters. *J. Phys. D: Appl. Phys.*, 44 (19), 1-8.

Morsi, S. A. and Alexander A. J. (1972) An investigation of particle trajectories in two-phase flow systems. *J. Fluid Mech.*, 55 (2), 193-208.

Mostaghimi, J. Pasandideh-Fard, M. Chandra, S. (2002) Dynamics of splat formation in plasma spray coating process. *Plasma Chem. Plasma Process,* 22 (1), 59-84.

Nguyen, C. T. Desgranges, F. Galanis, N. Roya, G. Maréd, T. Boucher, S. Angue Mintsa H. A. (2008) Viscosity data for Al_2O_3–water nanofluid—hysteresis: is heat transfer enhancement using nanofluids reliable? *Int. J. Therm. Sci.,* 47, 103–111.

Oberste-Berghaus, J. Legoux, J –G. Moreau, C. Hui, R. Decès-Petit, C. Qu, W. Yick, S. Wang, Z. Maric, R. Ghosh, D. (2008) Suspension and HVOF spraying of reduced temperature Solid Oxide Fuel Cell Electrolytes. *J. Therm. Spray Technol.,* 17 (5-6), 700-707.

O'Regan, B. Grätzel, M. (1991) A low-cost, high-efficiency solar cell based on dye-sensitized colloidal TiO_2 films. *Nature*, 353, 737-740

Papyrin, A. Kosarev, V. Klinkov, S. Alkhimov, A. Fomin, V. M. (2007) Cold Spray Technology. Amsterdam: Elsevier.

Pasandideh-Fard, M. Bhola, R. Chandra, S. Mostaghimi, J. (1998) Deposition of tin droplets on a steel plate: simulations and experiments. *Int. J. Heat Mass Transfer*, 41 (19), 2929-2945.

Pasandideh-Fard, M. Chandra, S. Mostaghimi, J. (2002a) A three-dimensional model of droplet impact and solidification. *Int. J. Heat. Mass. Transfer*, 45 (11), 2229-2242.

Pasandideh-Fard, M. Pershin, V. Chandra, S. Mostaghimi, J. (2002b) Splat shapes in a thermal spray coating process: simulations and experiments, *J. Therm. Spray Techn*. 11 (2), 206-217.

Patankar, S. V. (1980) *Numerical Heat Transfer and Fluid Flow*. Washington, DC: Hemisphere Publishing Corporation.

Pattison, J. Celotto, S. Khan, A. and O'Niell, W. (2008) Standoff distance and bow shock phenomena in the cold spray process. *Surf. Coat. Technol.,* 202 (8), 1443-1454.

Pawlowski, L. (2009) Suspension and solution thermal spray coatings. *Surf. Coat Technol.,* 203 (19), 2807–2829.

Pawlowski, L. (2008a) Finely grained nanometric and submicrometric coatings by thermal spraying: A review. *Surf. Coat. Technol.*, 202 (18), 4318–4328.

Pawlowski, L. (2008b) *The Science and Engineering of Thermal Spray Coatings 2nd ed.* Chichester, UK: John Wiley & Sons.

Peric, M. (1990) Analysis of pressure-velocity coupling on nonorthogonal grids. *Numer. Heat Transfer Part B*, 17 (1), 63-82.

Pohler, O. E. M. (2000) Unalloyed titanium for implants in bone surgery. Injury. 31(4), 7-13.

Prandtl, L. (1925) Uber die ausgebildet Turbulenz. Zeit. Ange. Math. Mech. 5, 136–139.

Price, T. S. Shipway, P. H. McCartney, D. G. (2006) Effect of Cold Spray deposition of a titanium coating on Fatigue behavior of a Titanium Alloy. *J. Therm. Spray Technol.,* 15 (4), 507-512.

Price, T. S. Shipway, P. H. McCartney, D. G. Calla, E. and Zhang, D. (2007) A Method for Characterizing the Degree of Inter-particle Bond Formation in Cold Sprayed Coatings. *J. Therm. Spray Technol.*, 16 (4), 566-570.

Price, T. S. (2008) Cold gas dynamic spraying of titanium coatings (Ph. D Thesis), University of Nottingham.

Raithby, G. D. and Schneider, G. E. (1979) Numerical solution of problems in incompressible fluid flow: treatment of the velocity-pressure coupling. *Numer. Heat Transfer Part A*, 2 (4), 417-440.

Rampon, R. Toma, F.-L. Bertrand, G. Coddet, C. (2006) Liquid Plasma Sprayed Coatings of Yttria-Stabilized Zirconia for SOFC Electrolytes. *J. Therm. Spray Technol.,* 15, 682–688.

Rampon, R. Filiatre, C. Bertrand, G. (2008) Suspension Plasma Spraying of YPSZ Coatings: Suspension Atomization and Injection. *J. Therm. Spray Technol.,* 17, 105–114.

Ranz, W. E. and Marshall, W. R. (1952a) Evaporation from drops, Part I*. Chem. Eng. Prog.* 48 (3) 141-146.

Ranz, W. E. and Marshall, W. R. (1952b) Evaporation from drops, Part II. *Chem. Eng. Prog.* 48 (4) 173-180.

Reitz, R. D. (1987) Mechanisms of Atomization Processes in High-Pressure Vaporizing Sprays. *Atomization and Spray Technology*, 3 (4), 309–337.

Roscoe, R. (1952) The viscosity of suspensions of rigid spheres. *Br. J. Appl. Phys.*, 3, 267-269.

Saito, T. Saba, M. Sun, M. Takayama, K. (2007) The effect of an unsteady drag force on a structure of a non-equilibrium region behind a shock wave in a gas-particle mixture. *Shock waves*, 17 (5), 255-262.

Schmidt, T. Gartner, F. Assadi, H. Kreye, H. (2006) Development of a generalized parameter window for cold spray deposition. *Acta. Mater.,* 54 (3), 729-742.

Shakeri, S. Chandra, S. (2002) Splashing of molten tin droplets on a rough steel surface. *Int. J. Heat Mass Transfer*, 45 (23), 4561-4571.

Shi, D. Li, M. Christphides, P. D. (2004) Diamond Jet Hybrid HVOF Thermal Spray: Rule-Based Modeling of Coating Microstructure. *Ind. Eng. Chem. Res*. 43 (14) 3653–3665.

Shih, T. H. Liou, W. W. Shabbir, A. and Zhu, J. (1995) New k-ε Eddy-Viscosity Model for High Reynolds Number Turbulent Flows - Model Development and Validation. *Comput. Fluids*, 24 (3), 227-238.

Shinoda, K. Murakami, H. (2010) Splat Morphology of Yttria-Stabilized Zirconia Droplet Deposited Via Hybrid Plasma Spraying. *J. Therm. Spray Techn*. 19 (3), 602-610.

Simmons, C.A. Valiquette, N. Pilliar, R. M. (1999) Osseointegration of sintered porous-surfaced and plasma spray-coated implants: An animal model study of early postimplantation healing response and mechanical stability. *J Biomed Mater Res*., 47 (2), 127-38.

Sivells, J. C. (1970) Aerodynamic design of axisymmetric hypersonic wind-tunnel nozzles. *Journal of Spacecraft and Rockets*, 7 (11), 1292–1299.

Sobolev, V. V. Guilemany, J. M. Nutting, J. Miquel, J. R. (1997) Development of substrate-coating adhesion in thermal spraying. *Int. Mater. Rev*., 42 (20), 117-136.

Stoltenhoff, T. Kreye, H. Richter. H. J. (2002) An Analysis of the Cold Spray Process and Its Coatings. *J. Therm. Spray Techn.* 11 (4) 542 – 550.

Sun, M. Saito, T. Takayama, K. Tanno, H. (2004) Unsteady drag on a sphere by shock wave loading, *Shock waves*, 14 (1-2), 3-9.

Sundararajan, G. Sen, D. Sivakumar, G. (2005) The tribological behaviour of detonation sprayed coatings: the importance of coating process parameters. *Wear*, 258(1-4), 377-391.

Stöver, D. Hathiramani, D. Vaßen, R. Damani, R. J. (2006) Plasma-sprayed components for SOFC applications. *Surf. Coat. Technol*., 201 (5), 2002-2005.

Swank, W. D. Fincke, J. R. Haggard, D. C. Irons, G. (1994) HVOF gas flow field characteristics. IN: *Proceedings of the 7th national thermal spray conference*, June 20-24, Boston, Massachusetts, USA.

Tabbara, H. Gu, S. (2009) Computational simulation of liquid-fuelled HVOF thermal spraying. *Surf. Coat. Technol.,* 204 (5), 676–684.

Tabbara, H. Gu, S. McCartney, D. G. Price, T. S. and Shipway, P. H. (2010) Study on Process Optimization of Cold Gas Spraying, *J. Therm. Spray Technol*., 20 (3), 608–620.

Tabbara, H. Gu, S. (2011) Numerical study of semi-molten droplet impingement. *Appl. Phys. A,* 104 (4), 1011-1019.

Tabbara, H. Gu, S. McCartney, D. G. (2011) Computational modelling of titanium particles in warm spray. *Comp. Fluids*, 44 (1), 358-368.

Tani, K. Nakahira, A. (2004) Latest study and subject of thermal spraying in Japan, IN: *Proceedings of the International Thermal Spray Conference*, May 10-12, Osaka, Japan.

Taylor, G. I. (1963) *The Shape and Acceleration of a Drop in a High Speed Air Stream, Technical report*. In the Scientific Papers of Taylor, G. I. ed. Batchelor, G. K.

Tikkanen, J. Gross, K. A. Berndt, C. C. Pitktnen, V. Keskinen, J. Raghu, S. Rajala, M. Karthikeyan, J. (1997) Characteristics of the liquid flame spray process. *Surf. Coat. Technol.,* 90 (3), 210-216.

Toma, F-L. Berger, L-M. Stahr, C. C. Naumann, T. Langner, S. (2010) Microstructures and functional properties of suspension-sprayed Al_2O_3 and TiO_2 coatings: an overview. *J. Therm. Spray Technol*. 19 (1-2), 262-274.

Touloukian, Y. S. Powell, R. W. Ho, C. Y. Klemens, P. G. (1970) *Thermophysical properties of matter. The TPRC data series. Volume 1: Thermal conductivity of metallic elements and alloys.* Plenum.

Touloukian, Y. S. (1970) *Thermophysical properties of matter. The TPRC data series. Volume 6: Specific Heat of nonmetallic Liquids and Gases.* Plenum.

Touloukian, Y. S. Buyco, E. H. (1971) *Thermophysical properties of matter. The TPRC data series. Volume 4: Specific heat: of metallic elements and alloys.* Plenum.

Trelles, J. P. Chazelas, C. Verdelle, A. Heberlein, J. V. R. (2009) *J. Therm. Spray Techn.,* 18 (5-6), 728-752.

Tucker, M. (1950) *Approximate Turbulent boundary-dayer development in plane compressible flow along thermally insulated surfaces with application to supersonic-tunnel contour correction*. NACA TN, Lewis Flight Propulsion Laboratory, 2045.

Ubbink, O. Issa, R. I. (1999) A method for capturing sharp fluid interfaces on arbitrary meshes. *J. Comput. Phys*., 153 (1), 26-50.

Van Doormaal, J. P. Raithby, G. D. and McDonald, B. H. (1987) The segregated approach to predicting viscous compressible fluid flows. *J. Turbomach.,* 109 (2), 268-277.

Vaßen, R. Yi, Z. Kaßner, H. Stöver, D. (2009) Suspension plasma spraying of TiO_2 for the manufacture of photovoltaic cells. *Surf. Coat. Technol*., 203(15), 2146-2149.

de Villiers Lovelock, H. L. (1998) Powder/processing/structure relationships in WC-Co thermal spray coatings: A review of the published literature. *J. Therm. Spray. Techn.,* 7(3), 357-373.

Voller, V. R. and Prakash, C. (1987) A Fixed-Grid Numerical Modeling Methodology for Convection-Diffusion Mushy Region Phase-Change Problems. *Int. J. Heat Mass Transfer*, 30, 1709–1720.

Voller, V. R. Swaminathan, C. R. Thomas, B. G. (1990) Fixed grid techniques for phase change problems: A review. *International Journal for Numerical Methods in Engineering, Special Issue: Numerical Methods in Thermal Problems*, 30(4), 875–898.

Williams, F. A. (1985) Combustion Theory 2nd ed. Addison-Wesley: London.

Wolfe, H. E. Anderson, W. H. (1964) *Kinetics, mechanism, and resultant droplet sizes of the aerodynamics breakup of liquid drops*. AGCD Report, Aerojet General Corp., Downey, Calfornia, SP No. 0395-04 (18).

Wu, T. Kuroda, S. Kawakitam, J. Katanoda, H. Reed, R. Processing and properties of titanium produced by warm spraying. IN: *Proceedings of the 2006 International Thermal Spray Conference*, May 15-18, Seattle, Washington, USA.

Wu, T. C. M. Bussmann, M. Mostaghimi, J. (2009) The Impact of a Partially Molten YSZ Particle. *J. Therm. Spray Techn.*, 18 (5-6), 957-964.

Xiaoou, H. and Yufen, L. (2004). The current situation and future of thermal spraying industry in China, IN: *Proceedings of the International Thermal Spray Conference*, May 10-12, Osaka, Japan.

Xiong, H. B. Zheng, L. L. Vaidya, A. (2005) Melting and oxidation behavior of in-flight particles in plasma spray process. *Int. J. Heat Mass Transfer*, 48 (25-26), 5121-5133.

Yang, G-J. Li, C-J. Wang, Y-Y. (2005) Phase formation of Nano-TiO_2 particles during flame spraying with liquid feedstock. *Therm. Spray Technol.,* 14 (14), 480-486

Yang , X. Eidelman, S. J. (1996) Numerical analysis of a high-velocity oxygen-fuel thermal spray system. *Therm. Spray Technol.,* 5 (2), 175-184.

Yoon, S. Xiong, Y. Kim, H. and Lee, C. (2009) Dependence of initial powder temperature on impact behaviour of bulk metallic glass in a kinetic spray process. *J. Phys. D: Appl. Phys*., 42 (8),1-5.

Zeoli, N. Gu, S. Kamnis, S. (2008) Numerical simulation of in-flight particle oxidation during thermal spraying. *Comput. Chem. Eng.,* 32 (7), 1661-1668.

Zhang, D. Harris, S. J. McCartney, D. G. (2003) Microstructure formation and corrosion behaviour in HVOF-sprayed Inconel 625 coatings. *Mater. Sci. Eng. A*, 344 (1-2) 45-56.

Zhang, D. McCartney, D. G. Shipway, P. H. (2005) Cold gas dynamic spraying of aluminum: the role of substrate characteristics in deposit formation. *J. Therm. Spray Technol.*, 14 (1), 109-116.

Zhao, L. Maurer, F. Fischer, M. Lugscheider, E. (2004) Study of HVOF spraying of WC-CoCr using on-line particle monitoring. *Surf. Coat. Tech.,* 185 (2-3), 160-165.

Zirari, M. Abdellah El-Hadj, A. Bacha, N. (2010) Numerical analysis of partially molten splat during thermal spray process using the finite element method. *Appl. Surf. Sci.* 256 (11), 3581-3585.